PHOTONICS Research

Review of gallium-oxide-based solar-blind ultraviolet photodetectors

Xuanhu Chen, Fangfang Ren, Shulin Gu, and Jiandong Ye*

School of Electronics Science and Engineering, Nanjing University, Nanjing 210093, China
**Corresponding author: yejd@nju.edu.cn*

Received 2 October 2018; revised 20 December 2018; accepted 23 January 2019; posted 24 January 2019 (Doc. ID 347203); published 7 March 2019

Solar-blind photodetectors are of great interest to a wide range of industrial, civil, environmental, and biological applications. As one of the emerging ultrawide-bandgap semiconductors, gallium oxide (Ga_2O_3) exhibits unique advantages over other wide-bandgap semiconductors, especially in developing high-performance solar-blind photodetectors. This paper comprehensively reviews the latest progresses of solar-blind photodetectors based on Ga_2O_3 materials in various forms of bulk single crystal, epitaxial films, nanostructures, and their ternary alloys. The basic working principles of photodetectors and the fundamental properties and synthesis of Ga_2O_3, as well as device processing developments, have been briefly summarized. A special focus is to address the physical mechanism for commonly observed huge photoconductive gains. Benefitting from the rapid development in material epitaxy and device processes, Ga_2O_3-based solar-blind detectors represent to date one of the most prospective solutions for UV detection technology towards versatile applications.

https://doi.org/10.1364/PRJ.7.000381

1. INTRODUCTION

Ultraviolet (UV) detection has attracted considerable attention, owing to its versatile applications in civilian infrastructures, military facilities, and scientific research. The UV spectral region is widely established to occupy the spectral interval of $\lambda = 400\text{–}10$ nm and is commonly divided into the following subdivisions: near ultraviolet (NUV), mid ultraviolet (MUV), far ultraviolet (FUV), and extreme ultraviolet (EUV) [1], as shown in Fig. 1. In addition to the above names, the following names for spectral regions may be encountered: ultraviolet A (UVA), ultraviolet B (UVB), ultraviolet C (UVC), and vacuum ultraviolet (VUV) [1], where the wavelength regions are also shown in Fig. 1.

As we all know, the most important natural UV source is the Sun, which emits UV radiation at all wavelengths. However, all UVC radiation from the Sun is absorbed by the diatomic oxygen (100–200 nm) or by the ozone (triatomic oxygen) (200–280 nm) in the atmosphere. In addition, VUV light is strongly absorbed by the air. Therefore, the UV region with wavelengths of 200–280 nm is "solar blind," meaning it can be detected without the influence of the Sun's radiation. Detectors with a cutoff below 280 nm could be defined as solar blind because they respond only to UV radiation with wavelengths shorter than the solar radiation that can penetrate the atmosphere of the Earth. They produce no measurable signal if they are exposed to normal outdoor lighting. Solar-blind deep-UV (DUV) photodetectors with excellent thermal stability and reliability have led to various applications in monitoring ozone holes, detecting flame, space communication, missile guidance, biochemical detection, and inspection of UV leakage. One advantage of wide-bandgap (WBG) semiconductors, which include GaN (3.40 eV, bandgap energy) [2], ZnO (3.29 eV) [3], ZnS (3.76 eV) [4], ZnSe (2.82 eV) [5], SiC (2.3–3.2 eV) [6,7], AlN (6.20 eV) [8], diamond (5.5 eV) [9,10], BN (4.5–5.5 eV) [11], and gallium oxide (Ga_2O_3) (4.4–5.3 eV) [12–14], and their combinations as, for example, $Al_xGa_{1-x}N$ [15], is that they can be made into solar-blind photodetectors. In addition, WBG materials are suitable for high-temperature and high-power applications [16,17] due to their high breakdown field strength in comparison to Si ($1.5\ \mathrm{W \cdot cm^{-1} \cdot {}^\circ C^{-1}}$ and 0.3 MV/cm [16], respectively), the most widely used semiconductor material for photodetectors (PDs).

Determined from the bandgap, binary compound semiconductors including GaN, SiC, and ZnO are mostly suitable for developing visible-blind UV detectors, which are required to have a higher responsivity in the UV range than in lower energy ranges. To meet the criteria of a solar-blind photodetector with a cutoff below 280 nm, alloying engineering to tune the bandgap up to 4.42 eV or the utilization of external Wood's UV filters to eliminate the longer wavelength is necessary. For instance, $Al_xGa_{1-x}N$ [18] and $Mg_xZn_{1-x}O$ [19] WBG ternary semiconductor alloys have been used to develop solar-blind photodetectors, and rapid progress has been achieved, including a high-performance avalanche solar-blind photodetector with

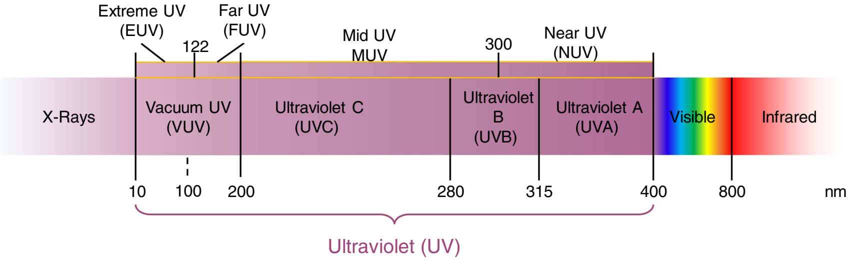

Fig. 1. UV spectral region and its subdivisions.

improved photoresponsivity and response speed [18]. The problems lie in the epitaxial growth of $Al_xGa_{1-x}N$ alloying films with a high Al component, which requires a critical growth temperature above 1350° [20,21]. $Mg_xZn_{1-x}O$ with a Mg composition over 37% will suffer phase segregation from wurtzite to rocksalt structure [22], which will introduce defects and dislocations around the separated domains and degrade the detecting performance. As one of the ultrawide-bandgap (UWBG) semiconductors, diamond material is one of the promising candidates for the development of solar-blind photodetectors [23]; however, bandgap engineering is difficult for such an elementary semiconductor [9,10], limiting its tunable photoresponse spectral range. The lack of large-area single-crystal diamond bulk material also hampers its practical application [17]. Alternatively, β–Ga_2O_3 is a promising candidate for solar-blind DUV detection. Monoclinic β-phase Ga_2O_3 has a bandgap of 4.4–4.8 eV [12] (with the corresponding wavelengths of 258–280 nm) and is expected to possess solar-blind sensitivity covering most of the range of the solar-blind UV region. Due to the availability of large-size Ga_2O_3 bulk single crystals [24], homoepitaxial growth of high crystalline quality epitaxial layers with defined doping and bandgap engineering can be used to fulfill the optoelectronic potential of Ga_2O_3 in UV detection [25].

In this review paper, we summarize recent advances in processing and device performance of solar photodetectors based on Ga_2O_3 material and related heterostructures. While briefly reviewing the basic types and key parameters of photodetectors, the fundamental optical properties, and processing development of the Ga_2O_3 material, the discussion mainly focuses on the device performance of Ga_2O_3 photodetectors in forms of bulk, epitaxy, and nanostructures, as well as the device physics according to the architecture of photodetectors. The roles of defects and radiation damages on the transport properties and device performance are discussed as well, together with the demonstration of novel hybrid heterostructures such as avalanche solar-blind photodetectors. These advances may provide better understanding on the Ga_2O_3 emerging material to fully exploit its promising optoelectronic application in the UV spectral region.

A. Basic Parameters of UV Photodetectors

1. Responsivity (R_i), Photoelectric Gain (g), and Internal Quantum Efficiency (η)

The current responsivity is one of the basic parameters to evaluate the sensitivity of a photodetector and is defined as the photocurrent per unit of incident optical power at a specific wavelength:

$$R_i = \frac{I_{\mathrm{ph}}}{P_\lambda} = \frac{I_{\mathrm{tot}} - I_{\mathrm{dark}}}{P_\lambda}, \tag{1}$$

where R_i is the current responsivity, I_{ph} is the photocurrent, P_λ is the incident optical power at the specific wavelength of λ, I_{tot} is the total current under illumination, and I_{dark} is the dark current.

Under illumination with a specific wavelength of λ, the responsivity is determined by the internal quantum efficiency η and the photoelectric gain g, where the internal quantum efficiency is defined as the yield of carriers per incident photon and the gain is the number of carriers passing contacts per one generated pair put forth by Rose [26]. As a result, the responsivity follows the relationship

$$R_i = \frac{\lambda\eta}{hc} qg, \tag{2}$$

where λ is the illumination wavelength, h is the Planck's constant, c is the light velocity, q is the electron charge, and ηg is the external quantum efficiency (EQE).

2. Response Time (τ) and Bandwidth (BW)

The response speed is normally described by the response time of the photodetector. It is characterized by the decay time τ_d and rise time τ_r, as defined as the time when the photocurrent drops from 90% to 10% and rises from 10% to 90% of the maximum value, respectively. Given the decay time and the rise time, which are simply assumed to be the same, the relationship to τ is that $\tau_d = \tau_r = \ln(0.9) \cdot \tau - \ln(0.1) \cdot \tau = \ln(9) \cdot \tau \approx 2.20\tau$. As a result, the bandwidth determined by the exponential transient response can be expressed as [27]

$$\mathrm{BW} = \frac{1}{2\pi\tau} = \frac{2.20}{2\pi\tau_d} = \frac{2.20}{2\pi\tau_r}. \tag{3}$$

3. Detectivity and Noise Equivalent Power

Detectivity (D^*) for a photodetector is a figure of merit used to characterize performance, equal to the reciprocal of noise-equivalent power (NEP), normalized per square root of the sensor's area and frequency bandwidth (reciprocal of twice the integration time), as defined to be

$$D^* = \frac{R_i (A_o \Delta f)^{1/2}}{I_n}, \tag{4}$$

where A_o is the effective radiation area of detectors, Δf is the bandwidth, and I_n is the current noise mainly caused by carrier generation and recombination processes. There are three main contributions to the noise that limits D^*, including dark-current-induced shot noise, Johnson–Nyquist noise, and thermal fluctuation "flicker" noise [28]. If, as expected, the shot noise from the dark current is the major contribution, the detectivity can be simplified as [28]

$$D^* = \frac{R_i}{(2qI_{\text{dark}})^{1/2}}. \tag{5}$$

The NEP is the optical input power for which the signal-to-noise ratio is equal to one. If the detector performance is determined by the background radiation when the thermal generation is reduced much lower than the background level, the NEP in this condition is given by [29]

$$\text{NEP} = \frac{(A_o \Delta f)^{1/2}}{D^*}. \tag{6}$$

The NEP yields the cutoff wavelength and rejection ratio of semiconductor photodetectors. The cutoff wavelength is closely related to the bandgap energy (E_g) of the semiconductor materials.

B. Types of Photodetectors and Device Processes

UV semiconductor photodetectors can be classified into three fundamental working modes: photoconductive detectors, Schottky barrier diode (SBD), and p–n junction photodiode. Figure 2 shows the schematic structure of different semiconductor photodetectors. Since there is no sign of p-type Ga_2O_3 achieved, the Ga_2O_3-based p–n homojunction has not been reported, and most Ga_2O_3-based photodetectors are working in photoconductive, SBD, or p–n heterojunctions. Herein, the basic work mechanisms of photoconductors and SBD are presented as follows.

1. Photoconductive Detectors

The photoconductive detector (photoconductor) is essentially a radiation-sensitive resistor, which follows the basic properties of a resistor. Assuming the photoconductor has an area of $A = wl$ and a thickness of t, and if, in most conditions, the sample resistance is much larger than the contact resistance, the basic expression describing photoconductivity under equilibrium excitation can be simplified as

$$I_{\text{ph}} = q\eta A \Phi_s g, \tag{7}$$

where I_{ph} is the short-circuit photocurrent under DC conditions and $\Phi_s(\lambda)$ is the photon flux density. Under V_b bias, the total current component caused by photon-generated electron–hole pairs is

$$I_{\text{ph}} = \frac{wtq(\Delta n \mu_e + \Delta p \mu_h)}{l} V_b, \tag{8}$$

where μ_e (μ_h) is the electron (hole) mobility, and Δn (Δp) is the excess electron (hole) concentration induced by illumination, respectively.

If the change in conductivity upon irradiation is relatively small with respect to the dark conductivity by assuming uniform and complete light absorption, the voltage responsivity of an n-type semiconductor photoconductive detector can be expressed as [30]

$$R_V = \frac{I_{\text{ph}} R_d}{\Phi_s A h\nu} = \frac{\eta}{lwt} \frac{\lambda \tau}{hc} \frac{V_b}{n_0}, \tag{9}$$

where τ is the excess carrier lifetime, n_0 is the thermal equilibrium carrier concentration, and the product of $\Phi_s A h\nu$ represents the absorbed monochromatic power. From the expression of R_V, high quantum efficiency η, long excess carrier lifetime τ, high bias voltage V_b, low thermal equilibrium carrier concentration n_0, and the smallest possible piece of crystal are desirable for achieving high photoconductive responsivity under a given wavelength λ. When the excitation light is frequency modulated, the responsivity as a function of frequency is expressed as [30,31]

$$R_f = R_V \frac{1}{(1 + 4\pi^2 f^2 \tau_{ef}^2)^{1/2}}, \tag{10}$$

where τ_{ef} is the effective carrier lifetime, and f is the excitation modulation frequency. As a result, the carrier lifetime or the response time can be fitted by the dependence of responsivity on modulation frequency [31].

2. Schottky Barrier Photodiodes

Photodiodes based on the Schottky junction, p–n junction, and type-II isotype heterojunctions, in which a built-in electric field occurs, are working in the photovoltaic mode. The built-in electric field helps separate photon-generated electron–hole pairs and excitons to move in opposite directions, which makes photodetectors exhibit self-powered properties under zero bias. In addition, the carrier transport also depends on the external circuit. In general, the Schottky barrier photodiode is a "majority carrier" device, which has unique advantages over the p–n junction dominated by minority carriers, such as simplified fabrication processes, short reverse recovery times, and high response speeds.

In terms of the ideal Schottky–Mott model [32], the rectifying property of the semiconductor and metal contact is determined by the difference in work functions of the metal (ϕ_m) and semiconductor (ϕ_s). As shown in Fig. 3, for an n-type semiconductor, if $\phi_m > \phi_s$, a Schottky contact forms with a barrier

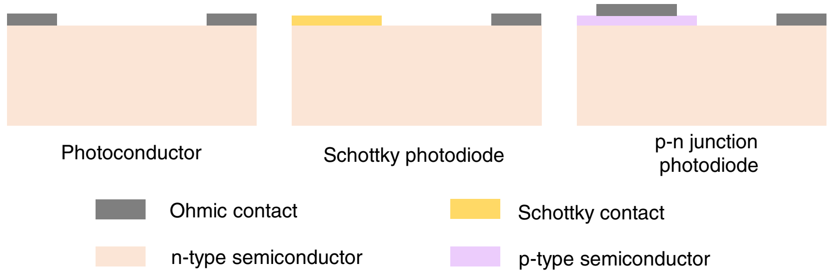

Fig. 2. Schematic structures of different semiconductor photodetectors.

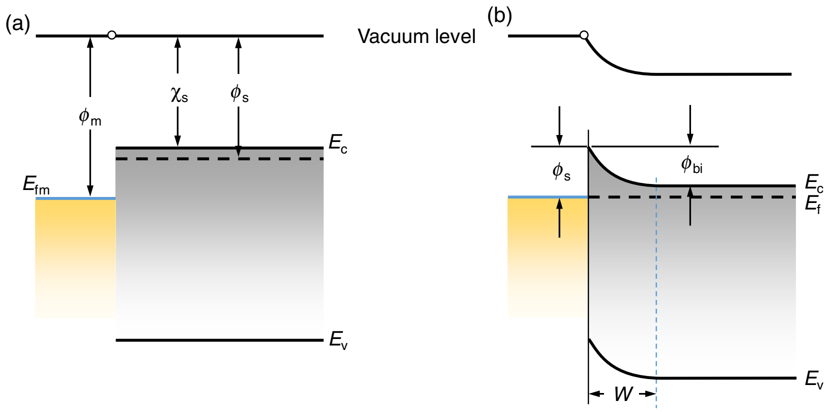

Fig. 3. (a) Energy band diagram of a metal and a semiconductor before contact; (b) ideal energy band diagram of a metal/n–semiconductor junction for $\phi_m > \phi_s$.

height given by $\phi_{bn} = \phi_m - \chi_s$, where χ_s is the electron affinity of the semiconductor. On the semiconductor side, ϕ_{bi} is the built-in potential barrier, expressed as $\phi_{bi} = \phi_m - \phi_s$, which is slightly dependent on the Fermi level of the semiconductor determined by the doping level. However, the built-in barrier of a real Schottky diode does not follow such an ideal and simple relationship with ϕ_m for a given semiconductor practically, as it is effectively reduced owing to the imaging force [33,34] and the presence of interface states [35]. Therefore, there are numerous and considerable variations among experimental data on ϕ_{bn} and ϕ_{bi}, which will be discussed in the following section by focusing on the fabrication processes of Ga_2O_3-based SBD photodetectors.

Various theories [36–39] have been developed to describe the carrier transport over the energy barrier of the Schottky diode. Among these theories, the thermal emission theory appears to explain the current–voltage (*I*–*V*) properties of high-mobility semiconductors [37], and the thermionic diffusion theory is applicable to low-mobility semiconductors [40]. In the presence of interfacial defects, the trap-assisted tunneling [41] and hopping [42] conduction mechanisms may also dominate the transport properties. In terms of thermionic theory, the current density of electrons for n-type semiconductors transported from the semiconductor over the potential barrier into the metal in the dark condition is expressed as [39]

$$J_T = J_{sT}\left[\exp\left(\frac{qV}{nkT}\right) - 1\right], \tag{11}$$

where V is the external applied voltage, n is the ideality factor, k is the Boltzmann's constant, T is the temperature, J_{sT} is the saturation current density as expressed as $J_{sT} = A^* T^2 \exp(-\frac{\phi_{bn}}{kT})$, $A^* = 4\pi q k^2 m^*/h^3 = 120 m^*/m_0\ \mathrm{A \cdot cm^{-2} \cdot K^{-2}}$ is the Richardson constant, and m^* is the effective electron mass. From Eq. (11), the saturation current density is very sensitive to temperature. The current density expressions of the thermionic diffusion and the thermionic emission theories are very similar except the expression of the saturation current density. The saturation current density in the diffusion theory is expressed as [30]

$$J_{sD} = \frac{q^2 D_e N_c}{kT}\left[\frac{q(V_{bi} - V)2N_d}{\varepsilon_s \varepsilon_0}\right], \tag{12}$$

where D_e is the diffusion coefficient, N_c is the density of states in the conduction band, and N_d is the donor density. As compared to the thermionic theory, the saturation current density in the framework of the thermionic diffusion mechanism is less sensitive to temperature variation.

For a nondegenerated n-type semiconductor, the contribution of light illumination to the current is primarily due to photogenerated carriers in the depletion region, with a width of $d = \left[\frac{2\varepsilon_s \varepsilon_0 (V_{bi} - V)}{qN_d}\right]^{1/2}$ [32]. Thus, the photocurrent density J_λ under a single-photon flux density Φ_s, which flows in the negative direction, depends on the applied voltage given by $J_\lambda = q\Phi_s[1 - \exp(-\alpha d)]$ [43], and α is the absorption coefficient of the material. Consequently, the current responsivity can be obtained through the relationship of $R_i = J_\lambda \lambda / \Phi_s hc$. However, the existence of trapping states (N_{ss}) at the Schottky contact interface, which originate from the surface states, metal-induced gap states, and/or the interface chemical reactions of metal and semiconductor atoms, will trap the photogenerated holes in the topmost surface region of the semiconductor side and generates net positive charges of $Q_{ss} = qN_{ss}$ [43]. Under illumination, photogenerated holes drift towards the surface region and are trapped by these traps, which produces net positive charge Q_{ss}. The metal negative charges Q_m and the positive charges Q_d in the depletion region satisfy the neutrality condition of $Q_{ss} + Q_d + Q_m = 0$. As a result, under an illumination circumstance, the amount of the band-bending $V_{bi\text{-}\lambda}$ will be reduced in terms of the relationship of $V_{bi\text{-}\lambda} = V_{bi\text{-}d} - Q_{ss} d / 2\varepsilon_s \varepsilon_0$ [43,44], where $V_{bi\text{-}d}$ is the barrier height in the dark condition, and d is the width of the depletion region. The decrease in V_{bi} under illumination will reduce the Schottky barrier ϕ_b, denoted as $\Delta\phi_b$. The reduction of V_{bi} is determined by the trapping states and the external applied voltage, leading to the reduction of the Schottky barrier. Accounting for the current contribution by the reduction of the Schottky barrier and by photogenerated excess carriers, the entire current under illumination is

$$J_{\text{tot}} = \exp\left(\frac{\Delta\phi_b}{nkT}\right)J_T - J_\lambda, \quad \textbf{(13)}$$

where the photocurrent component J_λ is contributed by the photon-generated electron–hole pairs in the depletion layer and has the opposite current direction against the dark current component and no contribution to the photoconductive gain. As a result, the responsivity can be expressed as [43,44]

$$R_i = \frac{\left[\exp\left(\frac{\Delta\phi_b}{nkT} - 1\right)\right]J_T - J_\lambda}{P_\lambda}. \quad \textbf{(14)}$$

Hence, the responsivity will differ under different light intensity below the saturation light intensity and the applied voltage. In the presence of traps, there are two mechanisms responsible for the observed photoresponse, including the component maintained by photogenerated excess carriers in the depletion region and the lowering effect of the Schottky barrier caused by trapping of photogenerated holes near the surface [43]. In fact, photogenerated holes localized at the trapping states at the metal–semiconductor interface will lead to high photoconductive gain but low response speed, which is commonly observed in the most Ga_2O_3-based solar-blind photodetectors, as discussed later on. The yield of huge high gain is caused by longer trapping and detrapping times as compared with the transit time of the electrons between the contacts and the resistive-capacitive (RC) delay time of the circuit.

3. Ohmic Contacts

Ohmic and Schottky contacts are essential for high-performance, high-reliability, and high-efficiency Ga_2O_3-based UV photodetectors. Ohmic contacts can be applied in both photoconductors and Schottky barrier photodetectors while Schottky contacts are the basis of self-powered Schottky barrier photodetectors.

To avoid reducing device switching speeds and encountering the reliability issues due to local contact heating during device operation, additional contact resistance should be excluded. According to the ideal Schottky–Mott model, for an n-type semiconductor, to achieve an Ohmic contact means that the work function of the metal should be equal to or smaller than that of the host semiconductor material. Since the work function of a practical-interest n-type semiconductor is mainly determined by the affinity of the semiconductor material, to achieve Ohmic contacts to β-Ga_2O_3, the work function of the metal should be close to or smaller than the affinity of β-Ga_2O_3, which is reported to be 4.00 ± 0.05 eV [33]. Therefore, Hf (3.9 eV, work function), Sc and La (both 3.5 eV), Zn (3.63 eV), and Gd (2.90 eV) are the potential choices for Ohmic contacts to β-Ga_2O_3 [45]. Most likely the contact will be bilayers of these with Au to reduce the contact sheet resistance and improve their reliability. A basic physical parameter used to describe the contact properties is the specific contact resistance ρ_c, which is independent of the contact geometry compared to the contact resistance and is typically expressed in the unit of $\Omega \cdot \text{cm}^2$. The transport properties in the contacts including the contact resistance R_c, the specific contact resistance ρ_c, the transfer length L_T, and the resistance of the semiconductor can be determined by the temperature-dependent transmission line method (TLM) or circular TLM (CTLM) measurements.

However, for UWBG semiconductors, Ohmic contact is a critical issue as commonly used metals have large work function and large barrier heights exist in the interface of semiconductors and metals [46]. The carrier transport properties and the specific contact resistance are mainly determined by the Schottky barrier ϕ_b and the doping concentration of the semiconductor. When the n-type Ga_2O_3 semiconductor is nondegenerated with a doping concentration of about 10^{16}–10^{18} cm^{-3}, the thermionic field emission is operative, and the specific constant resistance can be calculated from

$$\rho_c = \left(\frac{\mathrm{d}J_T}{\mathrm{d}V}\right)^{-1}_{|V=0} = \frac{kT}{qJ_{sT}} = \frac{k}{qA^*T}\exp\left(\frac{\phi_{bn}}{kT}\right). \quad \textbf{(15)}$$

To realize the reduction of the barrier height or the depletion width, heavier doping processes by *in situ* doping [47] or implantation [48–50] have been widely employed, which enhance the tunneling of electrons by reducing the barrier width. As Ga_2O_3 is degenerated, the specific contact resistance follows the relationship of [32]

$$\rho_c \sim \exp\left[\frac{4\sqrt{\varepsilon_s\varepsilon_0 m^*}}{\sqrt{N_{\mathrm{d}}}}\left(\frac{\phi_{bn}}{\hbar}\right)\right]. \quad \textbf{(16)}$$

Table 1 shows a summary of Ohmic contact processes to β-Ga_2O_3 from the reported literature. Specific contact resistance with optimal values in the range of 10^{-5}–10^{-6} $\Omega \cdot \text{cm}^2$ was achieved after processes of Si implantation, surface treatment, Ti-based metal stack, and rapid thermal annealing (RTA) [48,51–59]. In particular, n^+ degenerate doping in the selective region of β-Ga_2O_3 by Si implantation and postannealing activation in a temperature range of about 950°C are employed to realize electron tunneling and a rather low specific on-resistance [48,51]. Besides, In- and Ti-based electrodes are often utilized to form Ohmic contacts. However, In is properly not optimal due to the low melting point of only 157°C, while Ti contacts will be degraded above 600°C due to oxidation reactions with β-Ga_2O_3 [60]. Therefore, the RTA process for the electrode based on Ti has an optimized temperature of about 470°C [51,52,54–57]. Metal stacks with an adherent layer of Ti, an overlayer of Al, a barrier layer of Ni, and a cap layer of Au are used to reduce the sheet resistance of the contact. Metal bilayers of Ti/Au, and post-treatment of thermal annealing have also been attempted in the formation of Ohmic contacts to Ga_2O_3. Surface pretreatment with plasma exposure, reactive ion etching, and ion implantation is another alternative approach to reduce the barrier height by introducing a large amount of surface defects or increasing the effective shallow donor concentration on the surface by preferential loss of oxygen [52,53,55–58]. Intermediate semiconductors such as ITO [61,62] or ZnO [59] with a lower bandgap have also been employed to reduce the conduction band offset and improve carrier transport at the interface. It was reported that ITO/Pt contacts on n-Ga_2O_3 showed much better Ohmic contact than Ti/Pt contacts, which was attributed to the formation of a lower bandgap intermediate semiconductor layer and a higher doping concentration than the unintentionally doped (UID) Ga_2O_3 [62].

Table 1. Summary of Ohmic Contact Properties on β-Ga_2O_3

Metal Stack	Doping (cm^{-3})	Treatments	ρ_c ($\Omega \cdot cm^2$)/Method	Reference
Ti/Au (50/300 nm)	3×10^{19}	Si implantation in contact region 950°C annealing for implant activation 450 °C RTA for contact	4.6×10^{-6}/CTLM	Sasaki *et al.* [48]
Ti/Au	5×10^{19}	Si implantation in contact region 925°C annealing for implant activation 470°C RTA for contact	4.6×10^{-6}/CTLM	Higashiwaki *et al.* [51]
Ti/Au (20/230 nm)	3×10^{19}	Si implantation in contact region 950°C annealing for implant activation BCl_3 ICP etching prior 470°C RTA for contact	7.5×10^{-6}/TLM	Wong *et al.* [52]
Ti/Au	3×10^{18}	diffusion of Sn from the SOG layer BCl_3/Ar ICP etching prior 450°C RTA for contact	$(2.1 \pm 1.4) \times 10^{-5}$/TLM	Zeng *et al.* [53]
Ti/Au (30/130 nm)	10^{20}	degenerately doped contact layer with a high Si doping concentration above 10^{20} cm^{-3} 470°C RTA for contact	1.1 $\Omega \cdot$ mm/TLM	Zhang *et al.* [54]
Ti/Au/Ni	2.4×10^{14} cm^{-2}	BCl_3 ICP/RIE etching prior 470°C RTA for contact	4.6×10^{-6}/TLM	Krishnamoorthy *et al.* [55]
Ti/Al/Au (15/60/50 nm)	2.7×10^{18}	Ar plasma treatment	2.7 $\Omega \cdot$ mm/TLM	Zhou *et al.* [63]
Ti/Al/Ni/Au	$\sim 10^{19}$	BCl_3 ICP etching prior 470°C RTA for contact	4.7 $\Omega \cdot$ mm/TLM	Chabak *et al.* [56]
Ti/Al/Ni/Au (20/100/50/50 nm)	4.8×10^{17}	BCl_3 ICP/RIE etching prior 470°C RTA for contact	16 $\Omega \cdot$ mm/CTLM	Green *et al.* [57]
Ti/Al/Ni/Au	$\sim 10^{18}$	BCl_3 ICP etching prior	10.7–80.0 $\Omega \cdot$ mm/CTLM	Moser *et al.* [58]
AZO/Ti/Au (10/20/80 nm)	$\sim 10^{19}$ [48]	Si implantation in contact region 950°C annealing for implant activation 400°C RTA for contact	2.82×10^{-5}/TLM	Carey *et al.* [59]
ITO/Ti/Au (10/20/80 nm)	$\sim 10^{19}$ [48]	Si implantation in contact region 950°C annealing for implant activation 600°C RTA for contact	6.3×10^{-5}/TLM	Carey *et al.* [61]
ITO/Pt (140/100 nm)	2×10^{17}	800–1200°C RTA for contact	not measured but Ohmic for annealing above 900°C	Zhou *et al.* [62]
Ti, In, Ag, Sn, W, Mo, Sc, Zn, and Zr (20 nm), with Au (100 nm) overlayers	5×10^{18}	400–800°C RTA for contact	not measured In and Ti produced linear *I*–*V* curves after anneals	Yao *et al.* [60]

4. Schottky Contacts

For the β-Ga_2O_3-based Schottky diodes, the nonideal factors including the presence of interface-induced subgap states [33,64], the upward band-bending effect [34,64–66], and the Schottky barrier lowering due to the nonequilibrium carrier often affect the barrier height [43,67]. Table 2 demonstrates that the reported values of Schottky barrier height (SBH) ϕ_b and ideality factor n, are varied with the n-type doping concentration and processes of different metals for Schottky contacts to Ga_2O_3. As is well known, the barrier height can be extracted from the linear portions of the *I*–*V* curve and the voltage intercept V_{i0} in the forward bias region from the $1/C^2$–V curve, respectively. However, the *I*–*V* determined values, which are lower than those determined by the *C*–*V* method [64,68–70], should be more representative to the effective SBHs for current flow. As shown in Table 2, regardless of the metal used, the typical barrier heights are in the range of 1.00–1.50 eV when the ideality factor is close to 1. The large ideality factor ($n > 1$) is due to the generation recombination in the depletion region, tunneling, and/or terminal edge leakage [71], which may degrade the Schottky device performance and affect the detecting properties under illumination.

Figure 4 shows the summary of the SBH as a function of metals with different work functions. The short dashed curve represents the ideal SBH based on the ideal Schottky–Mott model, where the electron affinity of the Ga_2O_3 is chosen to be 4.00 eV [33]. It is found that the values of SBH determined by the *I*–*V* or *C*–*V* are scattered and show a weak correlation with the work functions of the metals. Comparing the reported SBH with the ideal Schottky–Mott model, the factors other than the metal work function should be taken into account to evaluate the Schottky barrier in Ga_2O_3. For instance, the method of metal deposition also plays an important role in determining the effective barrier. The barrier height of the same metal also varies on Ga_2O_3 with different orientation, which could result from the different surface reconstruction and different surface state density [64,72]. Besides metals, highly conductive metal-like nitrides and oxides can also be employed to form the Schottky contact [34,73]. Tadjer *et al.* [73] and Müller *et al.* [34] have proven that TiN deposited by ALD

Table 2. Summary of Reported Schottky Barrier Contacts to β-Ga_2O_3

Metal	Barrier Height (eV)	Ideality Factor	Doping (cm^{-3})	Process/Measurement	Comments	Reference
Ni	1.25	1.01	$\sim 1.13 \times 10^{17}$	evaporation Ni/Au, I–V and C–V	built-in voltage is 1.18 V from C–V and 1.0 V from I–V	Oishi *et al.* [68]
Ni	1.05	not measured	1.7×10^{17}	DC–sputtering, I–V and C–V	higher barrier measured with C–V	Armstrong *et al.* [69]
Ni	1.08–1.12	1.05–1.10	$(1.0–2.5) \times 10^{17}$	evaporation Ni/Au, I–V	sample etched with H_3PO_4 at 140°C	Kasu *et al.* [74]
Ni	0.95	3.38	UID	e-beam deposition Ni/Au, I–V	barrier height increase, and ideality factor decrease with temperature	Oh *et al.* [75]
Ni	0.8–1.0	1.8–3.2	UID	evaporation, I–V	$(Al_xGa_{1-x})_2O_3$ with x up to 0.164	Ahmadi *et al.* [71]
Ni	1.07	1.3	$\sim 9 \times 10^{16}$	e-beam deposition Ni/Au, I–V	barrier height increase, and ideality factor decrease with temperature	Ahn *et al.* [76]
Ni	1.54	1.04	$\sim 1.1 \times 10^{17}$	e-beam deposition, I–V	similar value to that from C–V	Farzana *et al.* [77]
Ni	1.10	1.05	$\sim 2.8 \times 10^{17}$	evaporation Ni/Au, I–V and C–V	sample etched with H_3PO_4 at 140°C	Kasu *et al.* [78]
Ni	1.2	1.00	$\sim 3 \times 10^{17}$	e-beam deposition Ni/Au, I–V	dry etch damage to Schottky contact	Yang *et al.* [79]
Ni	0.99–1.02	1.05–1.09	$\sim 3 \times 10^{17}$	evaporation Ni/Au, I–V	(001) substrate	Oshima *et al.* [80]
Ni	1.04 ± 0.02	1.33 ± 0.03	$(5–8) \times 10^{18}$	e-beam evaporation, I–V	cleaned with HCl and H_2O_2, vertical SBD	Yao *et al.* [72]
	1.08 ± 0.1	1.68 ± 0.04	UID			
	1.00 ± 0.06	1.57 ± 0.2	$(5–8) \times 10^{18}$			
Ni	0.81	2.29	UID	I–V	$(Al_xGa_{1-x})_2O_3$ with x to about 0.08	Qian *et al.* [81]
Pt	1.35–1.52	1.04–1.06	$(0.3–1) \times 10^{17}$	evaporation Pt/Ti/Au, I–V and C–V	sample etched with 85 wt.% H_3PO_4 at 135°C, higher barrier measured with C–V	Sasaki *et al.* [70]
Pt	1.15	~1.0	$\sim 1.0 \times 10^{16}$	evaporation Pt/Ti/Au, I–V and C–V	A^* was calculated to be $55\ A \cdot cm^{-2} \cdot K^{-2}$	Higashiwaki *et al.* [82]
Pt	1.04	1.28	$\sim 9 \times 10^{16}$	e-beam deposition Pt/Au, I–V	barrier height increase, and ideality factor decrease with temperature	Ahn *et al.* [76]
Pt	1.58	1.03	$\sim 1.1 \times 10^{17}$	e-beam deposition, I–V	similar value to that from C–V	Farzana *et al.* [77]
Pt	1.39	1.1	2.3×10^{14}	sputtering Pt/Ti/Au, I–V	barrier height stable up to at least 150°C	He *et al.* [83]
Pt	1.46	1.03 ± 0.02	1.8×10^{16}	evaporation Pt/Ti/Au, I–V and C–V	barrier height may be increasing by the presence of F	Konishi *et al.* [84]
Pt	1.01	1.07	$\sim 3 \times 10^{17}$	e-beam evaporation Pt/Au, I–V	comparison to TiN	Tadjer *et al.* [73]
Pt	1.05 ± 0.03	1.40 ± 0.04	$(5–8) \times 10^{18}$	e-beam evaporation, I–V	bulk and epilayer SBD, cleaned with HCl and H_2O_2	Yao *et al.* [72]
	1.34 ± 0.1	1.87 ± 0.3	UID			
Pt	1.05–1.20	1.34–1.55	$\sim 4.2 \times 10^{18}$	e-beam evaporation Pt/Au, I–V	both (010) and $(\bar{2}01)$ single-crystal substrates were used; the (010) SBD had a larger V_{ON}	Fu *et al.* [64]
Au	1.07	1.02	$(0.6–8) \times 10^{17}$	e-beam deposition, I–V	affinity of Ga_2O_3 4.00 ± 0.05 eV, work function of Au 5.23 ± 0.05 eV	Mohamed *et al.* [33]
Au	1.71	1.09	$\sim 1.1 \times 10^{17}$	e-beam deposition, I–V	interface consistent with inhomogeneous barrier	Farzana *et al.* [77]
Au	~1.1	1.08	10^{17}–10^{18}	e-beam deposition, I–V	barrier height decrease, and ideality factor decrease to near unity after annealing at temperature above 200°C	Suzuki *et al.* [85]
Pd	1.27	1.05	$\sim 1.1 \times 10^{17}$	e-beam deposition, I–V	similar value to that from C–V	Farzana *et al.* [77]
Cu	1.32	1.03	1.6×10^{18}	DC sputtering, I–V	low-mobility Ga_2O_3 layer grown by PLD	Splith *et al.* [86]
Cu	0.98, 1.07	1.05, 1.1	6×10^{16}	Cu/Au/Ni, I–V	SBD, MOSSBD	Sasaki *et al.* [87]
Cu	1.13 ± 0.1	1.53 ± 0.2	$(5–8) \times 10^{18}$	e-beam evaporation, I–V	bulk vertical SBD, cleaned with HCl and H_2O_2	Yao *et al.* [72]
W	0.91 ± 0.09	1.40 ± 0.4	$(5–8) \times 10^{18}$	e-beam evaporation, I–V	bulk and epilayer SBD, cleaned with HCl and H_2O_2	Yao *et al.* [72]
	1.05 ± 0.03	2.68 ± 0.3	UID			
Ir	1.29 ± 0.1	1.45 ± 0.2	$(5–8) \times 10^{18}$ UID	e-beam evaporation, I–V	bulk and epilayer SBD, cleaned with HCl and H_2O_2	Yao *et al.* [72]
TiN	0.98	1.09	$\sim 3 \times 10^{17}$	ALD 350°C, I–V	similar to Pt used as comparison	Tadjer *et al.* [73]
PtO_x	1.94	1.09	10^{17}	magnetron sputtering PtO_x/Pt, I–V	bulk crystal	Müller *et al.* [34]
	1.42	1.28	$(0.5–1) \times 10^{18}$		PLD sample	

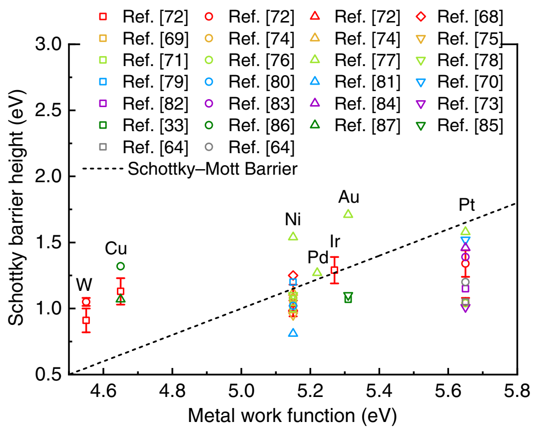

Fig. 4. Dependence of the Schottky barrier height on the metal work function of different metals, and the ideal Schottky barrier height based on the Schottky–Mott model (short dashed curve).

and PtO_x deposited by sputtering are good replacement materials to form the Schottky contact to Ga_2O_3.

2. FUNDAMENTAL PROPERTIES OF Ga_2O_3

As one of the representative UBG semiconductor materials, Ga_2O_3 has a WBG of about 4.4–5.3 eV [12–14], which corresponds to the wavelength at the UVC spectral region. The variation of the bandgap results from the different polymorphs of Ga_2O_3 with different structure symmetry [13,88–91] and its anisotropy along different orientations [12,89,92]. Ga_2O_3 has six different phases, among which the β-phase is the most thermodynamically stable phase [93], and most studies have been focused on β-Ga_2O_3 in the last decade. The most stable β-Ga_2O_3 has monoclinic structure, which belongs to space group $C2/m(C_{2h}^3)$ [94,95]. Any other polymorphs of Ga_2O_3 will be transformed to β-phase at sufficiently high temperature in air atmosphere [93,96], as shown in Fig. 5. Table 3 is a summary of the basic parameters of different phases of Ga_2O_3. The bandgap of the β-Ga_2O_3 is reported to be varied from 4.4 to 5.0 eV, determined by the optical transitions from the valence band maximum (VBM) to the conduction band minimum (CBM) according to the polarization golden rules [12].

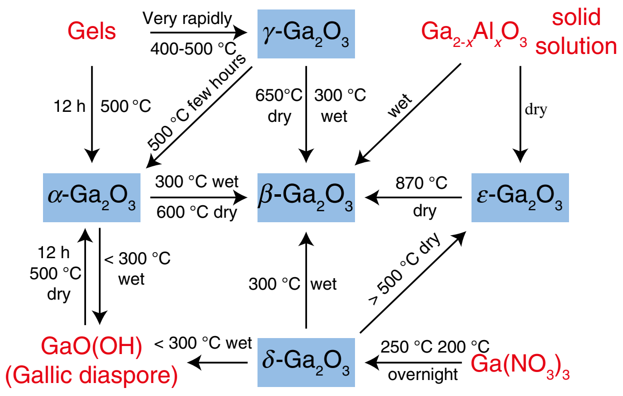

Fig. 5. Chart illustrating transformation relationships among the forms of Ga_2O_3 and its hydrates. Redraw with permission from Roy *et al.* [93]. Copyright 1952 American Chemical Society.

The other five polymorphs are commonly identified as α-, γ-, δ-, κ-, and ε-Ga_2O_3, which are less studied, but recently have drawn increasing attention due to their interesting properties. The metastable polymorph α-Ga_2O_3 has a rhombohedral structure, analogous to corundum (sapphire, α-Al_2O_3) with the space group of $R\bar{3}c$ [97,98]. The bandgap of α-Ga_2O_3 is reported to be about 5.3 eV [13,14,91], which means that it can be used in solar-blind detectors with a shorter cutoff wavelength and a higher breakdown electric field than the commonly used β-Ga_2O_3 material. α-Ga_2O_3 is thermodynamically a semistable phase and initially can only be synthesized at high pressures [14]. By strain engineering, Fujita *et al.* [14] reported the growth of high quality α-Ga_2O_3 thin films on sapphire substrates under atmospheric pressure at a temperature lower than 500°C [91]. The phase transition temperature of α-Ga_2O_3 can be lifted up to about 800°C when an α-$(Al_xGa_{1-x})_2O_3$ alloying buffer layer is introduced [99]. In addition, α-Ga_2O_3, along with other corundum-structured III-oxide semiconductors, α-In_2O_3 and α-Al_2O_3, enables the design and delivery of high-performance WBG heterostructure devices [14], such UV detectors with a wider sensitive range, Schottky diodes with a higher breakdown voltage, and high electron mobility transistors (HEMTs) based on modulation-doped $(Al_xGa_{1-x})_2O_3/Ga_2O_3$ [54,100].

The γ-Ga_2O_3 has a defective cubic spinel-type structure ($MgAl_2O_4$-type) with a space group of $Fd\bar{3}m$ [101–103], and its bandgap was reported to be 5.0 eV (direct bandgap) or 4.4 eV (indirect bandgap), whereas the specific band structure and the nature of optical transition in γ-Ga_2O_3 are still under a lack of study [102]. The other two polymorphs, δ-Ga_2O_3 and ε-Ga_2O_3, were first synthesized by Roy *et al.* [93] in 1952. The structure of δ-Ga_2O_3 was assumed to be structurally related to cubic defect spinels, such as γ-Al_2O_3, η-In_2O_3, and other M_2O_3 oxides [96]. Recent research indicates that pure ε-Ga_2O_3 thin films exhibit ferroelectric properties with strong spontaneous polarization [104,105]. The space group of ε-Ga_2O_3 was tentatively assigned as $P6_3mc$ [96,104,106], analogous to hexagonal GaN and ZnO materials, while the density functional theory (DFT) calculation and recent experimental results identify ε-Ga_2O_3 in the orthorhombic $Pna2_1$ symmetry [98,107,108], which is as an ordered subgroup of the hexagonal $P6_3mc$ [108,109]. The direct bandgap of ε-Ga_2O_3 is determined to be 4.9 eV from the $(\alpha h\nu)^2 - h\nu$ plot by Oshima *et al.* [106], while Nishinaka *et al.* [110] evaluated the optical bandgap of ε-Ga_2O_3 from the direct transition to be 5.0 eV and from the indirect transition to be 4.5 eV, respectively. Pure-phase high-quality ε-Ga_2O_3 thin films can be heteroepitaxially grown on the inexpensive substrates, including sapphire, Al_2O_3 [107,111], SiC [112], GaN [106], AlN [106], and MgO [110], which indicates ε-Ga_2O_3 provides more opportunities to design the optoelectronic devices by combining with other WBG semiconductors. Nevertheless, due to the most thermodynamically stable phase and the availability of β-Ga_2O_3 single crystalline substrate, most of the reported solar-blind photodetectors and power electronic devices are developed based on β-phase Ga_2O_3. Therefore, the following sections will mainly focus on the discussion of the band structure of β-Ga_2O_3 and the synthesis of

Table 3. Summary of the Basic Parameters of Ga_2O_3 Polymorphs

Polymorph	Bandgap	Structure and Space Group	Lattice Parameters	Comment	Reference
α	5.3 eV [91] (5.25 eV [113])	rhombohedral $R\bar{3}c$	$a = 4.9825 \pm 0.0005$ Å $c = 13.433 \pm 0.001$ Å	experimental	Marezio *et al.* [97]
			$a = 5.059$ Å $c = 13.618$ Å	calculated	Yoshioka *et al.* [98]
β	4.4–5.0 eV [12]	monoclinic $C2/m$	$a = 12.23 \pm 0.02$ Å $b = 3.04 \pm 0.01$ Å $c = 5.80 \pm 0.01$ Å $\beta = 103.7 \pm 0.3°$	experimental	Geller *et al.* [94]
			$a = 12.34$ Å $b = 3.08$ Å $c = 5.87$ Å $\beta = 103.9°$	calculated	He *et al.* [95]
γ	4.4 (indirect) [102] 5.0 (direct) [102]	cubic $Fd\bar{3}m$	$a = 8.30 \pm 0.05$ Å	experimental	Otero *et al.* [101]
			$a = 8.24$ Å		Oshima *et al.* [102]
δ	–	cubic $Ia\bar{3}$	$a = 10.00$ Å	experimental	Roy *et al.* [93]
			$a = 9.401$ Å	calculated	Yoshioka *et al.* [98]
ε	4.9 (direct) [106] 4.5 (indirect) [110] 5.0 (direct) [110]	hexagonal $P6_3mc$	$a = 2.9036$ Å $c = 9.2554$ Å	experimental	Playford *et al.* [96]
			$a = 2.906$ Å $c = 9.255$ Å	experimental	Mezzadri *et al.* [104]
	–	orthorhombic $Pna2_1$	$a = 5.120$ Å $b = 8.792$ Å $c = 9.410$ Å	calculated	Yoshioka *et al.* [98] Kracht *et al.* [107]
			$a = 5.0463$ Å $b = 8.7020$ Å $c = 9.2833$ Å	experimental	Cora *et al.* [108]

β-Ga_2O_3 materials in various forms of bulk, thin film, and nanostructures.

A. Bulk Crystal and Epitaxial Films of Ga_2O_3

Among the polymorphs of Ga_2O_3, β-Ga_2O_3 is the only one that is stable until the melting point under an atmospheric pressure of about 1800°C [114]. Various melt growth methods, including the Verneuil method [115,116], Vertical Bridgman [117,118], floating zone (FZ) process [119–130], Czochralski process (CZ) [114,131–133], and edge-defined film-fed growth (EFG) process [24,134–136], have been reported to synthesize the β-Ga_2O_3 bulk materials. Flux [137–139] and gas [140–142] phase methods have also been demonstrated for the growth of β-Ga_2O_3, but the crystal size is too small for practical applications. Most of the UID β-Ga_2O_3 bulk single crystal exhibits n-type conductivity, which is possibly a result of intrinsic shallow donor defects (Ga interstitial) [143] or external impurities (H, C or Si) [24,130]. Similar to the asymmetric doping in ZnO, n-type conductivity of β-Ga_2O_3 single crystals or epitaxial films can be easily achieved by the doping of tetravalent elements (Si, Sn, or Ge) with a resultant free-electron concentration in the range of 10^{16}–10^{20} cm^{-3} [24,25,128,143–150]. In contrast, no effective p-type conductivity of β-Ga_2O_3 has been reported, which is strongly hindered by a very low formation energy of self-trapped holes (STHs) [69,151,152] and almost no dispersion of the energy levels near the top of the valence band [153,154]. Doping with Fe, Mg, and N does not convert β-Ga_2O_3 into p-type but results in the semi-insulating status [154–157], which has been used as substrates for the fabrication of MOSFET devices with low leakage current [49,57,100,158].

To date, large-size β-Ga_2O_3 bulk crystals were mainly synthesized at a growth rate up to 10 mm/h by using the EFG technique [24], which has been widely used to produce large-size sapphire bulk material. The 2 inch (1 inch = 2.54 cm) UID and Fe-doped semi-insulating β-Ga_2O_3 wafers with orientations of $(\bar{2}01)$ and (100) are commercially available, and 6 inch technology is also under development [24]. The major residual donor impurities in the UID crystal are Si with its concentration of about 2×10^{17} cm^{-3}, which is consistent with the C–V measurements of an $(N_d - N_a)$ value of 2×10^{17} cm^{-3}. Therefore, UID bulk crystals have a typical electron background concentration in the $\sim 10^{17}$ cm^{-3} level and an electron mobility of ~ 130 $cm^2/(V \cdot s)$ at room temperature [68,131,143,159]. The *in situ* doping of Sn or Si can be achieved with the carrier concentration in the range of 1.0×10^{18} to 2.0×10^{19} cm^{-3} [24]. Since the $\langle 010 \rangle$ crystallographic direction is parallel to both the cleavage planes $\{100\}$ and $\{001\}$ [160], the (100)- and (001)-oriented substrates are fragile during the fabrication processes [24]. Interestingly, a large lattice constant along the [100] direction facilitates the mechanical cleavage of the β-Ga_2O_3 crystal into thin flakes or nanomembranes [161] along this plane, which provides an alternative platform to develop β-Ga_2O_3 membrane-based field-effect transistors (FETs) [63,161–166] and solar-blind photodetectors [167–170].

To meet the high demand for power electronic device applications, great efforts have been made on the epitaxial growth of Ga_2O_3 thin films in recent years by various technological means, including molecular beam epitaxy (MBE) [25,171,172], metal–organic vapor phase epitaxy (MOVPE) [145,173], halide vapor phase epitaxy (HVPE) [174,175], low-pressure chemical vapor deposition (LPCVD) [176,177], pulsed laser deposition (PLD) [90,148], and mist chemical vapor deposition (mist-CVD) [146]. Due to the availability of β-Ga_2O_3 bulk substrates, high-quality homoepitaxy of β-Ga_2O_3, and the related ternary alloying films with low densities of dislocation and defects, a well-controlled n-type doping by Si, a high electron mobility, and an atomic smooth surface morphology, have been achieved [25,145,147,178]. High-crystalline-quality $(Al_xGa_{1-x})_2O_3/Ga_2O_3$ heterostructures have been produced by plasma-assisted MBE with modulation doping of Si [100,178] and Ge [179] and high-mobility 2D electron gas has been observed at their interface, which delivers the demonstration of the first HEMT based on β-Ga_2O_3 [100]. However, the crystalline quality of the heteroepitaxial growth of β-Ga_2O_3 thin films (mainly on *c*-plane sapphire) is poor. The crystalline structure difference and lattice misfit between β-Ga_2O_3 and α-Al_2O_3 lead to 3D island growth, lattice twist, and phase segregation at the interface [180]. In addition, it is very difficult to realize the defined doping in these heteroepitaxially-grown films.

In contrast, the other metastable polymorphs, including α-, ε-, and γ-Ga_2O_3 thin films, have been heteroepitaxially grown on foreign substrates including sapphire, AlN [106], SiC [112], GaN [106], ZnO [181], and MgO [110]. The used epitaxial techniques are mostly based on chemical vapor deposition (CVD) techniques, such as mist-CVD, HVPE, and MOCVD. For instance, high-crystalline-quality α-Ga_2O_3 thin films with device-acceptable doping and the ternary epilayers have been grown on sapphire substrates using the mist-CVD technique developed by Fujita *et al.* [182–184]. The α-Ga_2O_3 films on sapphire exhibit a narrow diffraction peak for the (0006) plane with typical FWHMs of 30–60 arcsec [184]. Recently, the highest mobility of 31.5 $cm^2/(V \cdot s)$ was achieved for the Si-doped α-Ga_2O_3 film at the carrier density of 3×10^{18} cm^{-3} [185]. With advances of the mist-CVD technique in low-temperature synthesis, high growth rate, well-controlled doping and low-cost, high-voltage Schottky rectifiers [186] and metal-semiconductor-field-effect-transistors (MESFETs) [187] based on α-Ga_2O_3 have been demonstrated, which are even superior to the devices based on the β-Ga_2O_3 homoepilayers. In addition, a pure-phase ε-Ga_2O_3 can also be grown by MBE [107] and PLD [188] on sapphire, but the optimized growth window is quite narrow because of the formation of mixed β- and ε-phases as compared to the CVD methods. Having similar hexagonal symmetry with common WBG semiconductors, ε-Ga_2O_3 is normally achieved on sapphire, GaN, AlN, and SiC substrates, and unique properties such as ferroelectric polarization have been discovered [104,105]. However, the crystalline quality is still fair due to the domain rotation with respect to the substrates. If the material quality meets the criteria of device fabrication, it is expected that ε-Ga_2O_3 will provide an alternative platform for the development of low-consumption transistors, switchable memories, and UV photodetectors. A few studies have reported the epitaxial growth of γ-Ga_2O_3 thin films [102,189], but the fundamental properties of γ-Ga_2O_3 thin films are rare.

B. Nanostructures of β-Ga_2O_3

Low-dimensional crystalline β-Ga_2O_3 nanostructures in a variety of forms, such as nanocrystals [190–196], nanowires (NWs) [197–241], nanorods (NRs) [242–251], nanobelts (NBs) [248,249,252–256], nanosheets (NSHs) [248,249,252, 257–259], and other configured structures [220–222,224, 260–263], have been synthesized by various means, as summarized in Fig. 6. NBs or nanoflakes of β-Ga_2O_3 can also be produced from the (100) single crystal β-Ga_2O_3 substrate by a mechanical exfoliation method [163,167–170,264,265]. These low-dimensional β-Ga_2O_3 structures have been utilized in the investigation of the fundamental properties as well as

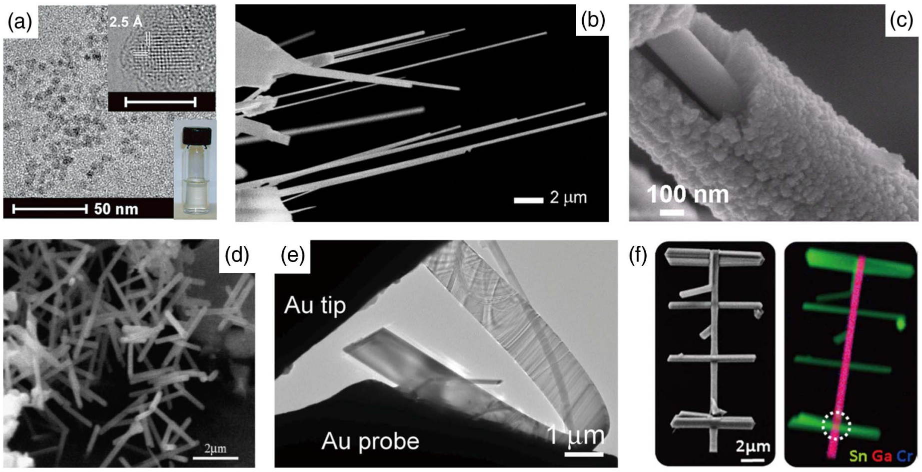

Fig. 6. Various Ga_2O_3 nanostructures. (a) γ-Ga_2O_3 nanocrystals. Reprinted with permission from Wang *et al.* [196]. Copyright 2010 American Chemical Society. (b) β-Ga_2O_3 nanowires. Reprinted with permission from Nogales *et al.* [229]. Copyright 2007 American Institute of Physics. (c) $Ga_2O_3/GaN{:}O_x@SnO_2$ shell@core NWs. Reprinted with permission from Lupan *et al.* [234]. Copyright 2015 Elsevier B.V. (d) β-Ga_2O_3 nanorods. Reprinted with permission from Vanithakumari *et al.* [244]. Copyright 2009 Wiley-VCH Verlag GmbH & Co. KGaA, Weinheim. (e) As-synthesized β-Ga_2O_3 nanobelt. Reprinted with permission from Zou *et al.* [256]. Copyright 2014 Wiley-VCH Verlag GmbH & Co. KGaA, Weinheim. (f) Branched multiwire nanostructures (left) and its X-ray fluorescence (XRF) map (right). Reprinted with permission from Martinez-Criado *et al.* [224]. Copyright 2014 American Chemical Society.

the implementation of functional devices including FETs [163,202], gas sensors [197,209,225], and solar-blind photodetectors [207,254,266].

Several approaches have been developed to synthesize Ga_2O_3 nanostructures, such as the vapor–liquid–solid (VLS) or vapor–solid (VS) process [206,213,220,267], the solution process [190,196,255,268], physical evaporation [203,224, 235,248], plasma exposure [257], thermal oxidation of compacted gallium nitride powder [249,269], and thermal reduction chemical vapor transport (CVT) [256], as well as recently developed mechanical exfoliation methods. The VLS and VS processes have been proven to be favorable to achieve high-quality β-Ga_2O_3 nanostructures, especially NWs [270]. In the VLS process, Au is the most commonly used metal catalyst to grow β-Ga_2O_3 nanostructures. Terasako *et al.* [233] reported that the average diameter of NWs and the morphology of β-Ga_2O_3 nanostructures, such as NWs, NBs, and NSHs, can be controlled by tuning the Au thickness, the growth time, and the growth temperature. Alternatively, Johnson *et al.* [212] reported the use of Fe as the catalyst to grow GaN NWs, Ga_2O_3 NWs, and Ga_2O_3 nanoribbons by using ion implantation of Fe^+ into the thermally grown SiO_2 layers and subsequent annealing to form the catalyst nanoparticles. However, the use of a metal catalyst has the risk of some level of impurity incorporation into the β-Ga_2O_3, which may introduce deep-level defects and affect the electrical properties of the material. Cho *et al.* [248] investigated that various forms of β-Ga_2O_3 nanostructures such as NWs, NRs, NBs, NSHs, and nanocolumns could be successfully synthesized by simple evaporation of metallic gallium with no assisted catalyst in a flow of argon gas. Zhao *et al.* [240,271] reported ZnO–Ga_2O_3 core–shell microwires synthesized using a one-step approach on Si substrate by the CVD method. Because of the different growth threshold temperature of ZnO (900°C) and Ga_2O_3 (1100°C), the synthesis of the ZnO–Ga_2O_3 core–shell structure could be designed in one temperature rise continuous reaction process [271]. The ZnO core and the Ga_2O_3 shell were both single crystalline with few noticeable structural defects at the interface, which enables the demonstration of Ga_2O_3-based APDs.

In addition, several dopants such as N [201,250], Zn [202], Li [220], Cr [221,222,228,229,245], Sn[222,226], Er [229,261], and In [237] have been reported to be doped in β-Ga_2O_3 nanostructures and predominantly modify the optical properties. The presence of Sn leads to a broad emission in the UV-blue and UV-green ranges as observed by cathodoluminescence (CL) characterizations [222]. Lithium is of potential interest as a dopant in Ga_2O_3 nanostructures to modify its conductivity for electrical energy storage applications. However, no evidence proves the difference in conductivity of the Ga_2O_3 nanostructures with Li doping [220]. Zinc was expected to be a shallow acceptor by a diffusive doping method to increase the mobile carriers in Ga_2O_3 NWs [202] with a demonstration of p-channel FETs. However, it is still debatable due to a low hole mobility of $\sim 10^{-2}\ \mathrm{cm}^2/(\mathrm{V}\cdot\mathrm{s})$. Despite distinguished advantages of nanostructure-based devices, the reproducibility of the nanostructures and realization of high-yield and high-reliability contacts remain challenging issues. Effective doping to control the electrical and optical properties of nanostructures is also complicated, which hampers their practical applications.

C. Band Structures of β-Ga_2O_3

β-Ga_2O_3 is the most representative in the polymorphs of Ga_2O_3, and its band structure has been investigated considerably in theoretical and experimental aspects. Figure 7 displays the schematic structure of a β-Ga_2O_3 unit cell. As mentioned above, β-Ga_2O_3 has a monoclinic structure, where the angle $\beta = 103.7°$. The unit cell of β-Ga_2O_3 contains two crystallographically different Ga atoms in the asymmetric unit, one with tetrahedral (Ga_I) and the other with octahedral (Ga_{II}) coordination geometry. Correspondingly, there are three types of oxygen ions (O_I, O_{II}, O_{III}) in the unit cell, which leads to an anisotropy in thermal conductivities [272], phonon vibrational modes [273], effective mass [89,274], optical bandgap [12,89,275], and surface formation energy [276,277]. For instance, the optical anisotropy of β-Ga_2O_3 is caused by the transitions of electrons from the valence bands to the CBM according to the Fermi golden selection rules [12].

The band structure of Ga_2O_3 calculated by DFT is shown in Fig. 8 [275]. The CBM is located at the Γ point (the Brillouin zone center) and is isotropic with the effective electron mass in the range of $0.24m_0$–$0.34m_0$ [95,278,279]. The VBM is located at the L point (½, ½, ½), while in most previous publications it is labeled as the M point [275]. The VBM is slightly higher than $\Gamma(0,0,0)$ (less than 100 meV) as reported by theoretical calculation and experimental results [12,92,95,274,275,279,280], which strongly suggests that β-Ga_2O_3 is an indirect bandgap semiconductor. The indirect bandgap is slightly smaller than the direct bandgap with the energy difference of 0.03–0.04 eV by Onuma *et al.* [12]. The calculated results are in good agreement with absorption [12] and angle-resolved photoemission spectroscopy (ARPES) measurements [280–282]. Recently, the indirect nature of optical transition is identified to be retained after alloying with Al, and the VBM eigenvalue differences between the M and Γ points become larger as the Al content increases in β-$(Al_xGa_{1-x})_2O_3$ [283]. The indirect bandgap nature of β-$(Al_xGa_{1-x})_2O_3$ is as expected when one considers the fact that the top valence band is predominantly formed by O-2p orbitals. As β-Ga_2O_3 has been proven to be an indirect semiconductor, the typical

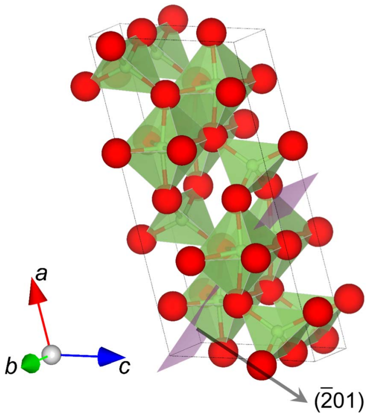

Fig. 7. The crystal structure of β-Ga_2O_3 and its $(\bar{2}01)$ surfaces.

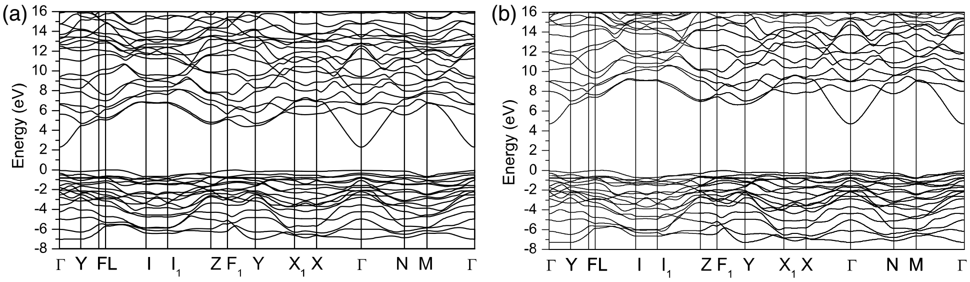

Fig. 8. Band structure of β-$\mathrm{Ga_2O_3}$. (a) At the GGA–DFT (PBE) level and (b) at the hybrid HF–DFT (Gau–PBE) level. Reprinted with permission from Mock *et al.* [275]. Copyright 2017 American Physical Society.

emission spectra recorded by means of photoluminescence (PL) and CL do not exhibit near-band-edge (NBE) emissions corresponding to the band-to-band optical transitions, while the UV luminescence (UVL) and blue luminescence (BL) bands related to the intrinsic defects are widely observed in β-$\mathrm{Ga_2O_3}$ with various forms of bulk, epilayers, or nanostructures [155,284,285]. The UVL band is widely recognized as being impurity independent [285,286], and experimental [285,286] and theoretical [151] studies have attributed it to the recombination of free electrons and STHs or self-trapped excitons. The BL band has been attributed to the donor–acceptor pair transitions involving deep donors and acceptors [286,287]. Therefore, although the detector based on β-$\mathrm{Ga_2O_3}$ is insensitive to the light it emits, the subgap absorption via these intrinsic defects will definitely reduce the UVC-to-UVA rejection ratio of the photoresponsivity and degrade the performance of the solar-blind detection. The existence of subgap defects is also an origin to produce a persistent photoconductivity (PPC) effect, which hinders the high-speed operation of the photodiodes for practical applications. Therefore, the suppression of defect-related subgap absorption is critical, and improving material growth technologies is the key solution to achieve low-defect density and high performance of the final devices.

In addition, the valence band ordering in β-$\mathrm{Ga_2O_3}$ contributes to the various transition from the valence bands to the CBM. The variation in band-to-band transition determines the absorption edges observed in experiments without taking the Urbach tail states into account. Polarized reflectance spectra and transmission spectra of different-orientation single-crystalline substrates can be used to determine the energies of different transitions from VBM to the CBM in terms of the selection rules. The polarized absorption edges are located at 4.48 eV, 4.57 eV, and 4.70 eV with incident light having the configuration of $E//c$, $E//a$ (or $E//a^*$, where the a^* axis is perpendicular to the (100) plane and is angled at −13.7° from the a axis), and $E//b$, respectively, at room temperature (RT). Therefore, the unpolarized transmittance spectra from the substrates must exhibit a distinct shoulder at 4.5–4.7 eV [12,89], and correspondingly, the shoulder will affect the responsivity of solar-blind photodetectors. The variation in reflectance and the absorption edges of different-orientation β-$\mathrm{Ga_2O_3}$ bulk crystals are shown in Fig. 9 [12]. Accordingly, the spectral wavelength of peak photoresponsivity of β-$\mathrm{Ga_2O_3}$-based photodetectors would be sensitive to the polarization of the incident light. From the viewpoint of reliability, the polarization-dependent photoresponsivity is indeed an undesirable trait for practical photodetectors. To minimize the effect of optical anisotropy on the responsivity of the devices, it would be better to choose (010) oriented β-$\mathrm{Ga_2O_3}$ crystals, which demonstrate a minimum difference on absorption edges of only ~0.1 eV. Furthermore, the optical anisotropic characteristics are almost negligible in epitaxial $(\bar{2}01)$ $\mathrm{Ga_2O_3}$ layers, which would also be a good solution to this problem. On the other hand, the polarization-sensitive anisotropic absorption may also open an opportunity to develop spectrally selective solar-blind photodetectors by light polarization engineering in β-$\mathrm{Ga_2O_3}$ single crystals. For example, similar to the bandpass photodetectors based on nonpolar GaN and

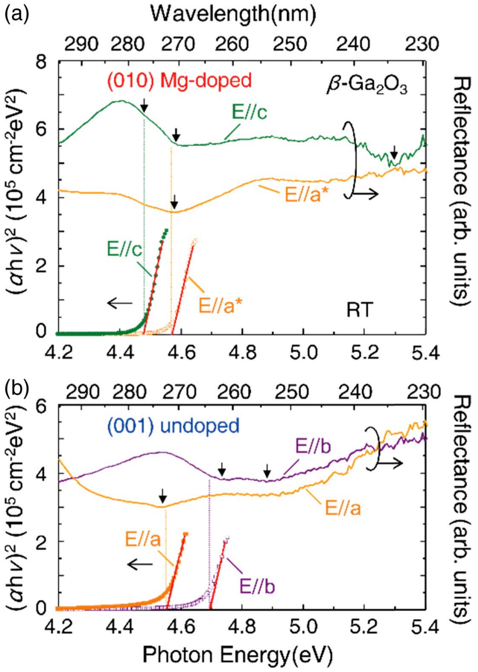

Fig. 9. $(\alpha h\nu)^2$ versus $h\nu$ plots for (a) (010) Mg-doped substrate for $E||c$ (closed circles) and $E||a^*$ (open circles) at RT. (b) Data set of (001) undoped substrate for $E||a$ (closed squares) and $E||b$ (open squares). Dotted lines represent the energies of the direct absorption edge. Partially polarized reflectance spectra at RT are shown in the upper part of the figures. Energies of the dips and the shoulder are indicated by the vertical arrows. Reprinted with permission from Onuma *et al.* [12]. Copyright 2015 The Japan Society of Applied Physics.

ZnO epilayers, by combining an identical β-Ga_2O_3 (100) single crystal with an orthogonal alignment to the planar detector, a highly narrow band photodetector demonstrates the strong capability to detect weak signals of DUV light with a specific wavelength and its polarization state. It provides a new paradigm for narrow bandpass photodetectors with broad applications where noises from a full daylight background or environmental radiation need to be suppressed [288–290].

D. Feasibility of p-Type Doping

It has been reported that the conductivity of β-Ga_2O_3 could be easily tuned over many orders of magnitude ranging from 10^{-12} to 10^3 S/cm [120,155]. To further extend the utility and applications of β-Ga_2O_3 in photodetectors as well as other bipolar optoelectronic devices, it is necessary to realize stable and reliable p-type β-Ga_2O_3. However, for WBG transparent oxide semiconductors, such as ZnO, Ga_2O_3, and In_2O_3, the creation of positive carriers (holes) is a most challenging issue, which is mainly limited by (i) the high formation energy of the native acceptors that produce holes, such as cation vacancies; and (ii) the low formation energy of native donors that compensate acceptors, such as anion vacancies [291]. The native point defects in β-Ga_2O_3 that act as donors, which are oxygen vacancies at threefold coordinated sites (O1 and O2) and fourfold coordinated sites (O3), do not directly contribute to the electrical conductivity because of the high formation energies of 3.31, 2.7, and 3.57 eV for O1, O2, and O3, respectively [292]. On the other hand, V_{Ga} acts as a deep-level acceptor with a large ionization energy. Therefore, intrinsic vacancies alone cannot contribute enough free carriers for the electrical conductivity of β-Ga_2O_3. Hydrogen as well as other external impurities such as Si, Ge, and Sn could be the contributors to the n-type conduction of unintentionally doped β-Ga_2O_3 with a background electron concentration of 10^{16} to 10^{17} cm^{-3}.

There are two possible types of potential dopants for effective p-type doping in Ga_2O_3: group V anions that substitute one of the oxygen sites, such as N, and group I, II, and IIB cations that substitute one of the gallium sites, such as Li, Mg, and Zn. Kyrtsos *et al.* [153] theoretically investigated the various cation substitutional dopants from group I, II, and IIB for the p-type in β-Ga_2O_3 by using the DFT. All these dopants were found to introduce deep-level acceptors with their ionization energies of more than 1.0 eV. The parasitic effect of trapping an extra hole at a very deep donor level also hinders conversion of p-type conductivity. Lyons *et al.* [293] investigated both anion and cation substitutional dopants in β-Ga_2O_3 for p-type doping theoretically and found that all impurities (N_O, group I, II, and IIB cations) exhibit acceptor transition levels of more than 1.3 eV above the valence band. In comparison, Mg_{Ga} was found to be the most stable impurity in n-type β-Ga_2O_3, and N_O would be unstable in some thermodynamic conditions, such as O-rich conditions and high temperatures [294]. Recently, the doping of β-Ga_2O_3 by nitrogen implantation has been demonstrated with activation temperatures beyond 800°C, but the film is still semi-insulating without any signal of p-type conduction [294–296]. Therefore, high ionization energies of the possible p-type dopants make it difficult to get enough free holes even at high-concentration doping.

Another reason that prohibits p-type conductivity in β-Ga_2O_3 is the prediction of STHs [151,155,284,286], which are energetically more favorable than the delocalized holes in β-Ga_2O_3. The self-trapping energy and the trapping barrier of β-Ga_2O_3 were theoretically calculated to be 0.53 and 0.10 eV, respectively [151]. STHs have been linked with UVL that is widely observed in UID, Si-doped, Mg-doped, and N-doped β-Ga_2O_3 materials [155,284,286]. Electron paramagnetic resonance (EPR) characteristics of neutral Mg acceptors in a Mg-doped β-Ga_2O_3 crystal also indicated that holes were trapped next to the Mg_{Ga} defect, as described as small polarons, and in turn, the deep nature of Mg acceptors is driven by the self-trapping of holes [297]. STHs have also been reported as the origin of large internal gain in Schottky photodiodes [69].

Owing to the strong binding of the oxygen anions, group-III oxides are considerably more ionic than group-III nitrides. As shown in Section 2.C, the band structures of β-Ga_2O_3 have a large splitting between upper and lower valence bands (LVBs). Ga (3d) core-level energies have been observed to overlap in energy with the O(2s)-like LVB states [298], similar to the case of Ga (3d) in GaN [299] and Zn (3d) in ZnO [300]. The resulting resonance causes the Ga (3d) electrons to be strongly hybridized with both the upper and lower s and p orbitals, which have a profound influence on the acceptor levels in β-Ga_2O_3. The potential acceptors with d electrons would have deep levels because of the antibonding repulsion between dopants (3d) and Ga (4p) electrons, whereas dopants without d electrons will form shallower ionization levels. Therefore, Mg will be promising in p-type doping of β-Ga_2O_3, while elements such as Zn, Cd, and Fe may have deep levels and lead to compensated high-resistivity material. In addition, determined from the band structure of β-Ga_2O_3, the top of the valence band is flat, which results in a very high effective hole mass and, consequently, in a very low hole mobility, and also hinders the possible p-type conductivity [275]. The codoping techniques, proven to be effective to improve p-type conductivity in GaN, can improve equilibrium solubility of acceptors and lower ionization energies [301–303]. However, it seems not to be working in β-Ga_2O_3. Tadjer *et al.* [296] have reported on the epitaxial β-Ga_2O_3 grown by the HVPE method with the codoping of Si and N. Nitrogen dopants have a deep acceptor-like level near $E_c - 0.23$ eV and compensate the donors as revealed by photoionization spectroscopy [296].

Therefore, since stable and reliable p-type doping of Ga_2O_3 has not been achieved until now, heterojunctions with other p-type semiconductors have been the topic of intense investigation.

3. Ga_2O_3-BASED UV PHOTODETECTORS AND THE PHYSICS

With the knowledge of fundamental properties and the development of synthesis methods of Ga_2O_3 materials, it is understood that Ga_2O_3 has unique advantages over other common WBG semiconductors, including a suitable bandgap, availability of a single-crystal substrate, and cost-saving growth of heterostructures. Therefore, Ga_2O_3 is a promising candidate in the applications in deep-UV or solar-blind photodetector devices. Benefitting from the development of epitaxial techniques and scaling-up of bulk single crystalline substrates, the solar-blind photodetectors based on bulk, thin films, ternary alloying epilayers, nanostructures, and hybrid heterostructures have been reported. The basic parameters, including photoresponsivity, response speed, and detectivity, are scattered in a quite broad range owing to the different architectures, various phases, and crystalline qualities. Huge photoconductive gains are commonly yielded, and the physical mechanisms behind them are related to the carrier trapping and PPC effects. In the following section, the most recent advances in Ga_2O_3-based solar-blind photodetectors are comprehensively reviewed, and the corresponding working mechanisms and physics have been discussed.

A. UV Photodetectors Based on Ga_2O_3 Bulk, Films, and Ternary Alloys

β-Ga_2O_3 single-crystalline substrates [69,85,136,304–306], different-phase Ga_2O_3 thin films [67,307–319], $(Al_xGa_{1-x})_2O_3$ [320–323], and $(In_xGa_{1-x})_2O_3$ [324–326] ternary alloying films have been used to fabricate deep-UV photodetectors. Due to the UWBG nature of Ga_2O_3 and large work functions of commonly used metals, Schottky contacts are easily formed, and as a result, most Ga_2O_3 photodetectors are Schottky based. The availability of β-Ga_2O_3 substrate with high crystalline, defined doping concentration (10^{17}–$10^{19}\ cm^{-3}$), and high mobility makes it possible to deliver the reported high-performance solar-blind photodetectors, while photodetectors based on thin films grown on foreign substrates could not give full play to the material's advantages on photon detection due to poor quality and uncontrollable electric conductivity. Especially for the Ga_2O_3 material on insulating substrates, the configuration of photodetectors is only the planar type, which requires comb electrodes or their equivalent and leads to a difficulty in enlarging the light-receiving area and narrowing the separation of the electrodes.

In 2008, Oshima *et al.* [304] reported a vertical-type Schottky photodetector based on a CZ growth (100)-oriented β-Ga_2O_3 substrate. To reduce the density of oxygen vacancies and the carrier concentration near the surface, the substrate was thermally annealed at 1100°C for 6 h in an oxygen ambient, which also achieves an atomically flat surface with step and terrace structures, as shown in Fig. 10(a). A Ni/Au (2 nm/8 nm) semitransparent Schottky contact was deposited with an area of 11.8 mm^2 and transmittance range in the DUV region of 34%–38%. Figure 10(b) shows the *I–V* characteristics of the β-Ga_2O_3 photodetector in the dark and under the 250 nm light irradiation. The responsivity biased at 0 V is observable, demonstrating the function of self-powered detection driven by the built-in field. Figure 10(c) shows the room-temperature spectral responses of the β-Ga_2O_3 photodetectors at a reverse bias of 10 V. The measured responsivity exhibits much larger optical gain in the solar-blind spectral region, which has contributed to the occurrence of carrier multiplication in the highly resistive surface region due to the presence of a high electric field up to 1.0 MV/cm [304]. The same group [305] also reported a flame detector based on β-Ga_2O_3 substrate with an inserted semi-insulating interfacial layer, and the Schottky contact was formed by spin coating transparent PEDOT–PSS material. Under the zero-bias operation, the spectral response exhibited a large 250–300 nm injection ratio of 1.5×10^4, and the EQE at 250 nm reached 18%. The transient response was in the order of ms, as shown in Fig. 10(d), which is sufficient for flame sensing. As demonstrated in Fig. 10(e), the detector was successfully employed to distinguish a 1.5 nW/cm^2 light signal in the solar-blind region from a flame under a fluorescent

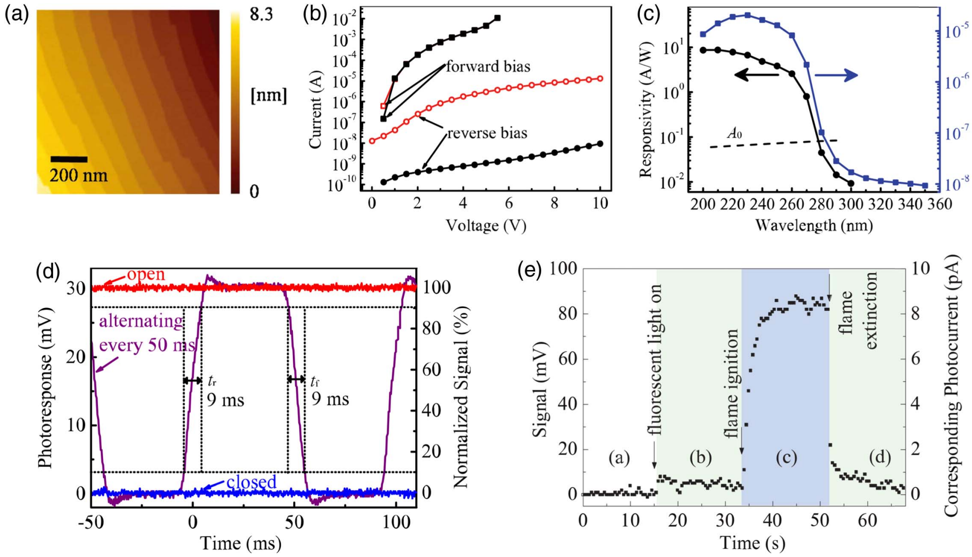

Fig. 10. (a) 1 μm × 1 μm scan image of an annealed surface observed by tapping mode atomic force microscopy. (b) *I–V* characteristics of a photodetector. Closed (black) and open (red) symbols represent current in the dark condition and current in the presence of 250 nm light irradiation, respectively. (c) Photocurrent spectral response (blue) and photoresponsivity of the photodetector (black) at a reverse bias of 10 V. The dashed line indicates the photoresponsivities expected in the case without carrier multiplication. Reprinted with permission from Oshima *et al.* [304]. Copyright 2008 The Japan Society of Applied Physics. (d) Transient response of the detector. (e) Signal from the flame detection system during the demonstration. Reprinted with permission from Oshima *et al.* [305]. Copyright 2009 The Japan Society of Applied Physics.

lamp illumination, indicating the significant potential for practical applications.

Furthermore, Suzuki *et al.* reported on β-Ga_2O_3 photodiodes with an Au (10 nm) Schottky contact fabricated on a single-crystal substrate, and the effect of postannealing in nitrogen ambient at temperatures ranging from 100 to 500°C on the electrical response and photoresponse of the photodiodes has been investigated [85]. Determined from *I*–*V* characteristics of the devices in Fig. 11(a), the ideality factor n values decrease and approach unity upon annealing over 200°C, together with a slight reduction of the barrier height ϕ_b. This is because interface defects, which act as recombination or carrier trapping centers, are reduced greatly in density due to thermal annealing. The spectral responsivities of the photodiode annealed at 400°C and the as-fabricated photodiode at a reverse bias of 3 V are shown in Fig. 11(b), respectively, in which the inset is the photocurrent of the devices under reverse bias voltage to 5 V. A high responsivity of 10^3 A/W at 240 nm was obtained for the device annealed at 400°C, yielding a ηg product of 5.17×10^3. In addition, the photocurrent significantly increases as the reverse bias voltage increases. Such behaviors indicate the presence of internal gain. Several theories, such as defect-assisted tunneling [327], the avalanche process [328], and minority carrier trapping [43], have been proposed to explain the large gain mechanisms in Schottky photodiodes. Determined from the consistent fitting of *I*–*V* forward bias curves in terms of the thermionic emission theory as well as the absence of current abruptly increased at reverse bias, the mechanisms of tunneling or avalanche processes can be excluded, and the most possible gain mechanism is the trapping effect of minority carriers, which have also been reported in GaN Schottky photodiodes [43,44]. For Ga_2O_3 material, the generated holes with a relatively larger capture coefficient are easily trapped by the deep-level defect states due to the diffusion of Au atoms in the neighborhood of the Au-Ga_2O_3 interface within the depletion layer. The physical mechanism responsible for the high internal gain has also been reported to minority carrier (hole) trapping other than carrier multiplication in Ref. [304].

The carrier-trapping-induced high optical gain has also been commonly observed in the photodetectors fabricated with thin films grown on foreign substrates [69,310,315,318]. Guo *et al.* [310] fabricated UV photodetectors with a metal–semiconductor–metal (MSM) structure using β-Ga_2O_3 thin films on sapphire substrates. They found that the *in situ* annealing of β-Ga_2O_3 films in O_2 atmosphere leads to the conversion of contact from Ohmic-type to Schottky-type. Figure 11(c) shows the photoresponse transient properties of the diode upon the 254 nm light illumination under 1 V bias. As compared to the Schottky-type devices, the photocurrent of the Ohmic device is much larger, while the response (or recovery) time is longer. Two temporal components are observed in the rise and the decay edges. The fast-response component is attributed to the rapid change of carrier concentration as the

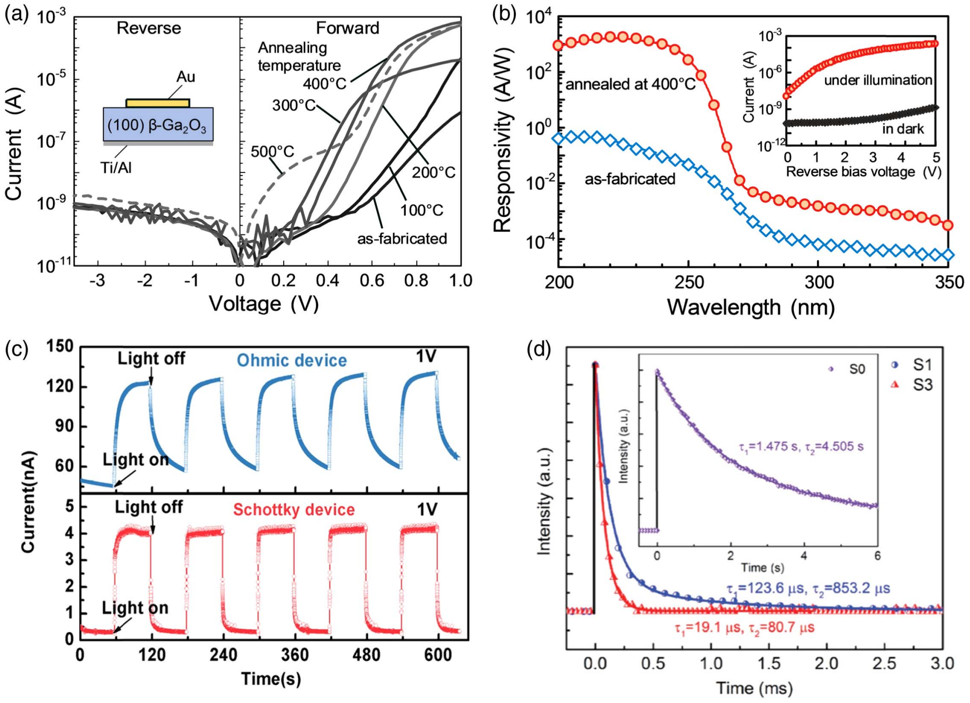

Fig. 11. (a) Dark *I*–*V* characteristics of the Au-Ga_2O_3 Schottky photodiode annealed at various temperatures. The inset shows the device configuration. (b) Spectral responsivities of the photodiode annealed at 400°C and the as-fabricated photodiode at a reverse bias of 3 V. The inset shows the photocurrent of the devices under reverse bias voltage to 5 V. Reprinted with permission from Suzuki *et al.* [87]. Copyright 2009 American Institute of Physics. (c) Time-dependent photoresponse of the β-Ga_2O_3 thin films prototype photodetector to 254 nm illumination: (top) the Ohmic-type device; (bottom) the Schottky-type device. Reprinted with permission from Guo *et al.* [310]. Copyright 2014 American Institute of Physics. (d) Temporal response tests of the PDs with KrF pulse laser illumination at 10 V bias. Reprinted with permission from Cui *et al.* [315]. Copyright 2017 Wiley-VCH Verlag GmbH & Co. KGaA, Weinheim.

light is switched, while the slow-response component is caused by the carrier trapping/releasing owing to the presence of trapping defects. Apparently, the decay times of Schottky devices based on heteroepitaxial layers are about 1 order higher than the photodetector based on Ga_2O_3 high-crystalline bulk material reported by Oshima *et al.* [305], which indicates that defect density within the active absorbing region plays a critical role to determine the response speed and optical gains. Similar phenomenon has also been widely observed in Refs. [69,315,318]. To address the physical origin of high gain, Armstrong *et al.* [16] employed deep-level optical spectroscopy (DLOS) characterization to reveal the roles of STHs in photoresponsivity. They identified that the accumulation of STHs above the valence band of Ga_2O_3 is spatially localized near the Schottky contact, which will cause a reduction of the Schottky barrier and consequently yield a large photoconductive gain. Oxygen vacancies are always abundant in WBG semiconductors such as ZnO and Ga_2O_3, and are widely regarded as deep-level donors acting as carrier trapping centers. To address this issue, Cui *et al.* [315] reported on the controlling of the response speed and responsivity of amorphous Ga_2O_3 solar-blind photodetectors with MSM structures, in which the active layers were grown with different oxygen fluxes in the reactive radio frequency (RF) magnetron sputtering process. The SBH values of the detectors estimated by fitting the dark *I–V* curves gradually increase by ~0.4 eV with increasing oxygen fluxes during the growth. This has been attributed to the upward band bending of Ga_2O_3 induced by negative defect states on the topmost surface of film or surrounding grain boundaries. Owing to the reduction of donor-like oxygen vacancies, the sample grown at high oxygen flux becomes more resistive, hence leading to the low dark current and low optical gains, as well as the fast decay speed, as shown in Fig. 11(d). A fast decay time of 19.1 μs and a responsivity of 0.19 A/W have been achieved for the amorphous Ga_2O_3 films grown under high oxygen flux, which is comparable to the performance of photodetectors based on single-crystal Ga_2O_3 counterparts.

Bandgap engineering in Ga_2O_3 materials with $(Al_xGa_{1-x})_2O_3$ [320–323] and $(In_xGa_{1-x})_2O_3$ [324–326] ternary alloying films enables rational designs of photodetectors to expand the photoresponse spectral region covering from UVA [326] to VUV [323]. Lee *et al.* [320] synthesized ternary $(Al_xGa_{1-x})_2O_3$ films by using a RF magnetron cosputter system with dual targets, and a series of MSM solar-blind photodetectors has been fabricated. The photoresponsivity in Fig. 12(a) indicates that, by increasing the incorporation of Al, the cutoff wavelength of photoresponsivity is tuned from 250 to 230 nm with their corresponding optical bandgaps of 5.0–5.4 eV, and the UV-visible rejection ratio ($>10^3$) keeps increasing as well. Figure 12(b) shows the dependence of the low-frequency noise power density on the operation frequency of the photodetectors at a bias voltage of 5 V. The noise performances were well fitted with a $1/f$ function, which is corresponding to the flicker noise. The total noise current over the bandwidth of 1 kHz and the corresponding NEP decrease for the $(Al_xGa_{1-x})_2O_3$ layers with high Al composition. It is understood that the incorporation of Al increases the number of the Al–O bonds and therefore suppresses the formation of the oxygen vacancies. As a result, the noise performances and detectivity of the resulting MSM DUV–PDs could be improved [320]. The rise and decay times of the temporal response of UV photodetectors based on $(Al_xGa_{1-x})_2O_3$ layers

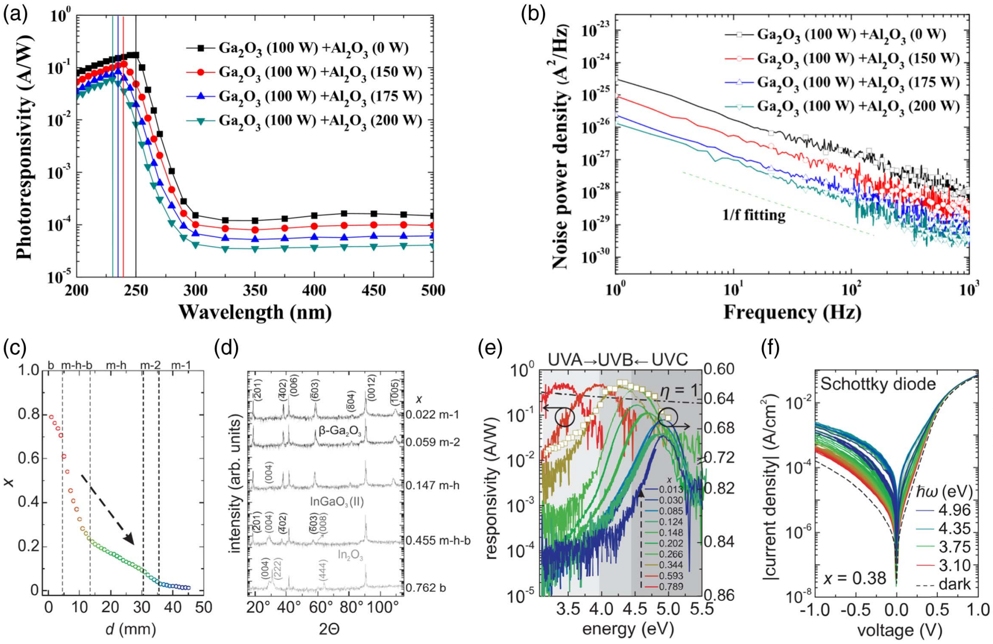

Fig. 12. (a) Photoresponsivity of metal–semiconductor–metal deep ultraviolet photodetectors. (b) Low-frequency noise power density as a function of frequency of metal–semiconductor–metal deep-ultraviolet photodetectors. Reprinted with permission from Lee *et al.* [320]. Copyright 2018 IEEE. (c) EDX line scan along the In gradient (the black dashed lines separate different crystallographic phases); (d) single XRD patterns selected from each phase. (e) Responsivity versus photon energy of 10 MSM-PDs along the In gradient. (f) Spectrally resolved *J–V* measurements of an SC [the analyzed $\Phi_{Bn,eff}$ are shown as squares in (e)]. Reprinted with permission from Zhang *et al.* [326]. Copyright 2016 American Institute of Physics.

with low Al composition have also been reported on the level of seconds [321], indicating that additional defects are generated accompanied by the incorporation of Al due to a serious alloying disorder. Hence, the response speed of the $(Al_xGa_{1-x})_2O_3$-based photodetectors still has much room to be improved, and high-quality ternary alloys are in demand.

On the other hand, for the purpose of a photodetector working in the UVA spectral region, Zhang *et al.* [326] fabricated visible-blind MSM photodetectors based on Si-doped $(In_xGa_{1-x})_2O_3$ ternary film ($0.35\% < x < 83\%$). Carrier concentrations of the resultant films range from 10^{17} to 10^{18} cm^{-3}. A crystallographic phase separation was observed from monoclinic β-Ga_2O_3 via hexagonal $InGaO_3$ (II) to cubic bixbyite In_2O_3, as shown in Figs. 12(c) and 12(d). Figure 12(e) shows that, with the reduction of In composition, the cutoff wavelength of the photoresponsivity is tuned from the UVA to UVC spectral range with the corresponding optical bandgap from 3.22 to 4.83 eV. The relationship of $E_{\text{cutoff}}^{\text{high}}$ and In component x was determined linearly as $E_{\text{cutoff}}^{\text{high}}(x) = (4.86 \pm 0.03) - (2.03 \pm 0.08)x$ (in eV). It is noted that a photoconductive gain was yielded only for PDs fabricated from the In-rich ternary films, but no gain was observed for devices based on the Ga-rich $(In_xGa_{1-x})_2O_3$. To explain this effect, the spectrally resolved *J*–*V* characteristics of the $(In_xGa_{1-x})_2O_3(x = 0.38)$-based photodetector are shown in Fig. 12(f). In terms of the thermionic emission theory, a clear correlation between the increased photoresponsivity and the reduction of an effective Schottky barrier is observed, strongly suggesting that the predominant gain mechanism is attributed to the trapping of photoexcited holes at the metal/$(In_xGa_{1-x})_2O_3$ interface. In addition, a deep-UV phototransistor based on amorphous indium gallium oxide (a-IGO) thin-film transistors (TFTs) has been developed by Chang *et al.* [325]. It is found that the magnitude of the photocurrent is correlated to the densities of oxygen vacancies within the channel of the TFTs. Kokubun *et al.* [324] reported similar dependence of the responsivity on the In component in the visible blind photodetectors based on $(In_xGa_{1-x})_2O_3$ films prepared by the sol–gel method.

In a short conclusion, high-responsivity solar-blind photodetectors based on Ga_2O_3 thin films, bulk crystals, and their ternary oxides have been developed. However, most of these photodetectors are of MSM structure with back-to-back Schottky configurations. Owing to the presence of deep-level traps involved in the material or at the interface of the metal–semiconductor interface, the internal gain of devices usually exceeds the theoretical maximum of $\eta = 100\%$. As stated in Section 1.B.2, the physical mechanism responsible for the large gains is identified to be dominated by the minority carrier trapping effect. The associated *I*–*V* characteristics cannot be well described in the framework of the thermionic emission theory as well. Especially for the Schottky photodiodes, photon-generated holes trapped at the electrode–semiconductor interface or oxygen vacancies have been proven to lower the SBH under irradiation. The responsivity will differ under different light intensity below the saturation light intensity and the applied voltage. For use in quantitative radiometric applications, the challenge is that these devices would require exquisite control and stability of the reverse bias supply. On the other hand, the sensitivity of responsivity to reverse bias is similar to the characteristics of a photomultiplier tube (PMT) with significant gains. If the dependence of photoresponsivity on the bias can be quantitatively calibrated, it also provides an opportunity to be applied in the field of low-flux detection. The current state of Ga_2O_3 photodetectors with high internal gains may be well suited to use as high-accuracy radiometric detectors for the sensing of weak-signal photon fluxes, especially in solar-blind UV spectral regions. Nevertheless, for the practical usage of UV photodetectors, breaking the trade-off between high responsivity and high response speed is critical. Ga_2O_3 nanostructures and heterostructures may be alternatives to achieve this goal.

B. UV Photodetectors Based on Ga_2O_3 Nanostructures

Ga_2O_3 NWs [203,207,214,238,239,266,267,329–333], NBs [237,254,256], NSHs [258,259], and quasi-2D nanoflakes fabricated using mechanically exfoliated β-Ga_2O_3 [167–170] and its heterostructures [240,264,271,334] have been widely used to fabricate UV photodetectors. With high-crystalline quality, Ga_2O_3 nanostructures are usually regarded as a promising platform to deliver high-performance photodetectors with fast response speed, high signal-to-noise ratio, low energy consumption, and low fabrication cost. Ga_2O_3 photodetectors fabricated using quasi-2D nanoflakes mechanically exfoliated from bulk substrate are expected to inherit the advantages of bulk crystal and nanostructures. Photodetectors fabricated based on a heterostructure with a core–shell nanostructure have been reported to achieve the avalanche process with high gain and fast response speed [240]. To improve the reproducibility of Ga_2O_3 nanostructure photodetectors, nanofilm photodetectors have also been attempted [203,238,329–331,333]. Nanofilm photodetectors have obvious merits over other devices based on bulk, thin films, and 1D nanostructures, such as easy fabrication, low cost, flexibility, and high performance [203,335].

Owing to the easy synthesis of 1D β-Ga_2O_3 NWs, solar-blind photodetectors were first developed on individual β-Ga_2O_3 NWs using Au electrodes as the metal contact [266]. High-crystalline-quality NWs were grown using Au as a catalyst at a high temperature of 980°C. Under 254 nm light illumination, the *I*–*V* curve of the device was asymmetric and nonlinear [266]. Such a behavior was ascribed to the poor Ohmic contact between the electrodes and the NW, which could be attributed to the extremely low free-carrier density in the NW, and the mismatch of the work function between the NW and the Au electrodes. Figures 13(a) and 13(b) show the temporal response of the detectors upon 254 nm light illumination at a bias of −8 V. The conductance of the NW increases by about 3 orders of magnitude, and the upper limits of the response and recovery time are 0.22 and 0.09 s, respectively. In general, for this sort of photoconductive detectors, the device usually suffers from a large dark current and a long recovery process. However, these issues do not occur in these NW detectors, which may be related to the small dimensions of NWs and depletion of shells due to upward band-bending effect. The exact mechanism has not been given by the authors, and further investigations on the physics behind it are needed. To further improve the sensitivity performance of the device,

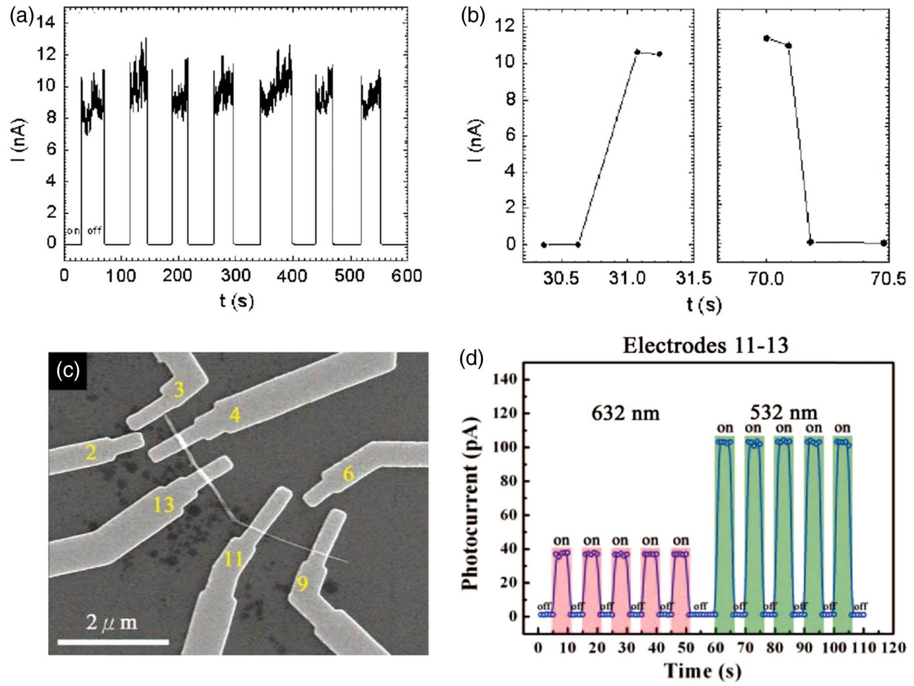

Fig. 13. (a) Real-time photoresponse of the detector to 254 nm light. (b) Enlarged rise and decay edges for the first "ON" and "OFF", respectively. Reprinted with permission from Feng *et al.* [266]. Copyright 2006 American Institute of Physics. (c) Enlarged SEM images of the photo switch made of an individual Au-in-Ga_2O_3 peapod nanowire. (d) Photoresponse behaviors during illumination ON and OFF cycles between electrodes 11–13. Reprinted with permission from Hsieh *et al.* [207]. Copyright 2008 American Chemical Society.

a novel 1D photo switch made of Au-in-Ga_2O_3 peapod NWs was designed by Hsieh *et al.*, as shown in Fig. 13(c) [207]. Surface plasmon resonance (SPR) induced by the embedded Au particles substantially enhances the photoresponse of an individual NW. Figure 13(d) exhibits that the device photoresponse revealed a high on/off rejection ratio during one cycle, which indicates that such a simple synthetic approach may expand the possible application of Ga_2O_3 optoelectronic devices.

The assembly of β-Ga_2O_3 NWs into high-performance photodetectors by using an effective bridging method was reported by Li *et al.* [331]. The device was made in a single-step CVD process on quartz substrates using Au as the catalyst. High performance was yielded with a high 250–280 nm rejection ratio ($\sim 2 \times 10^3$), a low photocurrent fluctuation ($<3\%$), and a fast decay time ($\ll 20$ ms). To address the effect of defects and crystalline quality on the device performance, a series of samples synthesized at different temperatures from 800°C to 1000°C has been used as the active absorbing layer. The time-dependent photocurrent, responsivity, and the PL spectra shown in Figs. 14(a)–14(c) identified that the defect density increases with decreasing growth temperature. With more defects involved in the NWs, more serious trapping of the photogenerated holes occurs, resulting in higher photoconductive responsivity but a sacrifice of the response speed [Fig. 14(d)]. Therefore, improvements of the device response speed can be achieved by reducing the defect density. In addition, a vertical Schottky photodiode based on Au/β-Ga_2O_3 NW array film has been demonstrated by a simple thermal partial oxidation process [203]. A schematic illustration of the fabrication of the β-Ga_2O_3 NW array film and its vertical Schottky photodiode is shown in Fig. 14(e). The photodiode exhibits a rectifying property under the dark condition with a current rectification ratio of 10^5 at ± 15 V. It is easy to conclude that the interfacial layer or the β-Ga_2O_3 active layer is highly resistive with a series resistance of $R_S \approx 10^8$ Ω determined from forward I–V curves [Fig. 14(f)]. Under 254 nm light illumination with an incident power density of 2 $\mathrm{mW/cm^2}$, distinct photocurrents have been observed in the forward region, which is attributed to the reduction of resistance of the NW films because of the photogenerated excess carriers under illumination, as suggested by Suzuki *et al.* [67]. A typical photovoltaic effect could be observed clearly in the inset of Figs. 14(f) and 14(g), from which the solar-blind photodetector is self-powered with a fast response speed. Figure 14(h) shows the temporal response of the photodetector under −10 V bias and illuminated by a DUV laser with a wavelength of 266 nm and a pulse width of 10 ns. The rise and decay times are estimated to be 1 μs and 64 μs, respectively, and the current drops to zero at about 100 μs. The slow decay component may be caused by the RC constant in the circuit as estimated to be ∼54 μs. As compared to devices based on bulk, thin films, and individual nanostructures, the reported photodetectors based on NW films exhibit high performance with fast response speeds, a self-powered function, excellent stability, and good reproducibility, and they therefore represent to date one of the most promising technical solutions for flexible UV detection [238,329,330,333,335].

Besides synthesis of 1D nanostructures, another unique feature of Ga_2O_3 is that 2D nanostructures can be easily obtained by direct oxidation [258], exfoliation from bulk [167–170], and CVD processes [237,254,256,259]. Feng *et al.* [258] first reported on the synthesis of 2D Ga_2O_3 by oxidation of GaSe NSHs and subsequent fabrication of solar-blind photodetectors based on 2D Ga_2O_3 NSHs. Figure 15(a) shows that the as-prepared 2D β-Ga_2O_3 is polycrystalline with a thickness less than 10 nm, which is the thinnest 2D β-Ga_2O_3 photodetector ever reported, to the best of our knowledge. The responsivity and EQE are 3.3 A/W and 1600%, respectively. The photo switch measurement under 254 nm illumination indicates that the on/off ratio is about 10, and the rise and decay times are 30 ms and 60 ms, respectively. Except for the large dark current, the device performance is acceptable, and it presents an alternative to realize 2D Ga_2O_3 photodetectors with a simple and low-cost approach. Alternatively, high-quality β-Ga_2O_3 2D NSHs have been synthesized via the CVD method, and solar-blind photodetectors were demonstrated as well [259]. The *I–V* measurements under the dark condition [Fig. 15(b)] indicate that the photodetector exhibits typical Schottky rectifying behaviors, and the β-Ga_2O_3 2D NSHs without doping are highly resistive. Therefore, the *I–V* characterization of the device under illumination of 254 nm light shows a typical photovoltaic effect, and a high response phenomenon is also observed in the forward bias region, as shown in Fig. 15(c), similar to the results reported in Refs. [67,203]. The resultant photodetector performs a high responsivity (19.31 A/W at forward bias of 1 V), an ultrahigh EQE value of 9427%, a fast response speed (about 20 ms), and a low dark current. Normally, Schottky photodiodes usually work under reverse bias with much lower dark current and efficient separation of photogenerated carriers in the expanded depletion region, and the unusual working in the forward bias

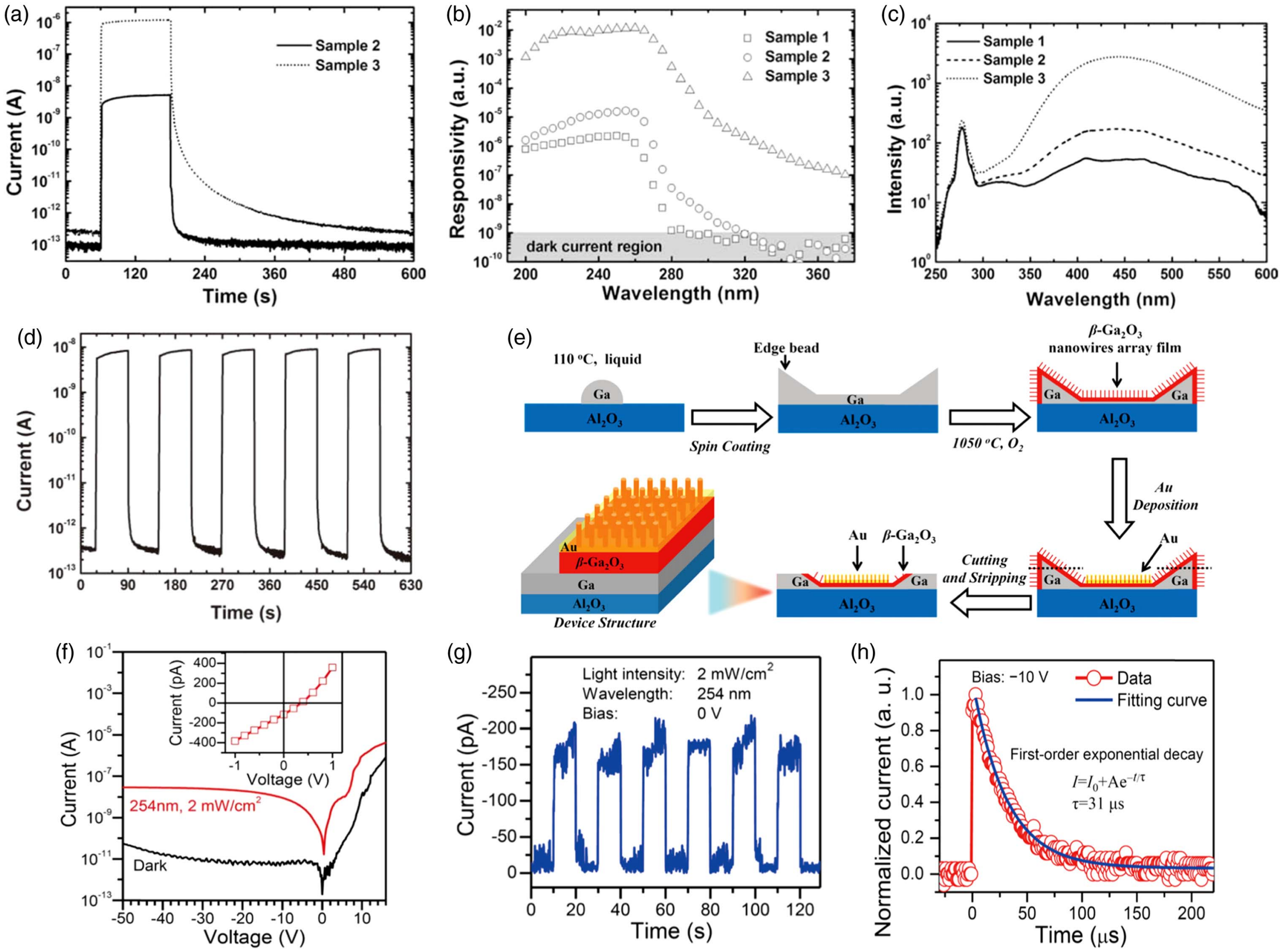

Fig. 14. (a) Time-dependent photoresponse of the bridged β-Ga_2O_3 NWs grown at 925°C (sample 2, solid line) and at 800°C (sample 3, dotted line) measured in dry air under a bias voltage of 5 V and a UVC (254 nm) irradiance of ~2 $mW \cdot cm^{-2}$. The photocurrent to dark current ratios for sample 2 and sample 3 were ~5×10^4 and ~5×10^6, respectively. (b) Spectral responses of sample 1 (squares), sample 2 (circles), and sample 3 (triangles). (c) Room-temperature PL spectra of sample 1 (solid line), sample 2 (dashed line), and sample 3 (dotted line), revealing an increase in defect emissions with decreasing growth temperature. (d) Time-dependent photoresponse of the bridged β-Ga_2O_3 NWs (sample 1). Reprinted with permission from Li *et al.* [331]. Copyright 2010 Wiley-VCH Verlag GmbH & Co. KGaA, Weinheim. (e) Schematic illustration of the fabrication of the β-Ga_2O_3 nanowire array film and its vertical Schottky photodiode. (f) *I–V* characteristics of the device in the dark and under the illumination of 254 nm light in the logarithmic scale. Inset shows the photovoltaic characteristic of the device near zero bias. (g) Time-dependent photocurrent response of an Au/β-Ga_2O_3 nanowire array film Schottky photodiode measured under 254 nm light illumination with the intensity of 2 $mW \cdot cm^{-2}$ at 0 V. (h) Decay edge of the current response at a reverse bias of 10 V. Reprinted with permission from Chen *et al.* [203]. Copyright 2016 American Chemical Society.

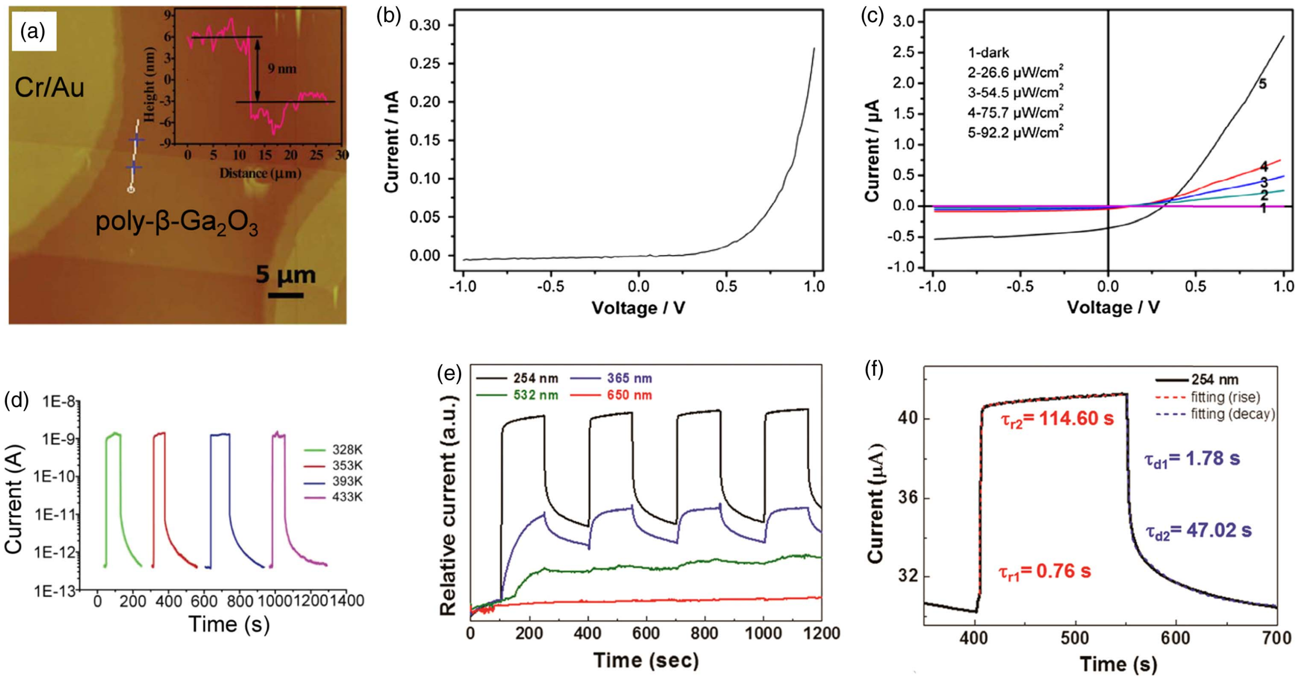

Fig. 15. (a) Atomic force microscopy image of a 2D β-Ga_2O_3 photodetector; inset, the corresponding height profile of the photodetector. Reprinted with permission from Feng *et al.* [258]. Copyright 2014 Royal Society of Chemistry. (b) *I–V* characteristics of the device in the dark. (c) *I–V* characteristics of the device under irradiation with 254 nm light at different light intensities. Reprinted with permission from Zhong *et al.* [259]. Copyright 2015 Elsevier B.V. All rights reserved. (d) The ON/OFF cycle of the β-Ga_2O_3 nanobelt device upon 250 nm light illumination from the RT to 433 K under the intensity of 9.835×10^{-5} W/cm² at a bias of 6.0 V. Reprinted with permission from Zou *et al.* [256]. Copyright 2014 Wiley-VCH Verlag GmbH & Co. KGaA, Weinheim. (e) Time-dependent photoresponse of the fabricated photodetector under various illumination conditions (254, 365, 532, and 650 nm light exposure). (f) Experimental and fitted curves of the current rise and decay process at 254 nm illumination under a gate bias of 0 V. Reprinted with permission from Oh *et al.* [169]. Copyright 2016 Royal Society of Chemistry.

may sacrifice the response speed. Zou *et al.* [256] have also reported solar-blind photodetectors based on β-Ga_2O_3 (100)-oriented NBs configured in a typical MSM structure. A high responsivity of 851 A/W and a response time less than 0.3 s have been achieved. In particular, these β-Ga_2O_3 NB photodetectors can work at a temperature up to about 433 K. Figure 15(d) shows that the photon-excited current remained constant with negligible changes in response speed when the operation temperature increased from 328 to 433 K at a fixed bias of 6.0 V. The reverse dark leakage current at 20 V slightly increases from 2.2×10^{-13} A to 2.41×10^{-12} A as the temperature rises to 433 K.

Similar to the fabrication of graphene, quasi-2D β-Ga_2O_3 flakes can be mechanically exfoliated from the β-Ga_2O_3 bulk material and transferred on other foreign substrates for specific applications. For instance, Oh *et al.* [169] fabricated back-gated phototransistors based on exfoliated quasi-2D β-Ga_2O_3 flakes, and the highest recorded responsivity of 1.8×10^5 A/W was reported. Figure 15(e) shows that the reported phototransistor has the distinct spectral photoresponse to photons with energy lower than the bandgap energy of β-Ga_2O_3 (365 nm and 532 nm). The generation of the photocurrent under 365 nm and 532 nm illumination is due to the impurity or defect levels within the bandgap, which results in carrier trapping in subgap energy levels and prevents charge–carrier recombination. Therefore, the highest recorded responsivity is yielded at the price of a slow response speed due to the PPC effect. Indeed, the slow decay component reaches around 50 s even at a bias of −50 V, as shown in Fig. 15(f), which is a typical sign of the PPC effect induced by carrier trapping in deep-level defects. Similar results have been obtained in the photodetectors fabricated by the combination of exfoliated flakes and graphene electrodes [168]. As compared to the performance of Ga_2O_3 nanoflake MSM photodetectors using Ni/Au electrodes, the Ga_2O_3/graphene photodetectors exhibited high responsivity and slow response speed. Though efforts have been contributed on photodetectors based on Ga_2O_3 nanoflake exfoliated from bulk, the overall performance still needs to be improved especially for high-speed application. For mass production, the reproducibility of the 2D nanoflakes with defined thickness and large area remains the dominant challenge.

As discussed above, the trade-off between responsivity and response speed still occurs in most photodetectors based on Ga_2O_3 films or nanostructures. To overcome the trade-off between the gain and bandwidth performance of a traditional photodetector, the avalanche photodetector (APD) can spontaneously achieve high responsivity and high speed by impact-ionization-induced carrier multiplication. Based on highly crystallized ZnO–Ga_2O_3 core–shell microwires, Zhao *et al.* reported the first Ga_2O_3 solar-blind APD [240]. Figure 16(a) displays the schematic diagram of the microwire photodetector, where the In and Ti/Au are used to form Ohmic contact with ZnO and Ga_2O_3, respectively. The dark *I–V* curve shown in Fig. 16(b) exhibits a typical junction-rectifying property, and a breakdown voltage occurs at 4.3 V with a corresponding breakdown field of about 100 kV/cm if assuming all were applied on the Ga_2O_3 side at room temperature. Determined from the reverse current under different temperatures shown in Fig. 16(c), it can be easily observed that the breakdown voltage increases with the increase in temperature from 300 to 370 K. Hence, a positive temperature coefficient is estimated to be 0.03 V/K, a typical sign of a photodiode working at an avalanche mode. Figure 16(d) is the spectral response of the device at −6 V bias. The device responsivity can reach up to 1.3×10^3 A/W under the reverse bias of 6 V, and the corresponding detectivity is as high as $9.91 \times 10^{14}\ \mathrm{cm \cdot Hz^{1/2}/W}$. The device also shows a fast response speed with a rise time shorter than 20 μs and a decay time of 42 μs, as shown in Fig. 16(e). The possible mechanisms were proposed to explain the avalanche process in terms of the energy band diagram of ZnO and Ga_2O_3 and electric potential distribution simulation in Fig. 16(f). Under a reverse bias, the electrons move from ZnO to Ga_2O_3, and a depletion region mainly on the Ga_2O_3 side acts as an electron-accelerating region. Near the breakdown point, electrons are accelerated and gain enough kinetic energy to cause ionized impact within the Ga_2O_3 lattice to launch the avalanche process. Under illumination, the photogenerated carriers are involved in the avalanche multiplication process and result in high internal gain. However, at room temperature, if the electrons are accelerated in the whole depletion region with no energy loss near the breakdown voltage, the kinetic energy of electrons is only 4.3 eV, which is smaller than the bandgap of Ga_2O_3 and not able to excite electron–hole pairs by impact ionization. Therefore, there are some doubts about the mechanism of the avalanche process in this reported device, and a deeper understanding of the transport mechanism is needed. More experiments on the avalanche process in Ga_2O_3 should be done to evaluate the possibility of Ga_2O_3-based APDs.

Overall, various types of nanostructures have been applied in solar-blind UV photodetectors. Though some individual NWs and 2D nanostructure-based photodetectors were reported with high performance, the reproducibility is the most troublesome problem for practical applications. NW-film-based solar-blind photodetectors have the advantages of easy fabrication, low cost, flexibility, modest performance, and good reproducibility. From the viewpoint of material synthesis, bulk single crystals, thin films, and nanostructures are of the β phase, while photodetectors based on the other metastable phases are rarely reported. For instance, high-quality corundum α-Ga_2O_3 and orthorhombic ε-Ga_2O_3 have been epitaxially achieved on foreign substrates, including sapphire, AlN, ZnO, SiC, and GaN. Unique properties such as a larger bandgap of α-Ga_2O_3 and the ferroelectric properties of ε-Ga_2O_3 may be favorable for further improving the device performance.

C. UV Photodetectors Based on Ga_2O_3 Heterostructures

Currently, due to the lack of p-type conduction of Ga_2O_3, mostly photoconductors and MSM detectors are reported. An alternative way to realize photovoltaic detectors is the integration of heterostructures with other materials that show p-type conduction or larger band offset with respect to Ga_2O_3. To date, Ga_2O_3 heterostructure-based photodetectors have been reported by combining with other functional semiconducting materials including GaN [336–341], SiC [342–344], ZnO [181,240,271,345–347], Si [348,349], graphene [350,351], diamond [10], and SnO_2 [352]. For a heterostructure, especially a hybrid p–n junction, a depletion region with a built-in field will be formed at the interface of the two different materials. Consequently, these photovoltaic-type photodetectors exhibit the self-powered and zero-energy-consumption properties driven by the built-in field. For an n–N isotype

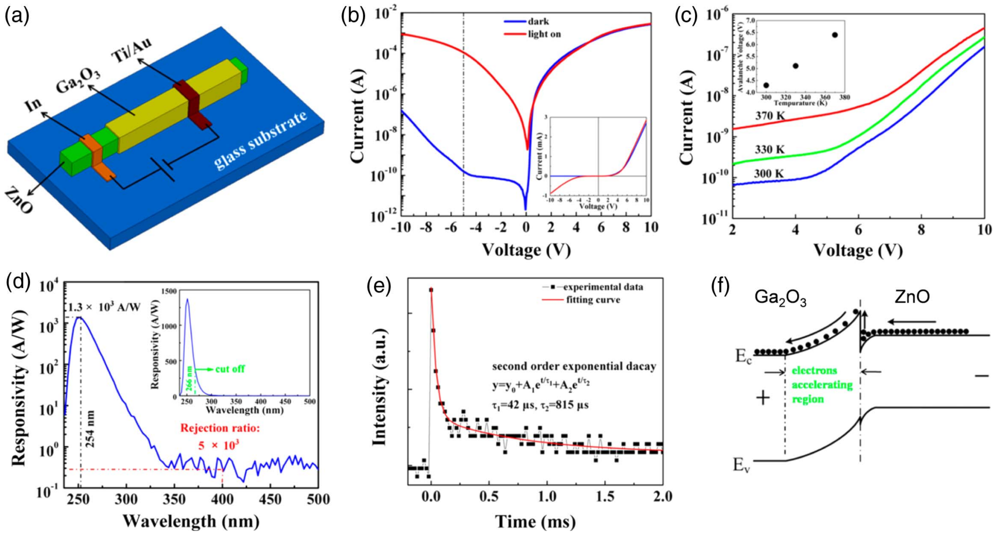

Fig. 16. (a) Schematic diagram of the APD device. (b) *I–V* characteristics of the photodetector under dark and illumination conditions with 254 nm light of 1.67 $\mathrm{mW/cm^2}$. (c) *I–V* characteristics at 300, 330, and 370 K in the reverse voltage under the dark condition; the inset shows the dependence of the avalanche breakdown voltage on the recording temperature. (d) Spectral response of the device at −6 V bias. (e) Transient response of the device at −6 V bias and a second-order exponential fit of the data. (f) Energy band diagram of the APD device in reverse bias. Reprinted with permission from Zhao *et al.* [240]. Copyright 2015 American Chemical Society.

heterostructure, a large band offset is essential to create a depletion region due to the band-bending effect at the interface, which can behave like a p–n junction with good rectifying characteristics. Therefore, the band alignment between the semiconductor and Ga_2O_3 should be taken into account first for the design of an n–N isotype heterostructure with type-II energy band alignment. The band alignment of β-Ga_2O_3 with various materials, including Si [353], GaN [354,355], 6H-SiC [356], AlN [357], α-Ga_2O_3, [358], and dielectric layers, has been investigated and summarized [359].

Nakagomi *et al.* [342] initially reported on a deep-UV photodiode based on a heterojunction composed of β-Ga_2O_3 and p-type (0001) 6H-SiC. The β-Ga_2O_3 layer (200 nm) was synthesized on a p-type 6H-SiC substrate through gallium evaporation in oxygen plasma, and thus vertically structured devices were fabricated. Figure 17(a) shows the *I*–*V* characteristics in the dark and under illumination, respectively. A typical rectifying behavior was observed with a turn-on voltage of 1.6–1.9 V and a low reverse current at about the nA level. The photocurrent is 3 orders of magnitude higher than the dark current, and a high responsivity is yielded for the spectral region from 210 to 260 nm. The response to illumination at wavelengths longer than 260 nm is related to the absorption by the SiC substrate. Ga_2O_3 and the 6H-SiC substrate were expected to form a type-II staggered gap heterostructure. Due to much lower carrier concentration in β-Ga_2O_3 than in the 6H-SiC substrate, the depletion region under 2 V in reverse is mainly located at the β-Ga_2O_3 side, and therefore, high responsivity to light with wavelengths shorter than 260 nm is expected. To suppress the responsivity for wavelengths longer than 260 nm, it is necessary to increase the doping level of the 6H-SiC substrate or work in a reduced reverse bias, for instance, zero bias. The transient response of the β-Ga_2O_3/6H-SiC photodiode working under a reverse of 2 V is shown in Fig. 17(b) with a silicon p–i–n diode under the same illumination condition for comparison. It was found that the photocurrent responds quickly with a rise time within 1.2 ms and a decay time within 1.5 ms. Considering the trapezoidal waveform of light through a light chopper, the actual response time of the photodiode is overestimated. Recently, the performance of a β-Ga_2O_3/p-type

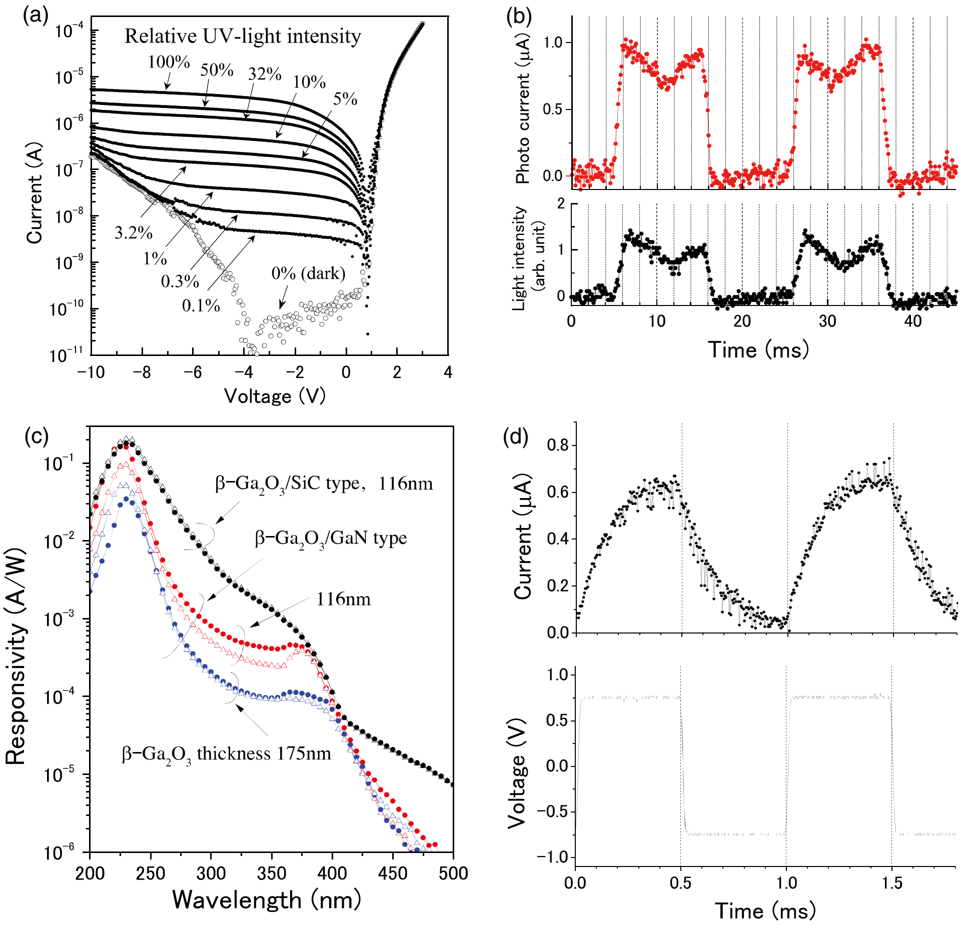

Fig. 17. (a) Dependence of current–voltage characteristics on intensity of UV light illumination of a deuterium lamp. (b) Top, reverse-current response of a photodiode to deep-UV light pulses (reverse-bias voltage is 2 V); bottom, light waveform measured by a silicon pin photodiode for the same light pulses. Reprinted with permission from Nakagomi *et al.* [342]. Copyright 2013 American Institute of Physics. (c) Spectral response of photodiodes based on a β-Ga_2O_3/GaN heterojunction with 116 nm and 175 nm thick β-Ga_2O_3 layers and based on a β-Ga_2O_3/SiC heterojunction with a 116 nm β-Ga_2O_3 layer. (d) Top, response of a photodiode to deep-UV light pulses with a reverse-bias voltage of 2 V; bottom, light waveform measured with a silicon APD module for the same light pulses. Reprinted with permission from Nakagomi *et al.* [340]. Copyright 2015 Elsevier B.V. All rights reserved.

4H-SiC photodiode has been improved [344]. The spectral responsivity at long wavelengths was reduced, and the response time decreased to about 30 μs as compared to the photodiode discussed in Ref. [342].

Nakagomi *et al.* [340] also demonstrated a photodiode based on a β-Ga_2O_3/p–GaN heterojunction with the out-of-plane orientation relationship of β-$Ga_2O_3(\bar{2}01)//GaN(0001)$. A similar rectifying behavior in the dark condition and a responsivity of 0.18 A/W are obtained at a wavelength of 225 nm. As shown in Fig. 17(c), the long wavelength threshold of the spectral response almost corresponds to the bandgap energy of β-Ga_2O_3 material, and a responsivity peak near 375 nm is contributed by the band-to-band absorption of GaN. The pattern of the spectral response is similar to that for a reported Ga_2O_3/GaN heterostructure UV detector [336–339], and the corresponding transient response, as shown in Fig. 17(d), indicates a short response time of 0.3 ms. The photoresponse characteristics both on responsivity and response speed are superior to the β-Ga_2O_3/6H-SiC photodiode, as discussed above [342], as well as the single-crystal β-Ga_2O_3 UV photodetector reported by Oshima *et al.* [305]. Considering the absence of p-type Ga_2O_3, the design of p–n heterojunction photodiodes on foreign p-type WBG semiconductors is a compromising way to realize high-performance solar-blind UV detectors.

Practically, for the detection of weak UV signals, the APD is an ideal candidate to break the trade-off between responsivity

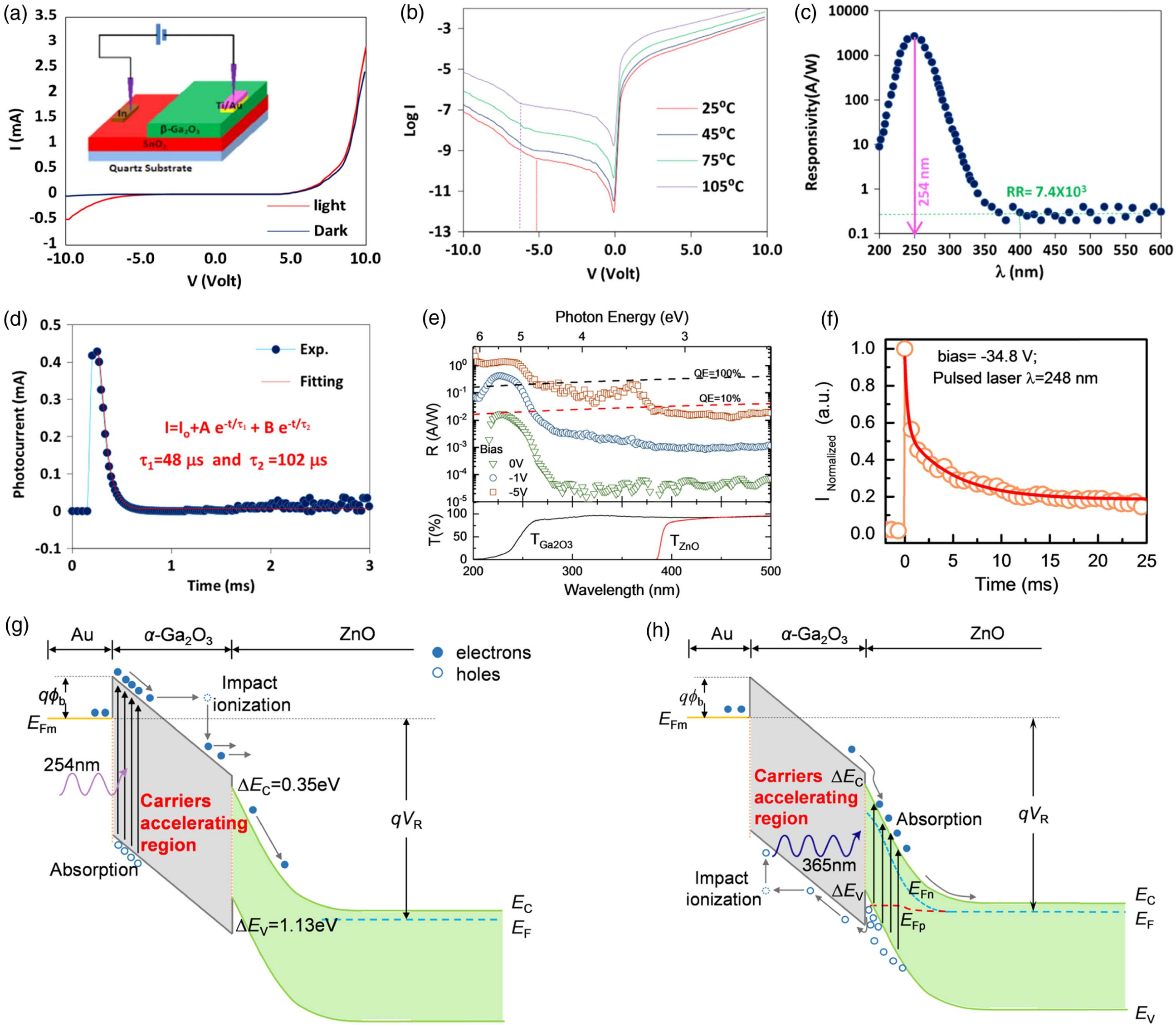

Fig. 18. (a) *I–V* characteristics of the β-Ga_2O_3/SnO_2 bilayer under the dark and illumination conditions (inset shows the construction of the developed device). (b) Dark current versus voltage at various temperatures. (c) The spectral response of the device at −5.5 V bias. (d) The transient response of the device at −5.5 V bias under pulsed 254 nm light illumination and a second-order exponential fit of the data. Reprinted with permission from Mahmoud [352]. Copyright 2016 Elsevier B.V. All rights reserved. (e) Spectral photoresponse of a Schottky diode under different biases and the transmittance spectra of the Ga_2O_3 epilayer and ZnO substrate. (f) The normalized transient photoresponse characteristics measured under reverse biases of −34.8 V (calculated) at room temperature. (g) and (h) Schematic energy diagrams at high reverse bias under 254 and 365 nm illumination, respectively. Reprinted with permission from Chen *et al.* [181]. Copyright 2017 American Chemical Society.

and response speed [240], in which high multiplication gain is achieved through impact ionization processes [360]. In APDs, a high electric field is necessary for the avalanche process, which is often delivered by the formation of the p–n junction [18,361]. Unfortunately, as an intrinsic n-type semiconductor, it is difficult to realize p-type conduction of Ga_2O_3 material. Alternatively, the control of band discontinuities at n–n isotype heterostructures also allows independent manipulation of carrier injection, carrier confinement, and ionization thresholds in high-speed optoelectronic devices [240,352]. Mahmoud [352] initially reported on the development of an APD based on the β-Ga_2O_3/n-SnO_2 isotype heterostructures. Figure 18(a) shows that the I–V characteristic curve of the device under dark and illumination exhibits typical single-junction rectifying features. Figure 18(b) displays that the threshold voltage in reverse bias increases from 5.2 to 6.3 V as the temperature is increased from 25°C to 105°C, indicative of a positive temperature coefficient of 0.016 V/°C. It is a sign that the breakdown processes are dominated by the avalanche multiplication mechanism in the depletion region of the Ga_2O_3 side. With the help of the avalanche process, this photodiode shows high selectivity at 254 nm light illumination with an ultrahigh responsivity of 2.3×10^3 A/W [Fig. 18(c)], an avalanche gain of 1.7×10^5, and a fast decay time of 42 μs [Fig. 18(d)] at a reverse bias of 5.5 V. However, the breakdown fields in these structures are much lower than the critical value for avalanche multiplication effects, and the physical mechanisms of impact ionization of electrons and holes are still under debate.

Recently, Chen *et al.* reported on the growth of single-phase α-Ga_2O_3 epilayers on nonpolar ZnO $(11\bar{2}0)$ substrates for the first time, and a high-performance Au/α-Ga_2O_3/ZnO isotype heterostructure-based Schottky barrier avalanche diode was demonstrated [181]. The device exhibits self-powered functions with a dark current lower than 1 pA, a UV-visible rejection ratio of 10^3, and a detectivity of $9.66 \times 10^{12}\ \mathrm{cm} \cdot \mathrm{Hz}^{1/2} \cdot \mathrm{W}^{-1}$. When a reverse bias of 5 V was applied to the detector, dual-responsivity bands with cutoff wavelengths at 255 and 375 nm were observed, as shown in Fig. 18(e), which is similar to the discussions of Ga_2O_3/SiC and Ga_2O_3/GaN p–n heterojunction photodetectors. The dual responsivity bands indicate that the photodetector can be used in bias-tunable UV photodetection in UVC and UVA spectral regions. The avalanche breakdown voltages shift from 29.5 to 34.0 V as the temperature increases from 298 to 373 K, yielding a positive temperature coefficient of $0.065\ \mathrm{V} \cdot \mathrm{K}^{-1}$. The electric field of the device was simulated to be over 2 MV/cm under a reverse bias of 30 V. Figure 18(f) shows the normalized transient photoresponse characteristics measured under a reverse bias of −34.8 V (calculated) at room temperature. The decay time of the fast-decay component was fitted to be 238 μs, which is caused by the avalanche process. Because of the differences in excitation locations and transport paths of excess carriers under 254 and 365 nm light irradiation, the electrons and holes can be selectively injected into the active region to initiate the avalanche process in the same device, as shown in Figs. 18(g) and 18(h). Therefore, the ionization coefficient of electrons (α) and holes (β) is determined to be $10^5\ \mathrm{cm}^{-1}$ and $10^4\ \mathrm{cm}^{-1}$. The low ratio of hole and electron ionization coefficients $k \approx 0.1$ holds promise for high-speed, low-noise, and stable APD. However, other conduction mechanisms, like Poole–Frenkel (PF) emission due to the presence of dislocations and deep donor-like oxygen vacancies, make the dominant contribution to the leakage current until the onset of the breakdown point. The leakage current induced by PF emission may act as an unstable issue and reduce the reliability of the device. The mechanisms of the avalanche process in the Ga_2O_3 heterojunction are still far from completion, and further efforts are needed to explore the possibility of the avalanche processes in Ga_2O_3 without forming a p–n junction.

4. SUMMARY AND OUTLOOK

In summary, the newest exciting progresses on high-performance solar-blind photodetectors based on Ga_2O_3 materials have been presented, and mechanisms for high internal gain have been explored, to the best of our knowledge. Table 4 is a benchmark of solar-blind photodetectors based on Ga_2O_3 in various forms of bulk, epilayer, ternary alloys, NWs, and heterostructures. Overall, Ga_2O_3-based photodetectors have demonstrated high responsivity and acceptable response speed, indicating that Ga_2O_3-based solar-blind photodetectors as key building blocks have great potential in UV detection technologies towards various military and civil applications. APDs based on Ga_2O_3 isotype heterostructures have also demonstrated simultaneously high responsivity and fast response in terms of the ionization-impact-induced multiplication process. For tuning the sensitivity wavelength for specific applications, $(Al_xGa_{1-x})_2O_3$ and $(In_xGa_{1-x})_2O_3$ ternary oxides photodetectors have been reported to expand the responsivity spectrum from the VUV to UVA spectral regions. Owing to unique properties such as a high electrical breakdown voltage and high resistance to radiation damage [362–364], Ga_2O_3-based photodetectors have a strong capability of operating in high temperature, high field, and harsh environments. These fascinating achievements earned so far would encourage expertise to tackle new challenges and to realize the full potential of Ga_2O_3 materials in UV optoelectronic applications.

Although various Ga_2O_3-based solar-blind photodetectors have been designed and demonstrated high-efficiency performance, several remaining challenging issues require proper solutions to take full advantage of superior physical properties of Ga_2O_3 and to deliver significant improvements in performance for practical applications. One challenge is how to achieve a high-efficiency photodetector without sacrificing the response speed. The response speed of most photoconductive or Schottky-based detectors is still far from the desired due to the trapping effect of photo-excited carriers by defects distributed within the material or in the surface/interface regions. Thus, a thorough physical study is in demand to gain deep understanding of defect behaviors and associated photoconductive gain mechanisms. To suppress the origin of the trapping effect, more efforts are required to reduce the dislocation and defect densities by optimizing the epitaxial process. Meanwhile, further development of the proper fabrication processes, such as low-damage etching, surface passivation, and impurity diffusion control, can be expected to eliminate the PPC origins.

Table 4. Summary of the Reported Basic Parameters of Representative Ga_2O_3 Photodetectors

			Decay Time (μs)			
Material	**Structure**	**Responsivity (A/W)**	τ_1	τ_2	**Rejection Ratio**	**Reference**
bulk	vertical–Schottky	3.7×10^{-2}@250 nm	9×10^3		1.5×10^4	Oshima *et al.* [305]
bulk	vertical–Schottky	10^3@240 nm	–		$\sim 10^6$	Suzuki *et al.* [85]
a-Ga_2O_3	film-based MSM	1.9×10^{-1}@254 nm	19.1	80.7	–	Cui *et al.* [315]
a-AGO	film-based MSM	1.38@230 nm	$\sim 10^6$		$\sim 2 \times 10^3$	Yuan *et al.* [321]
$(In_xGa_{1-x})_2O_3$	film-based MSM	3×10^{-2}–5×10^{-1}	–		$\sim 10^2$	Zhang *et al.* [326]
individual–NWs	NW-based MSM	–	$<9 \times 10^4$		–	Feng *et al.* [266]
NWs	NW-based MSM	–	$<2 \times 10^4$	$\sim 10^7$	$\sim 2 \times 10^3$	Li *et al.* [331]
NWs film	NW-based MSM	2.9×10^{-3}@258 nm	64		2×10^3	Chen *et al.* [203]
2D nanosheet	MSM	3.3@254 nm	$>10^6$		–	Feng *et al.* [258]
nanosheet	MSM	19.31@254 nm	2.3×10^4		–	Zhong *et al.* [259]
nanoflake	MSM	1.8×10^5@254 nm	$>10^6$		–	Oh *et al.* [169]
ZnO/β-Ga_2O_3	core–shell NW heterojunction APD	1.3×10^3@254 nm	42	815	2×10^3	Zhao *et al.* [240]
p-SiC/β-Ga_2O_3	heterojunction	0.053@260 nm	30	30	10^3	Nakagomi *et al.* [344]
p-GaN/β-Ga_2O_3	heterojunction	$\sim 1.8 \times 10^{-1}$@225 nm	300		$\sim 4 \times 10^2$	Nakagomi *et al.* [340]
SnO_2/β-Ga_2O_3	heterojunction APD	6.3×10^3@254 nm	48	100	7.4×10^3	Mahmoud [352]
ZnO/α-Ga_2O_3	heterojunction APD	1.1×10^4@254 nm	238	3040	10^3	Chen *et al.* [181]

Furthermore, despite the tenability of the sensitive spectral region expanding to the VUV region by ternary III-oxides, the photodetector performance is still deficient as compared to those III-nitride-based photodetectors, which strongly rely on the material quality and the development of epitaxial techniques. The solubility of alloying phase transitions must also be taken into account.

The second challenge is the reliability of APDs based on the reported isotype heterostructures. Unlike the well-known working mechanisms in APDs configured in the forms of p–n or p–i–n junctions, electrons are only majority carriers in the isotype n–N heterostructures, and the identification of the breakdown mechanism, the dynamics of carriers near the breakdown points, and the associated impact-ionization-induced multiplication are needed. Recent study indicates a normally off MOSFET based on an Ir_2O_3 p-type layer [365], and thus a design of a separate absorption and multiplication (SAM) APD can be expected, in which low dark current can be accomplished without sacrificing the quantum efficiency.

The third challenging factor lies in the reproducibility and reliability of photodetectors based on Ga_2O_3 nanostructures, although it shows the obvious figures of merit over bulk and thin films, including low energy consumption and high responsivity and especially flexibility. However, most nanostructures are synthesized in the equilibrium condition, in which the controllable doping and alloying as well as the fine quantum structures are difficult to yield. The presence of abundant surface states due to a large surface-to-volume ratio is also a critical issue to achieve high response speed, and even the transition time of the carrier in low-dimensional structures is low. Furthermore, the device performance strongly relies on the nanostructure synthesis conditions, which need more care to yield stable and reliable photodetectors. Especially for the flexible applications, the transferring techniques of nanostructures together with the suitable device fabrication processes require more efforts.

The last issue as well as the most challenging issue, we thought, is the realization of stable and reliable p-type Ga_2O_3, which is a general issue for most WBG semiconductors such as AlN, GaN, In_2O_3, and ZnO. It is critical not only for photodetectors but also for the development of other bipolar electronic and optoelectronic devices, such as high-power switches, transistors, and deep-UV light-emitting diodes, as well as APDs. Due to the lack of p-type, forming a p–n heterojunction with other p-type materials has become an alternative strategy to realize photovoltaic detectors. However, this compromising way suffers from several limitations, such as the defects and interfacial states inevitably induced by lattice mismatch, carrier blocking due to the band alignment, and long wavelength response due to the small bandgap of foreign substrates. With the lessons from p-type doping in ZnO, very few reports are focusing on p-type doping of Ga_2O_3. Theoretical calculations also indicate that group II elements, such as Mg and Zn in Ga_2O_3, are all deep-level acceptors, and more seriously, holes are always self-trapped in Ga_2O_3 materials, which need a very high temperature to be activated. One possible solution to achieve p-type conduction is nonequilibrium doping in other phased Ga_2O_3 at low temperature. The synthesis of high quality α- and ε-Ga_2O_3 by low temperature CVD techniques is a good demonstration. In particular, following the polarization engineering in III-nitrides and II-oxides, the reported spontaneous polarization in ε-Ga_2O_3 may help to reduce the ionization energy of acceptors and facilitate the p-type conduction. Together with these unique properties, such as ferroelectric polarization and an asymmetric optical bandgap, various solar blind photodetectors with novel functionality and improved performance may be expected.

Overall, the performance of Ga_2O_3-based solar-blind photodetectors in the current stage mainly relies on the material synthesis. Therefore, it is necessary to develop novel and reliable approaches to grow high-quality single-crystalline Ga_2O_3 materials with low defect density, tunable bandgap, controllable n- and p-type conductions, and desirable single phases. Engineering in the structural phase, band structure, and polarization, as well as defect engineering, is the strategic methodology to deliver high-performance Ga_2O_3 devices not limited to solar-blind photodetectors with commercial potential in practical applications.

Funding. National Key Research and Development Project (2017YFB0403003, 2018YFB0406502); National Natural Science Foundation of China (NSFC) (61322403, 61774081); State Key Laboratory of Wide-Bandgap Semiconductor Power Electric Devices (2017KF001); Natural Science Foundation of Jiangsu Province (BK20161401); State Key R&D Project of Jiangsu (BE2018115); Fundamental Research Funds for the Central Universities (021014380085, 021014380093); Postgraduate Research and Practice Innovation Program of Jiangsu Province.

REFERENCES

1. International Standard, Space Environment (Natural and Artificial)—Process for Determining Solar Irradiances, Technical report ISO 21348 (International Standard, 2007).
2. K. Osamura, K. Nakajima, Y. Murakami, P. H. Shingu, and A. Ohtsuki, "Fundamental absorption edge in GaN, InN and their alloys," Solid State Commun. **11**, 617–621 (1972).
3. J. D. Ye, S. L. Gu, S. M. Zhu, S. M. Liu, Y. D. Zheng, R. Zhang, Y. Shi, H. Q. Yu, and Y. D. Ye, "Gallium doping dependence of single-crystal n-type ZnO grown by metal organic chemical vapor deposition," J. Cryst. Growth **283**, 279–285 (2005).
4. C. Persson, C. Platzer-Bjorkman, J. Malmstrom, T. Torndahl, and M. Edoff, "Strong valence-band offset bowing of $ZnO_{1-x}S_x$ enhances p-type nitrogen doping of ZnO-like alloys," Phys. Rev. Lett. **97**, 146403 (2006).
5. F. Vigue, E. Tournie, and J. P. Faurie, "Evaluation of the potential of ZnSe and Zn(Mg)BeSe compounds for ultraviolet photodetection," IEEE J. Quantum Electron. **37**, 1146–1152 (2001).
6. H. Morkoç, S. Strite, G. B. Gao, M. E. Lin, B. Sverdlov, and M. Burns, "Large-band-gap SiC, III-V nitride, and II-VI ZnSe-based semiconductor device technologies," J. Appl. Phys. **76**, 1363–1398 (1994).
7. X. Chen, H. Zhu, J. Cai, and Z. Wu, "High-performance 4H-SiC-based ultraviolet p-i-n photodetector," J. Appl. Phys. **102**, 024505 (2007).
8. W. M. Yim, E. J. Stofko, P. J. Zanzucchi, J. I. Pankove, M. Ettenberg, and S. L. Gilbert, "Epitaxially grown AlN and its optical band gap," J. Appl. Phys. **44**, 292–296 (1973).
9. S. Salvatori, M. C. Rossi, F. Galluzzi, and E. Pace, "Solar-blind UV-photodetector based on polycrystalline diamond films: basic design principle and comparison with experimental results," Mater. Sci. Eng. B **46**, 105–111 (1997).
10. Y.-C. Chen, Y.-J. Lu, C.-N. Lin, Y.-Z. Tian, C.-J. Gao, L. Dong, and C.-X. Shan, "Self-powered diamond/β-Ga_2O_3 photodetectors for solar-blind imaging," J. Mater. Chem. C **6**, 5727–5732 (2018).
11. W. Zheng, R. Lin, Z. Zhang, and F. Huang, "Vacuum-ultraviolet photodetection in few-layered h-BN," ACS Appl. Mater. Interfaces **10**, 27116–27123 (2018).
12. T. Onuma, S. Saito, K. Sasaki, T. Masui, T. Yamaguchi, T. Honda, and M. Higashiwaki, "Valence band ordering in β-Ga_2O_3 studied by polarized transmittance and reflectance spectroscopy," Jpn. J. Appl. Phys. **54**, 112601 (2015).
13. K. Akaiwa and S. Fujita, "Electrical conductive corundum-structured α-Ga_2O_3 thin films on sapphire with tin-doping grown by spray-assisted mist chemical vapor deposition," Jpn. J. Appl. Phys. **51**, 070203 (2012).
14. S. Fujita, M. Oda, and K. Kaneko, and T. Hitora, "Evolution of corundum-structured III-oxide semiconductors: growth, properties, and devices," Jpn. J. Appl. Phys. **55**, 1202a3 (2016).
15. D. Li, K. Jiang, X. Sun, and C. Guo, "AlGaN photonics: recent advances in materials and ultraviolet devices," Adv. Opt. Photon. **10**, 43–110 (2018).
16. M. Kim, J.-H. Seo, U. Singisetti, and Z. Ma, "Recent advances in free-standing single crystalline wide band-gap semiconductors and their applications: GaN, SiC, ZnO, β-Ga_2O_3, and diamond," J. Mater. Chem. C **5**, 8338–8354 (2017).
17. J. Y. Tsao, S. Chowdhury, M. A. Hollis, D. Jena, N. M. Johnson, K. A. Jones, R. J. Kaplar, S. Rajan, C. G. Van de Walle, E. Bellotti, C. L. Chua, R. Collazo, M. E. Coltrin, J. A. Cooper, K. R. Evans, S. Graham, T. A. Grotjohn, E. R. Heller, M. Higashiwaki, M. S. Islam, P. W. Juodawlkis, M. A. Khan, A. D. Koehler, J. H. Leach, U. K. Mishra, R. J. Nemanich, R. C. N. Pilawa-Podgurski, J. B. Shealy, Z. Sitar, M. J. Tadjer, A. F. Witulski, M. Wraback, and J. A. Simmons, "Ultrawide-bandgap semiconductors: research opportunities and challenges," Adv. Electron. Mater. **4**, 1600501 (2018).
18. Z. G. Shao, D. J. Chen, H. Lu, R. Zhang, D. P. Cao, W. J. Luo, Y. D. Zheng, L. Li, and Z. H. Li, "High-gain AlGaN solar-blind avalanche photodiodes," IEEE Electron Device Lett. **35**, 372–374 (2014).
19. J. Yu, C. X. Shan, J. S. Liu, X. W. Zhang, B. H. Li, and D. Z. Shen, "MgZnO avalanche photodetectors realized in Schottky structures," Phys. Status Solidi RRL **7**, 425–428 (2013).
20. K. Balakrishnan, A. Bandoh, M. Iwaya, S. Kamiyama, H. Amano, and I. Akasaki, "Influence of high temperature in the growth of low dislocation content AlN bridge layers on patterned 6H-SiC substrates by metalorganic vapor phase epitaxy," Jpn. J. Appl. Phys. **46**, L307–L310 (2007).
21. M. Imura, K. Nakano, N. Fujimoto, N. Okada, K. Balakrishnan, M. Iwaya, S. Kamiyama, H. Amano, I. Akasaki, T. Noro, T. Takagi, and A. Bandoh, "High-temperature metal-organic vapor phase epitaxial growth of AlN on sapphire by multi transition growth mode method varying V/III ratio," Jpn. J. Appl. Phys. **45**, 8639–8643 (2006).
22. W. Yang, S. S. Hullavarad, B. Nagaraj, I. Takeuchi, R. P. Sharma, T. Venkatesan, R. D. Vispute, and H. Shen, "Compositionally-tuned epitaxial cubic Mg_xZn_{1-x} O on Si(100) for deep ultraviolet photodetectors," Appl. Phys. Lett. **82**, 3424–3426 (2003).
23. A. Balducci, M. Marinelli, E. Milani, M. E. Morgada, A. Tucciarone, G. Verona-Rinati, M. Angelone, and M. Pillon, "Extreme ultraviolet single-crystal diamond detectors by chemical vapor deposition," Appl. Phys. Lett. **86**, 193509 (2005).
24. A. Kuramata, K. Koshi, S. Watanabe, Y. Yamaoka, T. Masui, and S. Yamakoshi, "High-quality β-Ga_2O_3 single crystals grown by edge-defined film-fed growth," Jpn. J. Appl. Phys. **55**, 1202a2 (2016).
25. K. Sasaki, A. Kuramata, T. Masui, E. G. Víllora, K. Shimamura, and S. Yamakoshi, "Device-quality β-Ga_2O_3 epitaxial films fabricated by ozone molecular beam epitaxy," Appl. Phys. Express **5**, 035502 (2012).
26. A. Rose, *Concepts in Photoconductivity and Allied Problems* (Interscience, 1963).
27. E. Monroy, F. Omnès, and F. Calle, "Wide-bandgap semiconductor ultraviolet photodetectors," Semicond. Sci. Technol. **18**, R33–R51 (2003).
28. X. Gong, M. Tong, Y. Xia, W. Cai, J. S. Moon, Y. Cao, G. Yu, C. L. Shieh, B. Nilsson, and A. J. Heeger, "High-detectivity polymer photodetectors with spectral response from 300 nm to 1450 nm," Science **325**, 1665–1667 (2009).
29. R. J. Keyes, *Optical and Infrared Detectors, Topics in Applied Physics* (Springer-Verlag, 1977).
30. M. Razeghi and A. Rogalski, "Semiconductor ultraviolet detectors," J. Appl. Phys. **79**, 7433–7473 (1996).
31. P. Kung, X. Zhang, D. Walker, A. Saxler, J. Piotrowski, A. Rogalski, and M. Razeghi, "Kinetics of photoconductivity in n-type GaN photodetector," Appl. Phys. Lett. **67**, 3792–3794 (1995).
32. S. M. Sze and M.-K. Lee, *Semiconductor Devices: Physics and Technology*, 3rd ed. (Wiley, 2012).
33. M. Mohamed, K. Irmscher, C. Janowitz, Z. Galazka, R. Manzke, and R. Fornari, "Schottky barrier height of Au on the transparent semiconducting oxide β-Ga_2O_3," Appl. Phys. Lett. **101**, 132106 (2012).
34. S. Müller, H. von Wenckstern, F. Schmidt, D. Splith, F.-L. Schein, H. Frenzel, and M. Grundmann, "Comparison of Schottky contacts on β-gallium oxide thin films and bulk crystals," Appl. Phys. Express **8**, 121102 (2015).
35. R. Hackam and P. Harrop, "Electrical properties of nickel-low-doped n-type gallium arsenide Schottky-barrier diodes," IEEE Trans. Electron Devices **19**, 1231–1238 (1972).

36. W. Schottky and E. Spenke, "Quantitative treatment of the space charge and boundary-layer theory of the crystal rectifier," Wiss. Veroff. Siemens-Werken **18**, 225–291 (1939).
37. H. A. Bethe, *Theory of the Boundary Layer of Crystal Rectifiers* (Radiation Laboratory, Massachusetts Institute of Technology, 1942).
38. A. M. Cowley and S. M. Sze, "Surface states and barrier height of metal-semiconductor systems," J. Appl. Phys. **36**, 3212–3220 (1965).
39. C. R. Crowell and S. M. Sze, "Current transport in metal-semiconductor barriers," Solid-State Electron. **9**, 1035–1048 (1966).
40. C. Y. Wu, "Interfacial layer-thermionic-diffusion theory for the Schottky barrier diode," J. Appl. Phys. **53**, 5947–5950 (1982).
41. T. Hashizume, J. Kotani, and H. Hasegawa, "Leakage mechanism in GaN and AlGaN Schottky interfaces," Appl. Phys. Lett. **84**, 4884–4886 (2004).
42. E. J. Miller, E. T. Yu, P. Waltereit, and J. S. Speck, "Analysis of reverse-bias leakage current mechanisms in GaN grown by molecular-beam epitaxy," Appl. Phys. Lett. **84**, 535–537 (2004).
43. O. Katz, V. Garber, B. Meyler, G. Bahir, and J. Salzman, "Gain mechanism in GaN Schottky ultraviolet detectors," Appl. Phys. Lett. **79**, 1417–1419 (2001).
44. O. Katz, G. Bahir, and J. Salzman, "Persistent photocurrent and surface trapping in GaN Schottky ultraviolet detectors," Appl. Phys. Lett. **84**, 4092–4094 (2004).
45. T. Bruno, W. Haynes, and D. Lide, *CRC Handbook of Chemistry and Physics* (CRC Press, 2016).
46. S. N. Mohammad, "Contact mechanisms and design principles for alloyed ohmic contacts to n-GaN," J. Appl. Phys. **95**, 7940–7953 (2004).
47. A. J. Green, K. D. Chabak, M. Baldini, N. Moser, R. Gilbert, R. C. Fitch, G. Wagner, Z. Galazka, J. McCandless, A. Crespo, K. Leedy, and G. H. Jessen, "β-Ga$_2$O$_3$ MOSFETs for radio frequency operation," IEEE Electron Device Lett. **38**, 790–793 (2017).
48. K. Sasaki, M. Higashiwaki, A. Kuramata, T. Masui, and S. Yamakoshi, "Si-ion implantation doping in β-Ga$_2$O$_3$ and its application to fabrication of low-resistance ohmic contacts," Appl. Phys. Express **6**, 086502 (2013).
49. M. H. Wong, K. Sasaki, A. Kuramata, S. Yamakoshi, and M. Higashiwaki, "Field-plated Ga$_2$O$_3$ MOSFETs with a breakdown voltage of over 750 V," IEEE Electron Device Lett. **37**, 212–215 (2016).
50. Z. Hu, K. Nomoto, W. Li, N. Tanen, K. Sasaki, A. Kuramata, T. Nakamura, D. Jena, and H. G. Xing, "Enhancement-mode Ga$_2$O$_3$ vertical transistors with breakdown voltage >1 kV," IEEE Electron Device Lett. **39**, 869–872 (2018).
51. M. Higashiwaki, K. Sasaki, M. H. Wong, T. Kamimura, D. Krishnamurthy, A. Kuramata, T. Masui, and S. Yamakoshi, "Depletion-mode Ga$_2$O$_3$ MOSFETs on β-Ga$_2$O$_3$ (010) substrates with Si-ion-implanted channel and contacts," in *IEEE International Electron Devices Meeting* (2013).
52. M. H. Wong, Y. Nakata, A. Kuramata, S. Yamakoshi, and M. Higashiwaki, "Enhancement-mode Ga$_2$O$_3$ MOSFETs with Si-ion-implanted source and drain," Appl. Phys. Express **10**, 041101 (2017).
53. K. Zeng, J. S. Wallace, C. Heimburger, K. Sasaki, A. Kuramata, T. Masui, J. A. Gardella, and U. Singisetti, "Ga$_2$O$_3$ MOSFETs using spin-on-glass source/drain doping technology," IEEE Electron Device Lett. **38**, 513–516 (2017).
54. Y. Zhang, C. Joishi, Z. Xia, M. Brenner, S. Lodha, and S. Rajan, "Demonstration of β-(Al$_x$Ga$_{1-x}$)$_2$O$_3$/Ga$_2$O$_3$ double heterostructure field effect transistors," Appl. Phys. Lett. **112**, 233503 (2018).
55. S. Krishnamoorthy, Z. Xia, S. Bajaj, M. Brenner, and S. Rajan, "Delta-doped β-gallium oxide field-effect transistor," Appl. Phys. Express **10**, 051102 (2017).
56. K. Chabak, A. Green, N. Moser, S. Tetlak, J. McCandless, K. Leedy, R. Fitch, A. Crespo, and G. Jessen, "Gate-recessed, laterally-scaled β-Ga$_2$O$_3$ MOSFETs with high-voltage enhancement-mode operation," in *2017 75th Annual Device Research Conference (DRC)* (2017), pp. 1–2.
57. A. J. Green, K. D. Chabak, E. R. Heller, R. C. Fitch, M. Baldini, A. Fiedler, K. Irmscher, G. Wagner, Z. Galazka, S. E. Tetlak, A. Crespo, K. Leedy, and G. H. Jessen, "3.8-MV/cm breakdown strength of MOVPE-grown Sn-doped β-Ga$_2$O$_3$ MOSFETs," IEEE Electron Device Lett. **37**, 902–905 (2016).
58. N. A. Moser, J. P. McCandless, A. Crespo, K. D. Leedy, A. J. Green, E. R. Heller, K. D. Chabak, N. Peixoto, and G. H. Jessen, "High pulsed current density β-Ga$_2$O$_3$ MOSFETs verified by an analytical model corrected for interface charge," Appl. Phys. Lett. **110**, 143505 (2017).
59. P. H. Carey, J. Yang, F. Ren, D. C. Hays, S. J. Pearton, S. Jang, A. Kuramata, and I. I. Kravchenko, "Ohmic contacts on n-type β-Ga$_2$O$_3$ using AZO/Ti/Au," AIP Adv. **7**, 095313 (2017).
60. Y. Yao, R. F. Davis, and L. M. Porter, "Investigation of different metals as ohmic contacts to β-Ga$_2$O$_3$: comparison and analysis of electrical behavior, morphology, and other physical properties," J. Electron. Mater. **46**, 2053–2060 (2016).
61. P. H. Carey, J. Yang, F. Ren, D. C. Hays, S. J. Pearton, A. Kuramata, and I. I. Kravchenko, "Improvement of ohmic contacts on Ga$_2$O$_3$ through use of ITO-interlayers," J. Vac. Sci. Technol. B **35**, 061201 (2017).
62. T. Oshima, R. Wakabayashi, M. Hattori, A. Hashiguchi, N. Kawano, K. Sasaki, T. Masui, A. Kuramata, S. Yamakoshi, K. Yoshimatsu, A. Ohtomo, T. Oishi, and M. Kasu, "Formation of indium–tin oxide ohmic contacts for β-Ga$_2$O$_3$," Jpn. J. Appl. Phys. **55**, 1202b7 (2016).
63. H. Zhou, M. Si, S. Alghamdi, G. Qiu, L. Yang, and P. D. Ye, "High-performance depletion/enhancement-ode β-Ga$_2$O$_3$ on insulator (GOOI) field-effect transistors with record drain currents of 600/450 mA/mm," IEEE Electron Device Lett. **38**, 103–106 (2017).
64. H. Fu, H. Chen, X. Huang, I. Baranowski, J. Montes, T.-H. Yang, and Y. Zhao, "A comparative study on the electrical properties of vertical ($\bar{2}01$) and (010)β-Ga$_2$O$_3$ Schottky barrier diodes on EFG single-crystal substrates," IEEE Trans. Electron Devices **65**, 3507–3513 (2018).
65. T. C. Lovejoy, R. Chen, X. Zheng, E. G. Villora, K. Shimamura, H. Yoshikawa, Y. Yamashita, S. Ueda, K. Kobayashi, S. T. Dunham, F. S. Ohuchi, and M. A. Olmstead, "Band bending and surface defects in β-Ga$_2$O$_3$," Appl. Phys. Lett. **100**, 181602 (2012).
66. S. Jang, S. Jung, K. Beers, J. Yang, F. Ren, A. Kuramata, S. J. Pearton, and K. H. Baik, "A comparative study of wet etching and contacts on (201) and (010) oriented β-Ga$_2$O$_3$," J. Alloys Compd. **731**, 118–125 (2018).
67. R. Suzuki, S. Nakagomi, and Y. Kokubun, "Solar-blind photodiodes composed of a Au Schottky contact and a β-Ga$_2$O$_3$ single crystal with a high resistivity cap layer," Appl. Phys. Lett. **98**, 131114 (2011).
68. T. Oishi, Y. Koga, K. Harada, and M. Kasu, "High-mobility β-Ga$_2$O$_3$(201) single crystals grown by edge-defined film-fed growth method and their Schottky barrier diodes with Ni contact," Appl. Phys. Express **8**, 031101 (2015).
69. A. M. Armstrong, M. H. Crawford, A. Jayawardena, A. Ahyi, and S. Dhar, "Role of self-trapped holes in the photoconductive gain of β-gallium oxide Schottky diodes," J. Appl. Phys. **119**, 103102 (2016).
70. K. Sasaki, M. Higashiwaki, A. Kuramata, T. Masui, and S. Yamakoshi, "Ga$_2$O$_3$ Schottky barrier diodes fabricated by using single-crystal β–Ga$_2$O$_3$ (010) substrates," IEEE Electron Device Lett. **34**, 493–495 (2013).
71. E. Ahmadi, Y. Oshima, F. Wu, and J. S. Speck, "Schottky barrier height of Ni to β-(Al$_x$Ga$_{1-x}$)$_2$O$_3$ with different compositions grown by plasma-assisted molecular beam epitaxy," Semicond. Sci. Technol. **32**, 035004 (2017).
72. Y. Yao, R. Gangireddy, J. Kim, K. K. Das, R. F. Davis, and L. M. Porter, "Electrical behavior of β-Ga$_2$O$_3$ Schottky diodes with different Schottky metals," J. Vac. Sci. Technol. B **35**, 03d113 (2017).
73. M. J. Tadjer, V. D. Wheeler, D. I. Shahin, C. R. Eddy, and F. J. Kub, "Thermionic emission analysis of TiN and Pt Schottky contacts to β-Ga$_2$O$_3$," ECS J. Solid State Sci. Technol. **6**, P165–P168 (2017).
74. M. Kasu, K. Hanada, T. Moribayashi, A. Hashiguchi, T. Oshima, T. Oishi, K. Koshi, K. Sasaki, A. Kuramata, and O. Ueda, "Relationship between crystal defects and leakage current in β-Ga$_2$O$_3$ Schottky barrier diodes," Jpn. J. Appl. Phys. **55**, 1202bb (2016).
75. S. Oh, G. Yang, and J. Kim, "Electrical characteristics of vertical Ni/β-Ga$_2$O$_3$ Schottky barrier diodes at high temperatures," ECS J. Solid State Sci. Technol. **6**, Q3022–Q3025 (2016).
76. S. Ahn, F. Ren, L. Yuan, S. J. Pearton, and A. Kuramata, "Temperature-dependent characteristics of Ni/Au and Pt/Au

Schottky diodes on β-Ga$_2$O$_3$," ECS J. Solid State Sci. Technol. **6**, P68–P72 (2017).

77. E. Farzana, Z. Zhang, P. K. Paul, A. R. Arehart, and S. A. Ringel, "Influence of metal choice on (010) β-Ga$_2$O$_3$ Schottky diode properties," Appl. Phys. Lett. **110**, 202102 (2017).
78. M. Kasu, T. Oshima, K. Hanada, T. Moribayashi, A. Hashiguchi, T. Oishi, K. Koshi, K. Sasaki, A. Kuramata, and O. Ueda, "Crystal defects observed by the etch-pit method and their effects on Schottky-barrier-diode characteristics on (201) β-Ga$_2$O$_3$," Jpn. J. Appl. Phys. **56**, 091101 (2017).
79. J. Yang, S. Ahn, F. Ren, R. Khanna, K. Bevlin, D. Geerpuram, S. J. Pearton, and A. Kuramata, "Inductively coupled plasma etch damage in (-201) Ga$_2$O$_3$ Schottky diodes," Appl. Phys. Lett. **110**, 142101 (2017).
80. T. Oshima, A. Hashiguchi, T. Moribayashi, K. Koshi, K. Sasaki, A. Kuramata, O. Ueda, T. Oishi, and M. Kasu, "Electrical properties of Schottky barrier diodes fabricated on (001) β-Ga$_2$O$_3$ substrates with crystal defects," Jpn. J. Appl. Phys. **56**, 086501 (2017).
81. Q. Feng, Z. Feng, Z. Hu, X. Xing, G. Yan, J. Zhang, Y. Xu, X. Lian, and Y. Hao, "Temperature dependent electrical properties of pulse laser deposited Au/Ni/β-(AlGa)$_2$O$_3$ Schottky diode," Appl. Phys. Lett. **112**, 072103 (2018).
82. M. Higashiwaki, K. Konishi, K. Sasaki, K. Goto, K. Nomura, Q. T. Thieu, R. Togashi, H. Murakami, Y. Kumagai, B. Monemar, A. Koukitu, A. Kuramata, and S. Yamakoshi, "Temperature-dependent capacitance-voltage and current-voltage characteristics of Pt/Ga$_2$O$_3$ (001) Schottky barrier diodes fabricated on n$^-$-Ga$_2$O$_3$ drift layers grown by halide vapor phase epitaxy," Appl. Phys. Lett. **108**, 133503 (2016).
83. Q. He, W. Mu, H. Dong, S. Long, Z. Jia, H. Lv, Q. Liu, M. Tang, X. Tao, and M. Liu, "Schottky barrier diode based on β-Ga$_2$O$_3$ (100) single crystal substrate and its temperature-dependent electrical characteristics," Appl. Phys. Lett. **110**, 093503 (2017).
84. K. Konishi, K. Goto, H. Murakami, Y. Kumagai, A. Kuramata, S. Yamakoshi, and M. Higashiwaki, "1-kV vertical Ga$_2$O$_3$ field-plated Schottky barrier diodes," Appl. Phys. Lett. **110**, 103506 (2017).
85. R. Suzuki, S. Nakagomi, Y. Kokubun, N. Arai, and S. Ohira, "Enhancement of responsivity in solar-blind β-Ga$_2$O$_3$ photodiodes with a Au Schottky contact fabricated on single crystal substrates by annealing," Appl. Phys. Lett. **94**, 222102 (2009).
86. D. Splith, S. Müller, F. Schmidt, H. von Wenckstern, J. J. van Rensburg, W. E. Meyer, and M. Grundmann, "Determination of the mean and the homogeneous barrier height of Cu Schottky contacts on heteroepitaxial β-Ga$_2$O$_3$ thin films grown by pulsed laser deposition," Phys. Status Solidi A **211**, 40–47 (2014).
87. K. Sasaki, D. Wakimoto, Q. T. Thieu, Y. Koishikawa, A. Kuramata, M. Higashiwaki, and S. Yamakoshi, "First demonstration of Ga$_2$O$_3$ trench MOS-type Schottky barrier diodes," IEEE Electron Device Lett. **38**, 783–785 (2017).
88. H. H. Tippins, "Optical absorption and photoconductivity in the band edge of β-Ga$_2$O$_3$," Phys. Rev. **140**, A316–A319 (1965).
89. N. Ueda, H. Hosono, R. Waseda, and H. Kawazoe, "Anisotropy of electrical and optical properties in β-Ga$_2$O$_3$ single crystals," Appl. Phys. Lett. **71**, 933–935 (1997).
90. M. Orita, H. Ohta, M. Hirano, and H. Hosono, "Deep-ultraviolet transparent conductive β-Ga$_2$O$_3$ thin films," Appl. Phys. Lett. **77**, 4166–4168 (2000).
91. D. Shinohara and S. Fujita, "Heteroepitaxy of corundum-structured α-Ga$_2$O$_3$ thin films on α-Al$_2$O$_3$ substrates by ultrasonic mist chemical vapor deposition," Jpn. J. Appl. Phys. **47**, 7311–7313 (2008).
92. K. A. Mengle, G. Shi, D. Bayerl, and E. Kioupakis, "First-principles calculations of the near-edge optical properties of β-Ga$_2$O$_3$," Appl. Phys. Lett. **109**, 212104 (2016).
93. R. Roy, V. G. Hill, and E. F. Osborn, "Polymorphism of Ga$_2$O$_3$ and the system Ga$_2$O$_3$-H$_2$O," J. Am. Chem. Soc. **74**, 719–722 (1952).
94. S. Geller, "Crystal structure of β-Ga$_2$O$_3$," J. Chem. Phys. **33**, 676–684 (1960).
95. H. He, R. Orlando, M. A. Blanco, R. Pandey, E. Amzallag, I. Baraille, and M. Rérat, "First-principles study of the structural, electronic, and optical properties of Ga$_2$O$_3$ in its monoclinic and hexagonal phases," Phys. Rev. B **74**, 195123 (2006).
96. H. Y. Playford, A. C. Hannon, E. R. Barney, and R. I. Walton, "Structures of uncharacterised polymorphs of gallium oxide from total neutron diffraction," Chemistry **19**, 2803–2813 (2013).
97. M. Marezio and J. P. Remeika, "Bond lengths in the α-Ga$_2$O$_3$ structure and the high-pressure phase of Ga$_{2-x}$Fe$_x$O$_3$," J. Chem. Phys. **46**, 1862–1865 (1967).
98. S. Yoshioka, H. Hayashi, A. Kuwabara, F. Oba, K. Matsunaga, and I. Tanaka, "Structures and energetics of Ga$_2$O$_3$ polymorphs," J. Phys. Condens. Matter **19**, 346211 (2007).
99. R. Jinno, T. Uchida, K. Kaneko, and S. Fujita, "Control of crystal structure of Ga$_2$O$_3$ on sapphire substrate by introduction of α-(Al$_x$Ga$_{1-x}$)$_2$O$_3$ buffer layer," Phys. Status Solidi B **255**, 1700326 (2018).
100. Y. Zhang, A. Neal, Z. Xia, C. Joishi, J. M. Johnson, Y. Zheng, S. Bajaj, M. Brenner, D. Dorsey, K. Chabak, G. Jessen, J. Hwang, S. Mou, J. P. Heremans, and S. Rajan, "Demonstration of high mobility and quantum transport in modulation-doped β-(Al$_x$Ga$_{1-x}$)$_2$O$_3$/Ga$_2$O$_3$ heterostructures," Appl. Phys. Lett. **112**, 173502 (2018).
101. C. O. Areán, A. L. Bellan, M. P. Mentruit, M. R. G. Delgado, and G. T. Palomino, "Preparation and characterization of mesoporous γ-Ga$_2$O$_3$," Microporous Mesoporous Mater. **40**, 35–42 (2000).
102. T. Oshima, T. Nakazono, A. Mukai, and A. Ohtomo, "Epitaxial growth of γ-Ga$_2$O$_3$ films by mist chemical vapor deposition," J. Cryst. Growth **359**, 60–63 (2012).
103. H. Y. Playford, A. C. Hannon, M. G. Tucker, D. M. Dawson, S. E. Ashbrook, R. J. Kastiban, J. Sloan, and R. I. Walton, "Characterization of structural disorder in γ-Ga$_2$O$_3$," J. Phys. Chem. C **118**, 16188–16198 (2014).
104. F. Mezzadri, G. Calestani, F. Boschi, D. Delmonte, M. Bosi, and R. Fornari, "Crystal structure and ferroelectric properties of ε-Ga$_2$O$_3$ films grown on (0001)-sapphire," Inorg. Chem. **55**, 12079–12084 (2016).
105. D. Tahara, H. Nishinaka, M. Noda, and M. Yoshimoto, "Use of mist chemical vapor deposition to impart ferroelectric properties to ε-Ga$_2$O$_3$ thin films on SnO$_2$/c-sapphire substrates," Mater. Lett. **232**, 47–50 (2018).
106. Y. Oshima, E. G. Víllora, Y. Matsushita, S. Yamamoto, and K. Shimamura, "Epitaxial growth of phase-pure ε-Ga$_2$O$_3$ by halide vapor phase epitaxy," J. Appl. Phys. **118**, 085301 (2015).
107. M. Kracht, A. Karg, J. Schörmann, M. Weinhold, D. Zink, F. Michel, M. Rohnke, M. Schowalter, B. Gerken, A. Rosenauer, P. J. Klar, J. Janek, and M. Eickhoff, "Tin-assisted synthesis of ε–Ga$_2$O$_3$ by molecular beam epitaxy," Phys. Rev. Appl. **8**, 054002 (2017).
108. I. Cora, F. Mezzadri, F. Boschi, M. Bosi, M. Čaplovičová, G. Calestani, I. Dódony, B. Pecz, and R. Fornari, "The real structure of ε-Ga$_2$O$_3$ and its relation to κ-phase," CrystEngComm **19**, 1509–1516 (2017).
109. S. B. Cho and R. Mishra, "Epitaxial engineering of polar ε-Ga$_2$O$_3$ for tunable two-dimensional electron gas at the heterointerface," Appl. Phys. Lett. **112**, 162101 (2018).
110. H. Nishinaka, D. Tahara, and M. Yoshimoto, "Heteroepitaxial growth of ε-Ga$_2$O$_3$ thin films on cubic (111) MgO and (111) yttria-stablized zirconia substrates by mist chemical vapor deposition," Jpn. J. Appl. Phys. **55**, 1202bc (2016).
111. F. Boschi, M. Bosi, T. Berzina, E. Buffagni, C. Ferrari, and R. Fornari, "Hetero-epitaxy of ε-Ga$_2$O$_3$ layers by MOCVD and ALD," J. Cryst. Growth **443**, 25–30 (2016).
112. X. Xia, Y. Chen, Q. Feng, H. Liang, P. Tao, M. Xu, and G. Du, "Hexagonal phase-pure wide band gap ε-Ga$_2$O$_3$ films grown on 6H-SiC substrates by metal organic chemical vapor deposition," Appl. Phys. Lett. **108**, 202103 (2016).
113. S.-D. Lee, K. Akaiwa, and S. Fujita, "Thermal stability of single crystalline alpha gallium oxide films on sapphire substrates," Phys. Status Solidi C **10**, 1592–1595 (2013).
114. Y. Tomm, P. Reiche, D. Klimm, and T. Fukuda, "Czochralski grown Ga$_2$O$_3$ crystals," J. Cryst. Growth **220**, 510–514 (2000).
115. A. O. Chase, "Growth of β-Ga$_2$O$_3$ by the Verneuil technique," J. Am. Ceram. Soc. **47**, 470 (1964).
116. M. Fleischer and H. Meixner, "Electron mobility in single- and polycrystalline Ga$_2$O$_3$," J. Appl. Phys. **74**, 300–305 (1993).

117. K. Hoshikawa, E. Ohba, T. Kobayashi, J. Yanagisawa, C. Miyagawa, and Y. Nakamura, “Growth of β-Ga_2O_3 single crystals using vertical Bridgman method in ambient air,” J. Cryst. Growth **447**, 36–41 (2016).
118. E. Ohba, T. Kobayashi, M. Kado, and K. Hoshikawa, “Defect characterization of β-Ga_2O_3 single crystals grown by vertical Bridgman method,” Jpn. J. Appl. Phys. **55**, 1202bf (2016).
119. M. Saurat and A. Revcolevschi, “Preparation by floating zone method, of refractory oxide monocrystals, in particular of gallium oxide, and study of some of their properties,” Rev. Int. Hautes Temp. Refract. **8**, 291 (1971).
120. N. Ueda, H. Hosono, R. Waseda, and H. Kawazoe, “Synthesis and control of conductivity of ultraviolet transmitting β-Ga_2O_3 single crystals,” Appl. Phys. Lett. **70**, 3561–3563 (1997).
121. Y. Tomm, J. M. Ko, A. Yoshikawa, and T. Fukuda, “Floating zone growth of β-Ga_2O_3: a new window material for optoelectronic device applications,” Sol. Energy Mater. Sol. Cells **66**, 369–374 (2001).
122. E. G. Víllora, M. Yamaga, T. Inoue, S. Yabasi, Y. Masui, T. Sugawara, and T. Fukuda, “Optical spectroscopy study on β-Ga_2O_3,” Jpn. J. Appl. Phys. **41**, L622–L625 (2002).
123. E. G. Víllora, Y. Morioka, T. Atou, T. Sugawara, M. Kikuchi, and T. Fukuda, “Infrared reflectance and electrical conductivity of β-Ga_2O_3,” Phys. Status Solidi A **193**, 187–195 (2002).
124. E. G. Víllora, K. Hatanaka, H. Odaka, T. Sugawara, T. Miura, H. Fukumura, and T. Fukuda, “Luminescence of undoped β-Ga_2O_3 single crystals excited by picosecond x-ray and sub-picosecond UV pulses,” Solid State Commun. **127**, 385–388 (2003).
125. E. G. Víllora, K. Shimamura, Y. Yoshikawa, K. Aoki, and N. Ichinose, “Large-size β-Ga_2O_3 single crystals and wafers,” J. Cryst. Growth **270**, 420–426 (2004).
126. J. Zhang, B. Li, C. Xia, G. Pei, Q. Deng, Z. Yang, W. Xu, H. Shi, F. Wu, Y. Wu, and J. Xu, “Growth and spectral characterization of β-Ga_2O_3 single crystals,” J. Phys. Chem. Solids **67**, 2448–2451 (2006).
127. J. Zhang, C. Xia, Q. Deng, W. Xu, H. Shi, F. Wu, and J. Xu, “Growth and characterization of new transparent conductive oxides single crystals β-Ga_2O_3: Sn,” J. Phys. Chem. Solids **67**, 1656–1659 (2006).
128. N. Suzuki, S. Ohira, M. Tanaka, T. Sugawara, K. Nakajima, and T. Shishido, “Fabrication and characterization of transparent conductive Sn-doped β-Ga_2O_3 single crystal,” Phys. Status Solidi C **4**, 2310–2313 (2007).
129. S. Ohira, N. Suzuki, N. Arai, M. Tanaka, T. Sugawara, K. Nakajima, and T. Shishido, “Characterization of transparent and conducting Sn-doped β-Ga_2O_3 single crystal after annealing,” Thin Solid Films **516**, 5763–5767 (2008).
130. E. G. Víllora, K. Shimamura, Y. Yoshikawa, T. Ujiie, and K. Aoki, “Electrical conductivity and carrier concentration control in β-Ga_2O_3 by Si doping,” Appl. Phys. Lett. **92**, 202120 (2008).
131. Z. Galazka, R. Uecker, K. Irmscher, M. Albrecht, D. Klimm, M. Pietsch, M. Brützam, R. Bertram, S. Ganschow, and R. Fornari, “Czochralski growth and characterization of β-Ga_2O_3 single crystals,” Cryst. Res. Technol. **45**, 1229–1236 (2010).
132. Z. Galazka, R. Uecker, D. Klimm, K. Irmscher, M. Naumann, M. Pietsch, A. Kwasniewski, R. Bertram, S. Ganschow, and M. Bickermann, “Scaling-up of bulk β-Ga_2O_3 single crystals by the Czochralski method,” ECS J. Solid State Sci. Technol. **6**, Q3007–Q3011 (2017).
133. Z. Galazka, K. Irmscher, R. Uecker, R. Bertram, M. Pietsch, A. Kwasniewski, M. Naumann, T. Schulz, R. Schewski, D. Klimm, and M. Bickermann, “On the bulk β-Ga_2O_3 single crystals grown by the Czochralski method,” J. Cryst. Growth **404**, 184–191 (2014).
134. H. Aida, K. Nishiguchi, H. Takeda, N. Aota, K. Sunakawa, and Y. Yaguchi, “Growth of β-Ga_2O_3 single crystals by the edge-defined, film fed growth method,” Jpn. J. Appl. Phys. **47**, 8506–8509 (2008).
135. W. Mu, Z. Jia, Y. Yin, Q. Hu, Y. Li, B. Wu, J. Zhang, and X. Tao, “High quality crystal growth and anisotropic physical characterization of β-Ga_2O_3 single crystals grown by EFG method,” J. Alloys Compd. **714**, 453–458 (2017).
136. W. Mu, Z. Jia, Y. Yin, Q. Hu, J. Zhang, Q. Feng, Y. Hao, and X. Tao, “One-step exfoliation of ultra-smooth β-Ga_2O_3 wafers from bulk crystal for photodetectors,” CrystEngComm **19**, 5122–5127 (2017).
137. G. Katz and R. Roy, “Flux growth and characterization of β-Ga_2O_3 single crystals,” J. Am. Ceram. Soc. **49**, 168–169 (1966).
138. G. Garton, S. H. Smith, and B. M. Wanklyn, “Crystal growth from the flux systems PbO-V_2O_5 and Bi_2O_3-V_2O_5,” J. Cryst. Growth **13-14**, 588–592 (1972).
139. V. I. Chani, K. Inoue, K. Shimamura, K. Sugiyama, and T. Fukuda, “Segregation coefficients in β-Ga_2O_3: Cr crystals grown from a B_2O_3 based flux,” J. Cryst. Growth **132**, 335–336 (1993).
140. T. Matsumoto, M. Aoki, A. Kinoshita, and T. Aono, “Absorption and reflection of vapor grown single crystal platelets of β-Ga_2O_3,” Jpn. J. Appl. Phys. **13**, 1578–1582 (1974).
141. H. Juskowiak and A. Pajaczkowska, “Chemical transport of β-Ga_2O_3 using chlorine as a transporting agent,” J. Mater. Sci. **21**, 3430–3434 (1986).
142. A. Pajączkowska and H. Juskowiak, “On the chemical transport of gallium oxide in the Ga_2O_3/N-H-Cl system,” J. Cryst. Growth **79**, 421–426 (1986).
143. K. Irmscher, Z. Galazka, M. Pietsch, R. Uecker, and R. Fornari, “Electrical properties of β-Ga_2O_3 single crystals grown by the Czochralski method,” J. Appl. Phys. **110**, 063720 (2011).
144. S. C. Siah, R. E. Brandt, K. Lim, L. T. Schelhas, R. Jaramillo, M. D. Heinemann, D. Chua, J. Wright, J. D. Perkins, C. U. Segre, R. G. Gordon, M. F. Toney, and T. Buonassisi, “Dopant activation in Sn-doped Ga_2O_3 investigated by x-ray absorption spectroscopy,” Appl. Phys. Lett. **107**, 252103 (2015).
145. M. Baldini, M. Albrecht, A. Fiedler, K. Irmscher, R. Schewski, and G. Wagner, “Si- and Sn-doped homoepitaxial β-Ga_2O_3 layers grown by MOVPE on (010)-oriented substrates,” ECS J. Solid State Sci. Technol. **6**, Q3040–Q3044 (2016).
146. S.-D. Lee, K. Kaneko, and S. Fujita, “Homoepitaxial growth of beta gallium oxide films by mist chemical vapor deposition,” Jpn. J. Appl. Phys. **55**, 1202B8 (2016).
147. E. Ahmadi, O. S. Koksaldi, S. W. Kaun, Y. Oshima, D. B. Short, U. K. Mishra, and J. S. Speck, “Ge doping of β-Ga_2O_3 films grown by plasma-assisted molecular beam epitaxy,” Appl. Phys. Express **10**, 041102 (2017).
148. K. D. Leedy, K. D. Chabak, V. Vasilyev, D. C. Look, J. J. Boeckl, J. L. Brown, S. E. Tetlak, A. J. Green, N. A. Moser, A. Crespo, D. B. Thomson, R. C. Fitch, J. P. McCandless, and G. H. Jessen, “Highly conductive homoepitaxial Si-doped Ga_2O_3 films on (010) β-Ga_2O_3 by pulsed laser deposition,” Appl. Phys. Lett. **111**, 012103 (2017).
149. K. Goto, K. Konishi, H. Murakami, Y. Kumagai, B. Monemar, M. Higashiwaki, A. Kuramata, and S. Yamakoshi, “Halide vapor phase epitaxy of Si doped β-Ga_2O_3 and its electrical properties,” Thin Solid Films **666**, 182–184 (2018).
150. S.-H. Han, A. Mauze, E. Ahmadi, T. Mates, Y. Oshima, and J. S. Speck, “n-type dopants in (001) β-Ga_2O_3 grown on (001) β-Ga_2O_3 substrates by plasma-assisted molecular beam epitaxy,” Semicond. Sci. Technol. **33**, 045001 (2018).
151. J. B. Varley, A. Janotti, C. Franchini, and C. G. Van de Walle, “Role of self-trapping in luminescence and p-type conductivity of wide-band-gap oxides,” Phys. Rev. B **85**, 081109 (2012).
152. P. Deák, Q. Duy Ho, F. Seemann, B. Aradi, M. Lorke, and T. Frauenheim, “Choosing the correct hybrid for defect calculations: a case study on intrinsic carrier trapping in β–Ga_2O_3,” Phys. Rev. B **95**, 075208 (2017).
153. A. Kyrtsos, M. Matsubara, and E. Bellotti, “On the feasibility of p-type Ga_2O_3,” Appl. Phys. Lett. **112**, 032108 (2018).
154. A. T. Neal, S. Mou, S. Rafique, H. Zhao, E. Ahmadi, J. S. Speck, K. T. Stevens, J. D. Blevins, D. B. Thomson, N. Moser, K. D. Chabak, and G. H. Jessen, “Donors and deep acceptors in β-Ga_2O_3,” Appl. Phys. Lett. **113**, 062101 (2018).
155. T. Onuma, S. Fujioka, T. Yamaguchi, M. Higashiwaki, K. Sasaki, T. Masui, and T. Honda, “Correlation between blue luminescence intensity and resistivity in β-Ga_2O_3 single crystals,” Appl. Phys. Lett. **103**, 041910 (2013).
156. M. H. Wong, K. Sasaki, A. Kuramata, S. Yamakoshi, and M. Higashiwaki, “Anomalous Fe diffusion in Si-ion-implanted β-Ga_2O_3 and its suppression in Ga_2O_3 transistor structures through highly resistive buffer layers,” Appl. Phys. Lett. **106**, 032105 (2015).

157. C. Tang, J. Sun, N. Lin, Z. Jia, W. Mu, X. Tao, and X. Zhao, "Electronic structure and optical property of metal-doped Ga_2O_3: a first principles study," RSC Adv. **6**, 78322–78334 (2016).
158. M. Higashiwaki, K. Sasaki, A. Kuramata, T. Masui, and S. Yamakoshi, "Gallium oxide (Ga_2O_3) metal-semiconductor field-effect transistors on single-crystal β-Ga_2O_3 (010) substrates," Appl. Phys. Lett. **100**, 013504 (2012).
159. N. Ma, N. Tanen, A. Verma, Z. Guo, T. Luo, H. Xing, and D. Jena, "Intrinsic electron mobility limits in β-Ga_2O_3," Appl. Phys. Lett. **109**, 212101 (2016).
160. T. Oshima, N. Arai, N. Suzuki, S. Ohira, and S. Fujita, "Surface morphology of homoepitaxial β-Ga_2O_3 thin films grown by molecular beam epitaxy," Thin Solid Films **516**, 5768–5771 (2008).
161. W. S. Hwang, A. Verma, H. Peelaers, V. Protasenko, S. Rouvimov, H. Xing, A. Seabaugh, W. Haensch, C. V. de Walle, Z. Galazka, M. Albrecht, R. Fornari, and D. Jena, "High-voltage field effect transistors with wide-bandgap β-Ga_2O_3 nanomembranes," Appl. Phys. Lett. **104**, 203111 (2014).
162. S. Ahn, F. Ren, J. Kim, S. Oh, J. Kim, M. A. Mastro, and S. J. Pearton, "Effect of front and back gates on β-Ga_2O_3 nano-belt field-effect transistors," Appl. Phys. Lett. **109**, 062102 (2016).
163. J. Kim, M. A. Mastro, M. J. Tadjer, and J. Kim, "Quasi-two-dimensional h-BN/β-Ga_2O_3 heterostructure metal–insulator–semiconductor field-effect transistor," ACS Appl. Mater. Interfaces **9**, 21322–21327 (2017).
164. M. Si, L. Yang, H. Zhou, and P. D. Ye, "β-Ga_2O_3 nanomembrane negative capacitance field-effect transistors with steep subthreshold slope for wide band gap logic applications," ACS Omega **2**, 7136–7140 (2017).
165. H. Zhou, K. Maize, G. Qiu, A. Shakouri, and P. D. Ye, "β-Ga_2O_3 on insulator field-effect transistors with drain currents exceeding 1.5 A/mm and their self-heating effect," Appl. Phys. Lett. **111**, 092102 (2017).
166. J. Kim, M. A. Mastro, M. J. Tadjer, and J. Kim, "Heterostructure WSe_2–Ga_2O_3 junction field-effect transistor for low-dimensional high-power electronics," ACS Appl. Mater. Interfaces **10**, 29724–29729 (2018).
167. Y. Kwon, G. Lee, S. Oh, J. Kim, S. J. Pearton, and F. Ren, "Tuning the thickness of exfoliated quasi-two-dimensional β-Ga_2O_3 flakes by plasma etching," Appl. Phys. Lett. **110**, 131901 (2017).
168. S. Oh, C.-K. Kim, and J. Kim, "High responsivity β-Ga_2O_3 metal–semiconductor–metal solar-blind photodetectors with ultraviolet transparent graphene electrodes," ACS Photon. **5**, 1123–1128 (2017).
169. S. Oh, J. Kim, F. Ren, S. J. Pearton, and J. Kim, "Quasi-two-dimensional β-gallium oxide solar-blind photodetectors with ultrahigh responsivity," J. Mater. Chem. C **4**, 9245–9250 (2016).
170. S. Oh, M. A. Mastro, M. J. Tadjer, and J. Kim, "Solar-blind metal-semiconductor-metal photodetectors based on an exfoliated β-Ga_2O_3 micro-flake," ECS J. Solid State Sci. Technol. **6**, Q79–Q83 (2017).
171. E. G. Víllora, K. Shimamura, K. Kitamura, and K. Aoki, "Rf-plasma-assisted molecular-beam epitaxy of β-Ga_2O_3," Appl. Phys. Lett. **88**, 031105 (2006).
172. K. Sasaki, M. Higashiwaki, A. Kuramata, T. Masui, and S. Yamakoshi, "Growth temperature dependences of structural and electrical properties of Ga_2O_3 epitaxial films grown on β-Ga_2O_3 (010) substrates by molecular beam epitaxy," J. Cryst. Growth **392**, 30–33 (2014).
173. D. Gogova, M. Schmidbauer, and A. Kwasniewski, "Homo- and heteroepitaxial growth of Sn-doped β-Ga_2O_3 layers by MOVPE," CrystEngComm **17**, 6744–6752 (2015).
174. K. Nomura, K. Goto, R. Togashi, H. Murakami, Y. Kumagai, A. Kuramata, S. Yamakoshi, and A. Koukitu, "Thermodynamic study of β-Ga_2O_3 growth by halide vapor phase epitaxy," J. Cryst. Growth **405**, 19–22 (2014).
175. H. Murakami, K. Nomura, K. Goto, K. Sasaki, K. Kawara, Q. T. Thieu, R. Togashi, Y. Kumagai, M. Higashiwaki, A. Kuramata, S. Yamakoshi, B. Monemar, and A. Koukitu, "Homoepitaxial growth of β-Ga_2O_3 layers by halide vapor phase epitaxy," Appl. Phys. Express **8**, 015503 (2015).
176. S. Rafique, L. Han, A. T. Neal, S. Mou, M. J. Tadjer, R. H. French, and H. Zhao, "Heteroepitaxy of N-type β-Ga_2O_3 thin films on sapphire substrate by low pressure chemical vapor deposition," Appl. Phys. Lett. **109**, 132103 (2016).
177. S. Rafique, L. Han, M. J. Tadjer, J. A. Freitas, N. A. Mahadik, and H. Zhao, "Homoepitaxial growth of β-Ga_2O_3 thin films by low pressure chemical vapor deposition," Appl. Phys. Lett. **108**, 182105 (2016).
178. T. Oshima, Y. Kato, N. Kawano, A. Kuramata, S. Yamakoshi, S. Fujita, T. Oishi, and M. Kasu, "Carrier confinement observed at modulation-doped β-$(Al_xGa_{1-x})_2O_3/Ga_2O_3$ heterojunction interface," Appl. Phys. Express **10**, 035701 (2017).
179. S. Krishnamoorthy, Z. Xia, C. Joishi, Y. Zhang, J. McGlone, J. Johnson, M. Brenner, A. R. Arehart, J. Hwang, S. Lodha, and S. Rajan, "Modulation-doped β-$(Al_{0.2}Ga_{0.8})_2O_3/Ga_2O_3$ field-effect transistor," Appl. Phys. Lett. **111**, 023502 (2017).
180. R. Schewski, G. Wagner, M. Baldini, D. Gogova, Z. Galazka, T. Schulz, T. Remmele, T. Markurt, H. von Wenckstern, M. Grundmann, O. Bierwagen, P. Vogt, and M. Albrecht, "Epitaxial stabilization of pseudomorphic α-Ga_2O_3 on sapphire (0001)," Appl. Phys. Express **8**, 011101 (2015).
181. X. Chen, Y. Xu, D. Zhou, S. Yang, F. F. Ren, H. Lu, K. Tang, S. Gu, R. Zhang, Y. Zheng, and J. Ye, "Solar-blind photodetector with high avalanche gains and bias-tunable detecting functionality based on metastable phase α-Ga_2O_3/ZnO isotype heterostructures," ACS Appl. Mater. Interfaces **9**, 36997–37005 (2017).
182. M. Oda, K. Kaneko, S. Fujita, and T. Hitora, "Crack-free thick (~5 μm) α-Ga_2O_3 films on sapphire substrates with α-$(Al, Ga)_2O_3$ buffer layers," Jpn. J. Appl. Phys. **55**, 070304 (2016).
183. K. Kaneko, S. Fujita, and T. Hitora, "A power device material of corundum-structured α-Ga_2O_3 fabricated by MIST EPITAXY® technique," Jpn. J. Appl. Phys. **57**, 02cb18 (2018).
184. S. Fujita, "Evolution of oxide semiconductors for novel functional device applications," in *IEEE 16th International Conference on Nanotechnology* (IEEE-Nano) (2016), pp. 714–717.
185. T. Uchida, K. Kaneko, and S. Fujita, "Electrical characterization of Si-doped n-type α-Ga_2O_3 on sapphire substrates," MRS Adv. **3**, 171–177 (2018).
186. M. Oda, R. Tokuda, H. Kambara, T. Tanikawa, T. Sasaki, and T. Hitora, "Schottky barrier diodes of corundum-structured gallium oxide showing on-resistance of 0.1 $m\Omega \cdot cm^2$ grown by MIST EPITAXY®," Appl. Phys. Express **9**, 021101 (2016).
187. G. T. Dang, T. Kawaharamura, M. Furuta, and M. W. Allen, "Mist-CVD grown Sn-doped α-Ga_2O_3 MESFETs," IEEE Trans. Electron Devices **62**, 3640–3644 (2015).
188. M. Orita, H. Hiramatsu, H. Ohta, M. Hirano, and H. Hosono, "Preparation of highly conductive, deep ultraviolet transparent β-Ga_2O_3 thin film at low deposition temperatures," Thin Solid Films **411**, 134–139 (2002).
189. T. Oshima, K. Matsuyama, K. Yoshimatsu, and A. Ohtomo, "Conducting Si-doped γ-Ga_2O_3 epitaxial films grown by pulsed-laser deposition," J. Cryst. Growth **421**, 23–26 (2015).
190. L. Feng, Y. Li, X. Su, S. Wang, H. Liu, J. Wang, Z. Gong, W. Ding, Y. Zhang, and F. Yun, "Growth and characterization of spindle-like Ga_2O_3 nanocrystals by electrochemical reaction in hydrofluoric solution," Appl. Surf. Sci. **389**, 205–210 (2016).
191. B. Fernandes, M. Hegde, P. C. Stanish, Z. L. Mišković, and P. V. Radovanovic, "Photoluminescence decay dynamics in γ-Ga_2O_3 nanocrystals: the role of exclusion distance at short time scales," Chem. Phys. Lett. **684**, 135–140 (2017).
192. V. Ghodsi, S. Jin, J. C. Byers, Y. Pan, and P. V. Radovanovic, "Anomalous photocatalytic activity of nanocrystalline γ-phase Ga_2O_3 enabled by long-lived defect trap states," J. Phys. Chem. C **121**, 9433–9441 (2017).
193. J.-Y. Jung, W.-S. Cho, J.-H. Kim, K.-T. Hwang, E.-T. Kang, and K.-S. Han, "Morphological and crystal structural characterization of Ga_2O_3 particles synthesized by a controlled precipitation and polymerized complex method," Ceram. Int. **42**, 2582–2588 (2016).
194. A. H. A. Makinudin, T. M. Bawazeer, N. Alsenany, M. S. Alsoufi, and A. Supangat, "Gallium oxide nanospheres: effect of the post-annealing treatment," Mater. Lett. **194**, 53–57 (2017).

195. A. Singhal and I. Lieberwirth, “Non-aqueous synthesis of blue light emitting γ-Ga_2O_3 and c-In_2O_3 nanostructures from their ethylene glycolate precursors,” Mater. Lett. **161**, 112–116 (2015).
196. T. Wang, S. S. Farvid, and M. Abulikemu, and P. V. Radovanovic, “Size-tunable phosphorescence in colloidal metastable γ-Ga_2O_3 nanocrystals,” J. Am. Chem. Soc. **132**, 9250–9252 (2010).
197. S. P. Arnold, S. M. Prokes, F. K. Perkins, and M. E. Zaghloul, “Design and performance of a simple, room-temperature Ga_2O_3 nanowire gas sensor,” Appl. Phys. Lett. **95**, 103102 (2009).
198. E. Auer, A. Lugstein, S. Loffler, Y. J. Hyun, W. Brezna, E. Bertagnolli, and P. Pongratz, “Ultrafast VLS growth of epitaxial β-Ga_2O_3 nanowires,” Nanotechnology **20**, 434017 (2009).
199. K. F. Cai, S. Shen, C. Yan, and S. Bateman, “Preparation, characterization and formation mechanism of gallium oxide nanowires,” Curr. Appl. Phys. **8**, 363–366 (2008).
200. K.-W. Chang and J.-J. Wu, “Low-temperature catalytic growth of β-Ga_2O_3 nanowires using single organometallic precursor,” J. Phys. Chem. B **108**, 1838–1843 (2004).
201. L.-W. Chang, T.-Y. Lu, Y.-L. Chen, J.-W. Yeh, and H. C. Shih, “Effect of the doped nitrogen on the optical properties of β-Ga_2O_3 nanowires,” Mater. Lett. **65**, 2281–2283 (2011).
202. P.-C. Chang, Z. Fan, W.-Y. Tseng, A. Rajagopal, and J. G. Lu, “β-Ga_2O_3 nanowires: synthesis, characterization, and p-channel field-effect transistor,” Appl. Phys. Lett. **87**, 222102 (2005).
203. X. Chen, K. Liu, Z. Zhang, C. Wang, B. Li, H. Zhao, D. Zhao, and D. Shen, “Self-powered solar-blind photodetector with fast response based on Au/β-Ga_2O_3 nanowires array film Schottky junction,” ACS Appl. Mater. Interfaces **8**, 4185–4191 (2016).
204. K. H. Choi, K. K. Cho, G. B. Cho, H. J. Ahn, and K. W. Kim, “The growth behavior of β-Ga_2O_3 nanowires on the basis of catalyst size,” J. Cryst. Growth **311**, 1195–1200 (2009).
205. Y. C. Choi, W. S. Kim, Y. S. Park, S. M. Lee, D. J. Bae, Y. H. Lee, G. S. Park, W. B. Choi, N. S. Lee, and J. M. Kim, “Catalytic growth of β-Ga_2O_3 nanowires by arc discharge,” Adv. Mater. **12**, 746–750 (2000).
206. I. D. Hosein, M. Hegde, P. D. Jones, V. Chirmanov, and P. V. Radovanovic, “Evolution of the faceting, morphology and aspect ratio of gallium oxide nanowires grown by vapor–solid deposition,” J. Cryst. Growth **396**, 24–32 (2014).
207. C. H. Hsieh, L. J. Chou, G. R. Lin, Y. Bando, and D. Golberg, “Nanophotonic switch: gold-in-Ga_2O_3 peapod nanowires,” Nano Lett. **8**, 3081–3085 (2008).
208. J. Q. Hu, Q. Li, X. M. Meng, C. S. Lee, and S. T. Lee, “Synthesis of β-Ga_2O_3 nanowires by laser ablation,” J. Phys. Chem. B **106**, 9536–9539 (2002).
209. Y. Huang, S. Yue, Z. Wang, Q. Wang, C. Shi, Z. Xu, X. D. Bai, C. Tang, and C. Gu, “Preparation and electrical properties of ultrafine Ga_2O_3 nanowires,” J. Phys. Chem. B **110**, 796–800 (2006).
210. J. S. Hwang, T. Y. Liu, S. Chattopadhyay, G. M. Hsu, A. M. Basilio, H. W. Chen, Y. K. Hsu, W. H. Tu, Y. G. Lin, K. H. Chen, C. C. Li, S. B. Wang, H. Y. Chen, and L. C. Chen, “Growth of β-Ga_2O_3 and GaN nanowires on GaN for photoelectrochemical hydrogen generation,” Nanotechnology **24**, 055401 (2013).
211. J. Jie, C. Wu, Y. Yu, L. Wang, and Z. Hu, “Gallium-assisted growth of flute-like MgO nanotubes, Ga_2O_3-filled MgO nanotubes, and MgO/Ga_2O_3 co-axial nanotubes,” Nanotechnology **20**, 075602 (2009).
212. J. L. Johnson, Y. Choi, and A. Ural, “GaN nanowire and Ga_2O_3 nanowire and nanoribbon growth from ion implanted iron catalyst,” J. Vac. Sci. Technol. B **26**, 1841–1847 (2008).
213. M. C. Johnson, S. Aloni, D. E. McCready, and E. D. Bourret-Courchesne, “Controlled vapor–liquid–solid growth of indium, gallium, and tin oxide nanowires via chemical vapor transport,” Cryst. Growth Des. **6**, 1936–1941 (2006).
214. M. Kumar, S. Kumar, N. Chauhan, D. S. Kumar, V. Kumar, and R. Singh, “Study of GaN nanowires converted from β-Ga_2O_3 and photoconduction in a single nanowire,” Semicond. Sci. Technol. **32**, 085012 (2017).
215. M. Kumar, G. Sarau, M. Heilmann, S. Christiansen, V. Kumar, and R. Singh, “Effect of ammonification temperature on the formation of coaxial GaN/Ga_2O_3 nanowires,” J. Phys. D **50**, 035302 (2017).
216. S. Kumar, G. Sarau, C. Tessarek, M. Y. Bashouti, A. Hähnel, S. Christiansen, and R. Singh, “Study of iron-catalysed growth of β-Ga_2O_3 nanowires and their detailed characterization using TEM, Raman and cathodoluminescence techniques,” J. Phys. D **47**, 435101 (2014).
217. C. L. Kuo and M. H. Huang, “The growth of ultralong and highly blue luminescent gallium oxide nanowires and nanobelts, and direct horizontal nanowire growth on substrates,” Nanotechnology **19**, 155604 (2008).
218. Z. Li, B. Zhao, P. Liu, and Y. Zhang, “Synthesis of gallium oxide nanowires and their electrical properties,” Microelectron. Eng. **85**, 1613–1615 (2008).
219. C. H. Liang, G. W. Meng, G. Z. Wang, Y. W. Wang, L. D. Zhang, and S. Y. Zhang, “Catalytic synthesis and photoluminescence of β-Ga_2O_3 nanowires,” Appl. Phys. Lett. **78**, 3202–3204 (2001).
220. I. López, M. Alonso-Orts, E. Nogales, B. Méndez, and J. Piqueras, “Influence of Li doping on the morphology and luminescence of Ga_2O_3 microrods grown by a vapor-solid method,” Semicond. Sci. Technol. **31**, 115003 (2016).
221. I. López, E. Nogales, B. Méndez, and J. Piqueras, “Resonant cavity modes in gallium oxide microwires,” Appl. Phys. Lett. **100**, 261910 (2012).
222. I. López, E. Nogales, B. Méndez, J. Piqueras, A. Peche, J. Ramírez-Castellanos, and J. M. González-Calbet, “Influence of Sn and Cr doping on morphology and luminescence of thermally grown Ga_2O_3 nanowires,” J. Phys. Chem. C **117**, 3036–3045 (2013).
223. Y. Luo, Z. Hou, J. Gao, D. Jin, and X. Zheng, “Synthesis of high crystallization β-Ga_2O_3 micron rods with tunable morphologies and intensive blue emission via solution route,” Mater. Sci. Eng. B **140**, 123–127 (2007).
224. G. Martinez-Criado, J. Segura-Ruiz, M. H. Chu, R. Tucoulou, I. Lopez, E. Nogales, B. Mendez, and J. Piqueras, “Crossed Ga_2O_3/SnO_2 multiwire architecture: a local structure study with nanometer resolution,” Nano Lett. **14**, 5479–5487 (2014).
225. L. Mazeina, F. K. Perkins, V. M. Bermudez, S. P. Arnold, and S. M. Prokes, “Functionalized Ga_2O_3 nanowires as active material in room temperature capacitance-based gas sensors,” Langmuir **26**, 13722–13726 (2010).
226. L. Mazeina, Y. N. Picard, S. I. Maximenko, F. K. Perkins, E. R. Glaser, M. E. Twigg, J. A. Freitas, and S. M. Prokes, “Growth of Sn-doped β-Ga_2O_3 nanowires and Ga_2O_3–SnO_2 heterostructures for gas sensing applications,” Cryst. Growth Des. **9**, 4471–4479 (2009).
227. L. Mazeina, Y. N. Picard, and S. M. Prokes, “Controlled growth of parallel oriented ZnO nanostructural arrays on Ga_2O_3 nanowires,” Cryst. Growth Des. **9**, 1164–1169 (2009).
228. E. Nogales, J. A. García, B. Méndez, and J. Piqueras, “Red luminescence of Cr in β-Ga_2O_3 nanowires,” J. Appl. Phys. **101**, 033517 (2007).
229. E. Nogales, J. Á. García, B. Méndez, and J. Piqueras, “Doped gallium oxide nanowires with waveguiding behavior,” Appl. Phys. Lett. **91**, 133108 (2007).
230. E. Nogales, P. Hidalgo, K. Lorenz, B. Mendez, J. Piqueras, and E. Alves, “Cathodoluminescence of rare earth implanted Ga_2O_3 and GeO_2 nanostructures,” Nanotechnology **22**, 285706 (2011).
231. G. Sinha, A. Datta, S. K. Panda, P. G. Chavan, M. A. More, D. S. Joag, and A. Patra, “Self-catalytic growth and field-emission properties of Ga_2O_3 nanowires,” J. Phys. D **42**, 185409 (2009).
232. M. Suh, M. Meyyappan, and S. Ju, “The effect of Ga content on $In_{2x}Ga_{2-2x}O_3$ nanowire transistor characteristics,” Nanotechnology **23**, 305203 (2012).
233. T. Terasako, Y. Kawasaki, and M. Yagi, “Growth and morphology control of β-Ga_2O_3 nanostructures by atmospheric-pressure CVD,” Thin Solid Films **620**, 23–29 (2016).
234. Y. Yoon, K. I. Han, B. H. Kim, I. G. Lee, Y. Kim, J. P. Kim, and W. S. Hwang, “Formation of β-Ga_2O_3 nanofibers of sub-50 nm diameter synthesized by electrospinning method,” Thin Solid Films **645**, 358–362 (2018).
235. H. Z. Zhang, Y. C. Kong, Y. Z. Wang, X. Du, Z. G. Bai, J. J. Wang, D. P. Yu, Y. Ding, Q. L. Hang, and S. Q. Feng, “Ga_2O_3 nanowires

prepared by physical evaporation," Solid State Commun. **109**, 677–682 (1999).

236. S. Kumar, C. Tessarek, S. Christiansen, and R. Singh, "A comparative study of β-Ga_2O_3 nanowires grown on different substrates using CVD technique," J. Alloys Compd. **587**, 812–818 (2014).
237. W. Tian, C. Zhi, T. Zhai, S. Chen, X. Wang, M. Liao, D. Golberg, and Y. Bando, "In-doped Ga_2O_3 nanobelt based photodetector with high sensitivity and wide-range photoresponse," J. Mater. Chem. **22**, 17984–17991 (2012).
238. Y. L. Wu, S.-J. Chang, W. Y. Weng, C. H. Liu, T. Y. Tsai, C. L. Hsu, and K. C. Chen, "Ga_2O_3 nanowire photodetector prepared on SiO_2 template," IEEE Sens. J. **13**, 2368–2373 (2013).
239. S. Kumar, S. Dhara, R. Agarwal, and R. Singh, "Study of photoconduction properties of CVD grown β-Ga_2O_3 nanowires," J. Alloys Compd. **683**, 143–148 (2016).
240. B. Zhao, F. Wang, H. Chen, Y. Wang, M. Jiang, X. Fang, and D. Zhao, "Solar-blind avalanche photodetector based on single ZnO–Ga_2O_3 core–shell microwire," Nano Lett. **15**, 3988–3993 (2015).
241. D. Guo, H. Liu, P. Li, Z. Wu, S. Wang, C. Cui, C. Li, and W. Tang, "Zero-power-consumption solar-blind photodetector based on β-Ga_2O_3/NSTO heterojunction," ACS Appl. Mater. Interfaces **9**, 1619–1628 (2017).
242. X. Liu, G. Qiu, Y. Zhao, N. Zhang, and R. Yi, "Gallium oxide nanorods by the conversion of gallium oxide hydroxide nanorods," J. Alloys Compd. **439**, 275–278 (2007).
243. J. Zhang, Z. Liu, C. Lin, and J. Lin, "A simple method to synthesize β-Ga_2O_3 nanorods and their photoluminescence properties," J. Cryst. Growth **280**, 99–106 (2005).
244. S. C. Vanithakumari and K. K. Nanda, "A one-step method for the growth of Ga_2O_3-nanorod-based white-light-emitting phosphors," Adv. Mater. **21**, 3581–3584 (2009).
245. X.-S. Wang, W.-S. Li, J.-Q. Situ, X.-Y. Ying, H. Chen, Y. Jin, and Y.-Z. Du, "Multi-functional mesoporous β-Ga_2O_3:Cr^{3+} nanorod with long lasting near infrared luminescence for *in vivo* imaging and drug delivery," RSC Adv. **5**, 12886–12889 (2015).
246. G. Meligrana, W. Lueangchaichaweng, F. Colò, M. Destro, S. Fiorilli, P. P. Pescarmona, and C. Gerbaldi, "Gallium oxide nanorods as novel, safe and durable anode material for Li- and Na-ion batteries," Electrochim. Acta **235**, 143–149 (2017).
247. J. Zhang, S. Jiao, Y. Wan, S. Gao, D. Wang, and J. Wang, "A well-grown β-Ga_2O_3 microrods array transformed by GaOOH on Si (100) substrate and growth mechanism study," CrystEngComm **20**, 4329–4335 (2018).
248. K. K. Cho, G. B. Cho, K. W. Kim, and K. S. Ryu, "Growth behavior of β-Ga_2O_3 nanomaterials synthesized by catalyst-free thermal evaporation," Phys. Scr. **T139**, 014079 (2010).
249. A. K. Narayana Swamy, E. Shafirovich, and C. V. Ramana, "Synthesis of one-dimensional Ga_2O_3 nanostructures via high-energy ball milling and annealing of GaN," Ceram. Int. **39**, 7223–7227 (2013).
250. Y. Peng, N. Yu, Y. Xiang, J. Liu, L. Cao, and S. Huang, "One-step hydrothemal synthesis of nitrogen doped β-Ga_2O_3 nanostructure and its optical properties," J. Nanosci. Nanotechnol. **18**, 5654–5659 (2018).
251. S. Rafique, L. Han, C. A. Zorman, and H. Zhao, "Synthesis of wide bandgap β-Ga_2O_3 rods on 3C-SiC-on-Si," Cryst. Growth Des. **16**, 511–517 (2015).
252. Z. R. Dai, Z. W. Pan, and Z. L. Wang, "Gallium oxide nanoribbons and nanosheets," J. Phys. Chem. B **106**, 902–904 (2002).
253. Y. Guo, J. Zhang, F. Zhu, Z. X. Yang, J. Xu, and J. Yu, "Self-assembly of β-Ga_2O_3 nanobelts," Appl. Surf. Sci. **254**, 5124–5128 (2008).
254. L. Li, E. Auer, M. Liao, X. Fang, T. Zhai, U. K. Gautam, A. Lugstein, Y. Koide, Y. Bando, and D. Golberg, "Deep-ultraviolet solar-blind photoconductivity of individual gallium oxide nanobelts," Nanoscale **3**, 1120–1126 (2011).
255. L.-C. Tien, W.-T. Chen, and C.-H. Ho, "Enhanced photocatalytic activity in β-Ga_2O_3 nanobelts," J. Am. Ceram. Soc. **94**, 3117–3122 (2011).
256. R. Zou, Z. Zhang, Q. Liu, J. Hu, L. Sang, M. Liao, and W. Zhang, "High detectivity solar-blind high-temperature deep-ultraviolet photodetector based on multi-layered (/00) facet-oriented β-Ga_2O_3 nanobelts," Small **10**, 1848–1856 (2014).
257. F. Zhu, Z. X. Yang, W. M. Zhou, and Y. F. Zhang, "Direct synthesis of beta gallium oxide nanowires, nanobelts, nanosheets and nanograsses by microwave plasma," Solid State Commun. **137**, 177–181 (2006).
258. W. Feng, X. Wang, J. Zhang, L. Wang, W. Zheng, P. Hu, W. Cao, and B. Yang, "Synthesis of two-dimensional β-Ga_2O_3 nanosheets for high-performance solar blind photodetectors," J. Mater. Chem. C **2**, 3254–3259 (2014).
259. M. Zhong, Z. Wei, X. Meng, F. Wu, and J. Li, "High-performance single crystalline UV photodetectors of β-Ga_2O_3," J. Alloys Compd. **619**, 572–575 (2015).
260. E. Nogales, B. Mendez, and J. Piqueras, "Assessment of waveguiding properties of gallium oxide nanostructures by angle resolved cathodoluminescence in a scanning electron microscope," Ultramicroscopy **111**, 1037–1042 (2011).
261. E. Nogales, B. Mendez, J. Piqueras, and J. A. Garcia, "Europium doped gallium oxide nanostructures for room temperature luminescent photonic devices," Nanotechnology **20**, 115201 (2009).
262. T. Shao, P. Zhang, L. Jin, and Z. Li, "Photocatalytic decomposition of perfluorooctanoic acid in pure water and sewage water by nanostructured gallium oxide," Appl. Catal. B **142-143**, 654–661 (2013).
263. Y. Teng, X. Song le, A. Ponchel, Z. K. Yang, and J. Xia, "Self-assembled metastable γ-Ga_2O_3 nanoflowers with hexagonal nanopetals for solar-blind photodetection," Adv. Mater. **26**, 6238–6243 (2014).
264. G. Shin, H.-Y. Kim, and J. Kim, "Deep-ultraviolet photodetector based on exfoliated n-type β-Ga_2O_3 nanobelt/p-Si substrate heterojunction," Korean J. Chem. Eng. **35**, 574–578 (2017).
265. G. Yang, S. Jang, F. Ren, S. J. Pearton, and J. Kim, "Influence of high-energy proton irradiation on β-Ga_2O_3 nanobelt field-effect transistors," ACS Appl. Mater. Interfaces **9**, 40471–40476 (2017).
266. P. Feng, J. Y. Zhang, Q. H. Li, and T. H. Wang, "Individual β-Ga_2O_3 nanowires as solar-blind photodetectors," Appl. Phys. Lett. **88**, 153107 (2006).
267. N. D. Cuong, Y. W. Park, and S. G. Yoon, "Microstructural and electrical properties of Ga_2O_3 nanowires grown at various temperatures by vapor–liquid–solid technique," Sens. Actuators B **140**, 240–244 (2009).
268. S. Phumying, S. Labauyai, W. Chareonboon, S. Phokha, and S. Maensiri, "Optical properties of β-Ga_2O_3 nanorods synthesized by a simple and cost-effective method using egg white solution," Jpn. J. Appl. Phys. **54**, 06fj13 (2015).
269. W.-S. Jung, H. U. Joo, and B.-K. Min, "Growth of β-gallium oxide nanostructures by the thermal annealing of compacted gallium nitride powder," Phys. E (Amsterdam) **36**, 226–230 (2007).
270. R. S. Wagner and W. C. Ellis, "Vapor-liquid-solid mechanism of single crystal growth," Appl. Phys. Lett. **4**, 89–90 (1964).
271. B. Zhao, F. Wang, H. Chen, L. Zheng, L. Su, D. Zhao, and X. Fang, "An ultrahigh responsivity (9.7 $mA \cdot W^{-1}$) self-powered solar-blind photodetector based on individual ZnO–Ga_2O_3 heterostructures," Adv. Funct. Mater. **27**, 1700264 (2017).
272. Z. Guo, A. Verma, X. Wu, F. Sun, A. Hickman, T. Masui, A. Kuramata, M. Higashiwaki, D. Jena, and T. Luo, "Anisotropic thermal conductivity in single crystal β-gallium oxide," Appl. Phys. Lett. **106**, 111909 (2015).
273. C. Kranert, C. Sturm, R. Schmidt-Grund, and M. Grundmann, "Raman tensor elements of β-Ga_2O_3," Sci. Rep. **6**, 35964 (2016).
274. H. He, M. A. Blanco, and R. Pandey, "Electronic and thermodynamic properties of β-Ga_2O_3," Appl. Phys. Lett. **88**, 261904 (2006).
275. A. Mock, R. Korlacki, C. Briley, V. Darakchieva, B. Monemar, Y. Kumagai, K. Goto, M. Higashiwaki, and M. Schubert, "Band-to-band transitions, selection rules, effective mass, and excitonic contributions in monoclinic β-Ga_2O_3," Phys. Rev. B **96**, 245205 (2017).
276. V. M. Bermudez, "The structure of low-index surfaces of β-Ga_2O_3," Chem. Phys. **323**, 193–203 (2006).
277. T. Liu, I. Tranca, J. Yang, X. Zhou, and C. Li, "Theoretical insight into the roles of cocatalysts in the Ni–NiO/β-Ga_2O_3 photocatalyst for overall water splitting," J. Mater. Chem. A **3**, 10309–10319 (2015).

278. K. Yamaguchi, "First principles study on electronic structure of β-Ga$_2$O$_3$," Solid State Commun. **131**, 739–744 (2004).
279. J. B. Varley, J. R. Weber, A. Janotti, and C. G. Van de Walle, "Oxygen vacancies and donor impurities in β-Ga$_2$O$_3$," Appl. Phys. Lett. **97**, 142106 (2010).
280. C. Janowitz, V. Scherer, M. Mohamed, A. Krapf, H. Dwelk, R. Manzke, Z. Galazka, R. Uecker, K. Irmscher, R. Fornari, M. Michling, D. Schmeißer, J. R. Weber, J. B. Varley, and C. G. Van de Walle, "Experimental electronic structure of In$_2$O$_3$ and Ga$_2$O$_3$," New J. Phys. **13**, 085014 (2011).
281. T. C. Lovejoy, E. N. Yitamben, N. Shamir, J. Morales, E. G. Villora, K. Shimamura, S. Zheng, F. S. Ohuchi, and M. A. Olmstead, "Surface morphology and electronic structure of bulk single crystal β-Ga$_2$O$_3$ (100)," Appl. Phys. Lett. **94**, 081906 (2009).
282. M. Mohamed, C. Janowitz, I. Unger, R. Manzke, Z. Galazka, R. Uecker, R. Fornari, J. R. Weber, J. B. Varley, and C. G. Van de Walle, "The electronic structure of β-Ga$_2$O$_3$," Appl. Phys. Lett. **97**, 211903 (2010).
283. J. Li, X. Chen, T. Ma, X. Cui, F.-F. Ren, S. Gu, R. Zhang, Y. Zheng, S. P. Ringer, L. Fu, H. H. Tan, C. Jagadish, and J. Ye, "Identification and modulation of electronic band structures of single-phase β-(Al$_x$Ga$_{1-x}$)$_2$O$_3$ alloys grown by laser molecular beam epitaxy," Appl. Phys. Lett. **113**, 041901 (2018).
284. T. Onuma, Y. Nakata, K. Sasaki, T. Masui, T. Yamaguchi, T. Honda, A. Kuramata, S. Yamakoshi, and M. Higashiwaki, "Modeling and interpretation of UV and blue luminescence intensity in β-Ga$_2$O$_3$ by silicon and nitrogen doping," J. Appl. Phys. **124**, 075103 (2018).
285. T. Harwig, F. Kellendonk, and S. Slappendel, "The ultraviolet luminescence of β-galliumsesquioxide," J. Phys. Chem. Solids **39**, 675–680 (1978).
286. T. Harwig and F. Kellendonk, "Some observations on the photoluminescence of doped β-galliumsesquioxide," J. Solid State Chem. **24**, 255–263 (1978).
287. L. Binet and D. Gourier, "Origin of the blue luminescence of β-Ga$_2$O$_3$," J. Phys. Chem. Solids **59**, 1241–1249 (1998).
288. C. Rivera, J. L. Pau, E. Muñoz, P. Misra, O. Brandt, H. T. Grahn, and K. H. Ploog, "Polarization-sensitive ultraviolet photodetectors based on M-plane GaN grown on LiAlO$_2$ substrates," Appl. Phys. Lett. **88**, 213507 (2006).
289. S. Ghosh, C. Rivera, J. L. Pau, E. Muñoz, O. Brandt, and H. T. Grahn, "Very narrow-band ultraviolet photodetection based on strained M-plane GaN films," Appl. Phys. Lett. **90**, 091110 (2007).
290. S. Ghosh, C. Rivera, J. L. Pau, E. Muñoz, O. Brandt, and H. T. Grahn, "Narrow-band photodetection based on M-plane GaN films," Phys. Status Solidi A **205**, 1100–1102 (2008).
291. K. H. Zhang, K. Xi, M. G. Blamire, and R. G. Egdell, "P-type transparent conducting oxides," J. Phys. Condens. Matter **28**, 383002 (2016).
292. J. Furthmüller and F. Bechstedt, "Quasiparticle bands and spectra of Ga$_2$O$_3$ polymorphs," Phys. Rev. B **93**, 115204 (2016).
293. J. L. Lyons, "A survey of acceptor dopants for β-Ga$_2$O$_3$," Semicond. Sci. Technol. **33**, 05LT02 (2018).
294. K. Tetzner, A. Thies, E. B. Treidel, F. Brunner, and G. Wagner, "Selective area isolation of β-Ga$_2$O$_3$ using multiple energy nitrogen ion implantation," Appl. Phys. Lett. **113**, 172104 (2018).
295. M. H. Wong, C.-H. Lin, A. Kuramata, S. Yamakoshi, H. Murakami, Y. Kumagai, and M. Higashiwaki, "Acceptor doping of β-Ga$_2$O$_3$ by Mg and N ion implantations," Appl. Phys. Lett. **113**, 102103 (2018).
296. M. J. Tadjer, A. D. Koehler, J. A. Freitas, J. C. Gallagher, M. C. Specht, E. R. Glaser, K. D. Hobart, T. J. Anderson, F. J. Kub, Q. T. Thieu, K. Sasaki, D. Wakimoto, K. Goto, S. Watanabe, and A. Kuramata, "High resistivity halide vapor phase homoepitaxial β-Ga$_2$O$_3$ films co-doped by silicon and nitrogen," Appl. Phys. Lett. **113**, 192102 (2018).
297. B. E. Kananen, L. E. Halliburton, E. M. Scherrer, K. T. Stevens, G. K. Foundos, K. B. Chang, and N. C. Giles, "Electron paramagnetic resonance study of neutral Mg acceptors in β-Ga$_2$O$_3$ crystals," Appl. Phys. Lett. **111**, 072102 (2017).
298. A. Navarro-Quezada, S. Alamé, N. Esser, J. Furthmüller, F. Bechstedt, Z. Galazka, D. Skuridina, and P. Vogt, "Near valence-band electronic properties of semiconducting β–Ga$_2$O$_3$ single crystals," Phys. Rev. B **92**, 195306 (2015).
299. H. Morko, *Handbook of Nitride Semiconductors and Devices* (Springer, 2008).
300. B. C. Shih, Y. Xue, P. Zhang, M. L. Cohen, and S. G. Louie, "Quasiparticle band gap of ZnO: high accuracy from the conventional G^{0}W^0 approach," Phys. Rev. Lett. **105**, 146401 (2010).
301. H. Reiss, C. S. Fuller, and A. J. Pietruszkiewicz, "Solubility of lithium in doped and undoped silicon, evidence for compound formation," J. Chem. Phys. **25**, 650–655 (1956).
302. H. Reiss, C. S. Fuller, and F. J. Morin, "Chemical interactions among defects in germanium and silicon," Bell Syst. Tech. J. **35**, 535–636 (1956).
303. R. Y. Korotkov, J. M. Gregie, and B. W. Wessels, "Codoping of wide gap epitaxial III-nitride semiconductors," Opto-Electron. Rev. **10**, 243–249 (2002).
304. T. Oshima, T. Okuno, N. Arai, N. Suzuki, S. Ohira, and S. Fujita, "Vertical solar-blind deep-ultraviolet Schottky photodetectors based on β-Ga$_2$O$_3$ substrates," Appl. Phys. Express **1**, 011202 (2008).
305. T. Oshima, T. Okuno, N. Arai, N. Suzuki, H. Hino, and S. Fujita, "Flame detection by a β-Ga$_2$O$_3$-based sensor," Jpn. J. Appl. Phys. **48**, 011605 (2009).
306. C. Yang, H. Liang, Z. Zhang, X. Xia, P. Tao, Y. Chen, H. Zhang, R. Shen, Y. Luo, and G. Du, "Self-powered SBD solar-blind photodetector fabricated on the single crystal of β-Ga$_2$O$_3$," RSC Adv. **8**, 6341–6345 (2018).
307. Y. Kokubun, K. Miura, F. Endo, and S. Nakagomi, "Sol-gel prepared β-Ga$_2$O$_3$ thin films for ultraviolet photodetectors," Appl. Phys. Lett. **90**, 031912 (2007).
308. T. Oshima, T. Okuno, and S. Fujita, "Ga$_2$O$_3$ thin film growth on c-plane sapphire substrates by molecular beam epitaxy for deep-ultraviolet photodetectors," Jpn. J. Appl. Phys. **46**, 7217–7220 (2007).
309. D. Guo, Z. Wu, P. Li, Y. An, H. Liu, X. Guo, H. Yan, G. Wang, C. Sun, L. Li, and W. Tang, "Fabrication of β-Ga$_2$O$_3$ thin films and solar-blind photodetectors by laser MBE technology," Opt. Mater. Express **4**, 1067–1076 (2014).
310. D. Y. Guo, Z. P. Wu, Y. H. An, X. C. Guo, X. L. Chu, C. L. Sun, L. H. Li, P. G. Li, and W. H. Tang, "Oxygen vacancy tuned ohmic-Schottky conversion for enhanced performance in β-Ga$_2$O$_3$ solar-blind ultraviolet photodetectors," Appl. Phys. Lett. **105**, 023507 (2014).
311. G. C. Hu, C. X. Shan, N. Zhang, M. M. Jiang, S. P. Wang, and D. Z. Shen, "High gain Ga$_2$O$_3$ solar-blind photodetectors realized via a carrier multiplication process," Opt. Express **23**, 13554–13561 (2015).
312. Q. Feng, L. Huang, G. Han, F. Li, X. Li, L. Fang, X. Xing, J. Zhang, W. Mu, Z. Jia, D. Guo, W. Tang, X. Tao, and Y. Hao, "Comparison study of β-Ga$_2$O$_3$ photodetectors on bulk substrate and sapphire," IEEE Trans. Electron Devices **63**, 3578–3583 (2016).
313. D. Y. Guo, X. L. Zhao, Y. S. Zhi, W. Cui, Y. Q. Huang, Y. H. An, P. G. Li, Z. P. Wu, and W. H. Tang, "Epitaxial growth and solar-blind photoelectric properties of corundum-structured α-Ga$_2$O$_3$ thin films," Mater. Lett. **164**, 364–367 (2016).
314. Y. H. An, Y. S. Zhi, W. Cui, X. L. Zhao, Z. P. Wu, D. Y. Guo, P. G. Li, and W. H. Tang, "Thickness tuning photoelectric properties of β-Ga$_2$O$_3$ thin film based photodetectors," J. Nanosci. Nanotechnol. **17**, 9091–9094 (2017).
315. S. Cui, Z. Mei, Y. Zhang, H. Liang, and X. Du, "Room-temperature fabricated amorphous Ga$_2$O$_3$ high-response-speed solar-blind photodetector on rigid and flexible substrates," Adv. Opt. Mater. **5**, 1700454 (2017).
316. S. H. Lee, S. B. Kim, Y.-J. Moon, S. M. Kim, H. J. Jung, M. S. Seo, K. M. Lee, S.-K. Kim, and S. W. Lee, "High-responsivity deep-ultraviolet-selective photodetectors using ultrathin gallium oxide films," ACS Photon. **4**, 2937–2943 (2017).
317. L.-X. Qian, Z.-H. Wu, Y.-Y. Zhang, P. T. Lai, X.-Z. Liu, and Y.-R. Li, "Ultrahigh-responsivity, rapid-recovery, solar-blind photodetector based on highly nonstoichiometric amorphous gallium oxide," ACS Photon. **4**, 2203–2211 (2017).
318. A. S. Pratiyush, S. Krishnamoorthy, S. Vishnu Solanke, Z. Xia, R. Muralidharan, S. Rajan, and D. N. Nath, "High responsivity in molecular beam epitaxy grown β-Ga$_2$O$_3$ metal semiconductor metal

solar blind deep-UV photodetector," Appl. Phys. Lett. **110**, 221107 (2017).

319. F. H. Teherani, D. C. Look, D. J. Rogers, F. Alema, B. Hertog, A. V. Osinsky, P. Mukhopadhyay, M. Toporkov, W. V. Schoenfeld, and E. Ahmadi, and J. Speck, "Vertical solar blind Schottky photodiode based on homoepitaxial Ga_2O_3 thin film," Proc. SPIE **10105**, 101051M (2017).
320. H.-Y. Lee, J.-T. Liu, and C.-T. Lee, "Modulated Al_2O_3-alloyed Ga_2O_3 materials and deep ultraviolet photodetectors," IEEE Photon. Technol. Lett. **30**, 549–552 (2018).
321. S.-H. Yuan, C.-C. Wang, S.-Y. Huang, and D.-S. Wuu, "Improved responsivity drop from 250 to 200 nm in sputtered gallium oxide photodetectors by incorporating trace aluminum," IEEE Electron Device Lett. **39**, 220–223 (2018).
322. Q. Feng, X. Li, G. Han, L. Huang, F. Li, W. Tang, J. Zhang, and Y. Hao, "$(AlGa)_2O_3$ solar-blind photodetectors on sapphire with wider bandgap and improved responsivity," Opt. Mater. Express **7**, 1240–1248 (2017).
323. W. Y. Weng, T. J. Hsueh, S. J. Chang, S. C. Hung, G. J. Huang, H. T. Hsueh, Z. D. Huang, and C. J. Chiu, "An $(Al_xGa_{1-x})_2O_3$ metal-semiconductor-metal VUV photodetector," IEEE Sens. J. **11**, 1795–1799 (2011).
324. Y. Kokubun, T. Abe, and S. Nakagomi, "Sol-gel prepared $(Ga_{1-x}In_x)_2O_3$ thin films for solar-blind ultraviolet photodetectors," Phys. Status Solidi A **207**, 1741–1745 (2010).
325. T.-H. Chang, S.-J. Chang, C. J. Chiu, C.-Y. Wei, Y.-M. Juan, and W.-Y. Weng, "Bandgap-engineered in indium–gallium–oxide ultraviolet phototransistors," IEEE Photon. Technol. Lett. **27**, 915–918 (2015).
326. Z. Zhang, H. von Wenckstern, J. Lenzner, M. Lorenz, and M. Grundmann, "Visible-blind and solar-blind ultraviolet photodiodes based on $(In_xGa_{1-x})_2O_3$," Appl. Phys. Lett. **108**, 123503 (2016).
327. J. C. Carrano, T. Li, P. A. Grudowski, C. J. Eiting, R. D. Dupuis, and J. C. Campbell, "Current transport mechanisms in GaN-based metal–semiconductor–metal photodetectors," Appl. Phys. Lett. **72**, 542–544 (1998).
328. E. Monroy, F. Calle, E. Munoz, and F. Omnes, "Effects of bias on the responsivity of GaN metal–semiconductor–metal photodiodes," Phys. Status Solidi A **176**, 157–161 (1999).
329. W. Y. Weng, T. J. Hsueh, S. J. Chang, G. J. Huang, and S. P. Chang, "A solar-blind β-Ga_2O_3 nanowire photodetector," IEEE Photon. Technol. Lett. **22**, 709–711 (2010).
330. W. Y. Weng, T. J. Hsueh, S. J. Chang, G. J. Huang, and S. C. Hung, "Growth of Ga_2O_3 nanowires and the fabrication of solar-blind photodetector," IEEE Trans. Nanotechnol. **10**, 1047–1052 (2011).
331. Y. Li, T. Tokizono, M. Liao, M. Zhong, Y. Koide, I. Yamada, and J.-J. Delaunay, "Efficient assembly of bridged β-Ga_2O_3 nanowires for solar-blind photodetection," Adv. Funct. Mater. **20**, 3972–3978 (2010).
332. I. López, A. Castaldini, A. Cavallini, E. Nogales, B. Méndez, and J. Piqueras, "β-Ga_2O_3 nanowires for an ultraviolet light selective frequency photodetector," J. Phys. D **47**, 415101 (2014).
333. J. Du, J. Xing, C. Ge, H. Liu, P. Liu, H. Hao, J. Dong, Z. Zheng, and H. Gao, "Highly sensitive and ultrafast deep UV photodetector based on a β-Ga_2O_3 nanowire network grown by CVD," J. Phys. D **49**, 425105 (2016).
334. O. Lupan, T. Braniste, M. Deng, L. Ghimpu, I. Paulowicz, Y. K. Mishra, L. Kienle, R. Adelung, and I. Tiginyanu, "Rapid switching and ultra-responsive nanosensors based on individual shell–core Ga_2O_3/GaN:O_x@SnO_2 nanobelt with nanocrystalline shell in mixed phases," Sens. Actuators B **221**, 544–555 (2015).
335. X. Wang, W. Tian, M. Liao, Y. Bando, and D. Golberg, "Recent advances in solution-processed inorganic nanofilm photodetectors," Chem. Soc. Rev. **43**, 1400–1422 (2014).
336. W. Y. Weng, T. J. Hsueh, S. J. Chang, G. J. Huang, and H. T. Hsueh, "A β-Ga_2O_3/GaN hetero-structured solar-blind and visible-blind dual-band photodetector," IEEE Sens. J. **11**, 1491–1492 (2011).
337. W. Y. Weng, T. J. Hsueh, S. J. Chang, G. J. Huang, and H. T. Hsueh, "A β-Ga_2O_3/GaN Schottky-barrier photodetector," IEEE Photon. Technol. Lett. **23**, 444–446 (2011).
338. Z.-D. Huang, W. Y. Weng, S. J. Chang, C.-J. Chiu, T.-J. Hsueh, and S.-L. Wu, "Ga_2O_3/AlGaN/GaN heterostructure ultraviolet three-band photodetector," IEEE Sens. J. **13**, 3462–3467 (2013).
339. Z.-D. Huang, W.-Y. Weng, S.-J. Chang, Y.-F. Hua, C.-J. Chiu, and T.-Y. Tsai, "Ga_2O_3/GaN-based metal-semiconductor-metal photodetectors covered with Au nanoparticles," IEEE Photonics Technol. Lett. **25**, 1809–1811 (2013).
340. S. Nakagomi, T.-A. Sato, Y. Takahashi, and Y. Kokubun, "Deep ultraviolet photodiodes based on the β-Ga_2O_3/GaN heterojunction," Sens. Actuators A **232**, 208–213 (2015).
341. P. Li, H. Shi, K. Chen, D. Guo, W. Cui, Y. Zhi, S. Wang, Z. Wu, Z. Chen, and W. Tang, "Construction of GaN/Ga_2O_3 p–n junction for an extremely high responsivity self-powered UV photodetector," J. Mater. Chem. C **5**, 10562–10570 (2017).
342. S. Nakagomi, T. Momo, S. Takahashi, and Y. Kokubun, "Deep ultraviolet photodiodes based on β-Ga_2O_3/SiC heterojunction," Appl. Phys. Lett. **103**, 072105 (2013).
343. Y. Qu, Z. Wu, M. Ai, D. Guo, Y. An, H. Yang, L. Li, and W. Tang, "Enhanced Ga_2O_3/SiC ultraviolet photodetector with graphene top electrodes," J. Alloys Compd. **680**, 247–251 (2016).
344. S. Nakagomi, T. Sakai, K. Kikuchi, and Y. Kokubun, "β-Ga_2O_3/p-type 4H-SiC heterojunction diodes and applications to deep-UV photodiodes," Phys. Status Solidi A **215**, 1700796 (2018).
345. Y. H. An, D. Y. Guo, S. Y. Li, Z. P. Wu, Y. Q. Huang, P. G. Li, L. H. Li, and W. H. Tang, "Influence of oxygen vacancies on the photoresponse of β-Ga_2O_3/SiC n–n type heterojunctions," J. Phys. D **49**, 285111 (2016).
346. D. Y. Guo, H. Z. Shi, Y. P. Qian, M. Lv, P. G. Li, Y. L. Su, Q. Liu, K. Chen, S. L. Wang, C. Cui, C. R. Li, and W. H. Tang, "Fabrication of β-Ga_2O_3/ZnO heterojunction for solar-blind deep ultraviolet photodetection," Semicond. Sci. Technol. **32**, 03lt01 (2017).
347. Z. Wu, L. Jiao, X. Wang, D. Guo, W. Li, L. Li, F. Huang, and W. Tang, "A self-powered deep-ultraviolet photodetector based on an epitaxial Ga_2O_3/Ga:ZnO heterojunction," J. Mater. Chem. C **5**, 8688–8693 (2017).
348. Y. An, Y. Zhi, Z. Wu, W. Cui, X. Zhao, D. Guo, P. Li, and W. Tang, "Deep ultraviolet photodetectors based on p-Si/i-SiC/n-Ga_2O_3 heterojunction by inserting thin SiC barrier layer," Appl. Phys. A **122**, 1036 (2016).
349. X. C. Guo, N. H. Hao, D. Y. Guo, Z. P. Wu, Y. H. An, X. L. Chu, L. H. Li, P. G. Li, M. Lei, and W. H. Tang, "β-Ga_2O_3/p-Si heterojunction solar-blind ultraviolet photodetector with enhanced photoelectric responsivity," J. Alloys Compd. **660**, 136–140 (2016).
350. W. Y. Kong, G. A. Wu, K. Y. Wang, T. F. Zhang, Y. F. Zou, D. D. Wang, and L. B. Luo, "Graphene-β-Ga_2O_3 heterojunction for highly sensitive deep UV photodetector application," Adv. Mater. **28**, 10725–10731 (2016).
351. R. Lin, W. Zheng, D. Zhang, Z. Zhang, Q. Liao, L. Yang, and F. Huang, "High-performance graphene/β-Ga_2O_3 heterojunction deep-ultraviolet photodetector with hot-electron excited carrier multiplication," ACS Appl. Mater. Interfaces **10**, 22419–22426 (2018).
352. W. E. Mahmoud, "Solar blind avalanche photodetector based on the cation exchange growth of β-Ga_2O_3/SnO_2 bilayer heterostructure thin film," Sol. Energy Mater. Sol. Cells **152**, 65–72 (2016).
353. Z. Chen, K. Nishihagi, X. Wang, K. Saito, T. Tanaka, M. Nishio, M. Arita, and Q. Guo, "Band alignment of Ga_2O_3/Si heterojunction interface measured by x-ray photoelectron spectroscopy," Appl. Phys. Lett. **109**, 102106 (2016).
354. W. Wei, Z. Qin, S. Fan, Z. Li, K. Shi, Q. Zhu, and G. Zhang, "Valence band offset of β-Ga_2O_3/wurtzite GaN heterostructure measured by x-ray photoelectron spectroscopy," Nano. Res. Lett. **7**, 562 (2012).
355. M. Grodzicki, P. Mazur, S. Zuber, J. Brona, and A. Ciszewski, "Oxidation of GaN(0001) by low-energy ion bombardment," Appl. Surf. Sci. **304**, 20–23 (2014).
356. S.-H. Chang, Z.-Z. Chen, W. Huang, X.-C. Liu, B.-Y. Chen, Z.-Z. Li, and E.-W. Shi, "Band alignment of Ga_2O_3/6H-SiC heterojunction," Chin. Phys. B **20**, 116101 (2011).
357. H. Sun, C. G. T. Castanedo, K. Liu, K.-H. Li, W. Guo, R. Lin, X. Liu, J. Li, and X. Li, "Valence and conduction band offsets of β-Ga_2O_3/AlN heterojunction," Appl. Phys. Lett. **111**, 162105 (2017).

358. T. Wang, W. Li, C. Ni, and A. Janotti, “Band gap and band offset of Ga_2O_3 and $(Al_xGa_{1-x})_2O_3$ alloys,” Phys. Rev. Appl. **10**, 011003 (2018).
359. S. J. Pearton, J. Yang, P. H. Cary, F. Ren, J. Kim, M. J. Tadjer, and M. A. Mastro, “A review of Ga_2O_3 materials, processing, and devices,” Appl. Phys. Rev. **5**, 011301 (2018).
360. T. Tut, M. Gokkavas, B. Butun, S. Butun, E. Ulker, and E. Ozbay, “Experimental evaluation of impact ionization coefficients in $Al_xGa_{1-x}N$ based avalanche photodiodes,” Appl. Phys. Lett. **89**, 183524 (2006).
361. Y. Huang, D. J. Chen, H. Lu, K. X. Dong, R. Zhang, Y. D. Zheng, L. Li, and Z. H. Li, “Back-illuminated separate absorption and multiplication AlGaN solar-blind avalanche photodiodes,” Appl. Phys. Lett. **101**, 253516 (2012).
362. M. H. Wong, A. Takeyama, T. Makino, T. Ohshima, K. Sasaki, A. Kuramata, S. Yamakoshi, and M. Higashiwaki, “Radiation hardness of β-Ga_2O_3 metal-oxide-semiconductor field-effect transistors against gamma-ray irradiation,” Appl. Phys. Lett. **112**, 023503 (2018).
363. J. Kim, S. Pearton, C. Fares, J. Yang, F. Ren, S. Kim, and A. Y. Polyakov, “Radiation damage effects in Ga_2O_3 materials and devices,” J. Mater. Chem. C **7**, 10–24 (2019).
364. E. Wendler, E. Treiber, J. Baldauf, S. Wolf, and C. Ronning, “High-level damage saturation below amorphisation in ion implanted β-Ga_2O_3,” Nucl. Instrum. Methods Phys. Res. B **379**, 85–90 (2016).
365. “Ground breaking work on gallium oxide (Ga_2O_3) normally-off transistor,” FLOSFIA Inc., 2018, http://rocakk.sakura.ne.jp/index/struct/wp-content/uploads/79cd9d2dfa54a771f642e008cc4f9cb0.pdf.